Engineering Journal

Second Quarter 2023 | Volume 60, No. 2

AMERICAN INSTITUTE OF STEEL CONSTRUCTION
AISC
FOUNDED 1921

**Smarter.
Stronger.
Steel.**

Discussion:

Steel Structures Research Update

Engineering Journal

American Institute of Steel Construction

Dedicated to the development and improvement of steel construction, through the interchange of ideas, experiences, and data.

Editorial Staff

Editor	Margaret A. Matthew, PE
Managing Editor	Keith A. Grubb, SE, PE
Research Editor	Judy Liu, PhD
Production Editor	Kristin Hall

Officers

Chair
Stephen H. Knitter

Vice Chair
Hugh J. McCaffrey

Secretary/Legal Counsel
Edward Seglias

President
Charles J. Carter, SE, PE, PhD

Senior Vice Presidents
Scott L. Melnick
Mark W. Trimble, PE

Vice Presidents
Todd Alwood
Carly Hurd, CAE
Christopher H. Raebel, SE, PE, PhD
Michael Mospan
Brian Raff

The articles contained herein are not intended to represent official attitudes, recommendations or policies of the Institute. The Institute is not responsible for any statements made or opinions expressed by contributors to this Journal.

The opinions of the authors herein do not represent an official position of the Institute, and in every case the officially adopted publications of the Institute will control and supersede any suggestions or modifications contained in any articles herein.

The information presented herein is based on recognized engineering principles and is for general information only. While it is believed to be accurate, this information should not be applied to any specific application without competent professional examination and verification by a licensed professional engineer. Anyone making use of this information assumes all liability arising from such use.

Manuscripts are welcomed, but publication cannot be guaranteed. All manuscripts should be submitted in duplicate. Authors do not receive a remuneration. Guidelines for authors are printed on the inside back cover.

Engineering Journal (ISSN 0013-8029) is published quarterly. Published by the American Institute of Steel Construction at 130 E Randolph Street, Suite 2000, Chicago, IL 60601.

Copyright 2023 by the American Institute of Steel Construction. All rights reserved. No part of this publication may be reproduced without written permission. The AISC logo is a registered trademark of AISC.

Archives: Search at **aisc.org/ej**.
Article downloads are free for current members and are available for a nominal fee for non-members.

Discussion of:
Design for Local Member Shear at Brace and Diagonal-Member Connections: Full-Height and Chevron Gusset

Original Paper by Rafael Sabelli and Brandt Saxey

Discussion by Paul W. Richards

ABSTRACT

The paper "Design for Local Member Shear at Brace and Diagonal-Member Connections: Full-Height and Chevron Gusset" (Sabelli and Saxey, 2021) develops equations for checking local member shear demands using a Concentrated Stress Method (CSM) and presents a design example. This discussion presents results from a finite element (FE) model, based on the design example in the paper, to quantify the accuracy of the proposed design equations in predicting beam yielding. The FE model confirmed that the beam yielding state would not have occurred for the example frame under the design forces but would have occurred for forces about 4% higher. The stress and strain distributions observed in the FE model were consistent with those assumed in the CSM, although two points for potential refinement were noted. If beam yielding in a concentrically braced frame is forced, through oversized braces, the plastic mechanism would be like an eccentrically braced frame (EBF) but with higher yield force and higher beam inelastic rotations and strains for the same inelastic story drift.

INTRODUCTION

The paper being discussed is one of several articles that have appeared in the AISC *Engineering Journal* addressing local member shear demands in braced frames (Fortney and Thornton, 2015, 2017; Fortney, 2020; Hadad and Thornton, 2022; Roeder et al., 2021; Sabelli and Bolin, 2022; Sabelli and Saxey, 2021; Sabelli et al., 2021). In the paper, the authors develop equations for checking local member shear demands in braced frames using a Concentrated Stress Method (CSM) and present a design example.

Figure 1 shows braced frames with different governing limit states. For seismic design, it is the intent of the *Seismic Provisions for Structural Steel Buildings* (AISC, 2016) that a brace yielding limit state govern [Figure 1(a)]. For nonseismic design, it could be fine for a beam shear yielding limit state to govern [Figure 1(b)], but the limit state needs to be checked explicitly to ensure that it is not reached under the design loads. Sabelli and Saxey (2021) outline the procedure for checking this beam shear yielding limit state [Figure 1(b)]. In their design example of a seismic frame, they use CSM to check beam yielding [Figure 1(b)] in order to ensure that brace yielding actually governs [Figure 1(a)].

In the paper, the authors cite previous work where finite element models were used to investigate beam shear demands in chevron frames (Richards et al., 2018). While results from those finite element (FE) models were consistent with the CSM design method, those FE models were somewhat limited in their ability to predict post-yield behavior.

The publication of Sabelli and Saxey (2021), including their thorough design example (CSM example), provided an opportunity for more robust FE validation. To determine the accuracy of their equations for checking beam shear yielding, FE analysis was performed on a model based on their design example. In the CSM example, the beam was capacity-designed based on the maximum forces that could be delivered by the braces [Figure 1(a)], but in the FE model, the braces were given unlimited strength to force the beam shear yielding mechanism [Figure 1(b)] to develop. The FE model answered three questions:

- Was the CSM used by Sabelli and Saxey (2021) accurate?
- What load would have caused shear yielding in the beam?
- What would have happened if a beam shear mechanism developed?

The answers to the first two questions are pertinent for new design. The answer to the last may be pertinent for some existing braced-frames where beam local shear yielding was not checked during design.

This discussion will describe the FE model and discuss the CSM example in the context of the FE model results.

Paul Richards, Vice President of Research and Development, DuraFuse Frames, West Jordan, Utah. Email: paul.richards@durafuseframes.com

Paper No. 2021-01D

FINITE ELEMENT MODEL

The geometry of the FE model matched that of the CSM example [Figure 2(a)]. The example frame connection had a W24×94 beam with gussets that had a 0.75 in. thickness and a 56 in. effective length (the gusset was 58 in. long, but the weld was held back 1 in. from each end). The four braces framing into the beam had an angle of 50.2° off horizontal. Figure 1(b) shows the maximum expected brace forces. The horizontal components in the lower story sum to 782 kips. The gusset was proportioned to be just long enough to preclude beam shear yielding under these forces (based on the CSM). The gusset-to-beam welds were ½ in. for the end segments (14 in. each end) and 5/16 in. for the 28 in. in the middle.

The FE model was developed and analyzed with ANSYS (2022). Three types of elements were used in the model to represent various components efficiently. The gusset plates, brace ends, welds, and beam (in the connection region) were

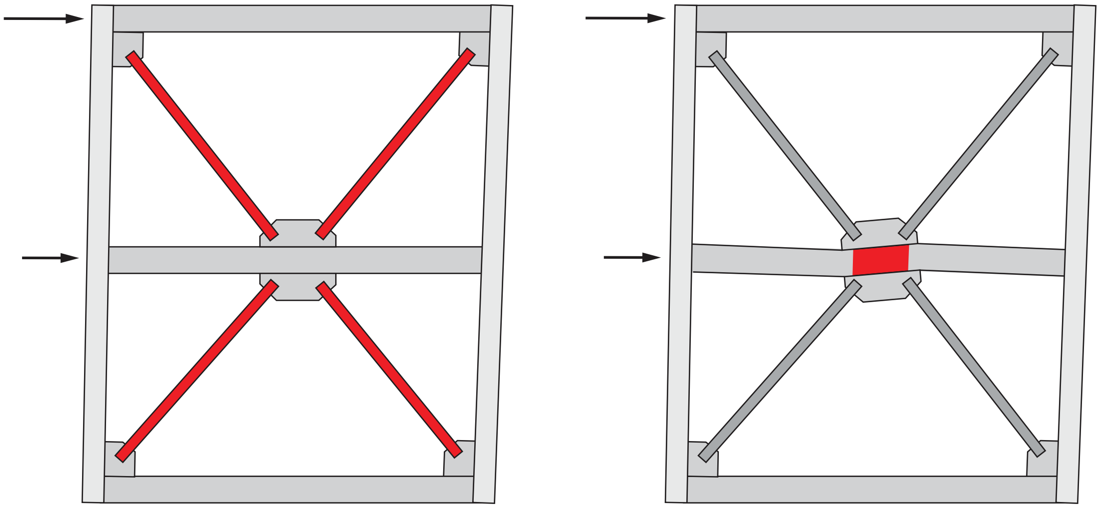
(a) Brace tension/compression yielding

(b) Beam shear yielding

Fig. 1. Braced frames with different governing limit states.

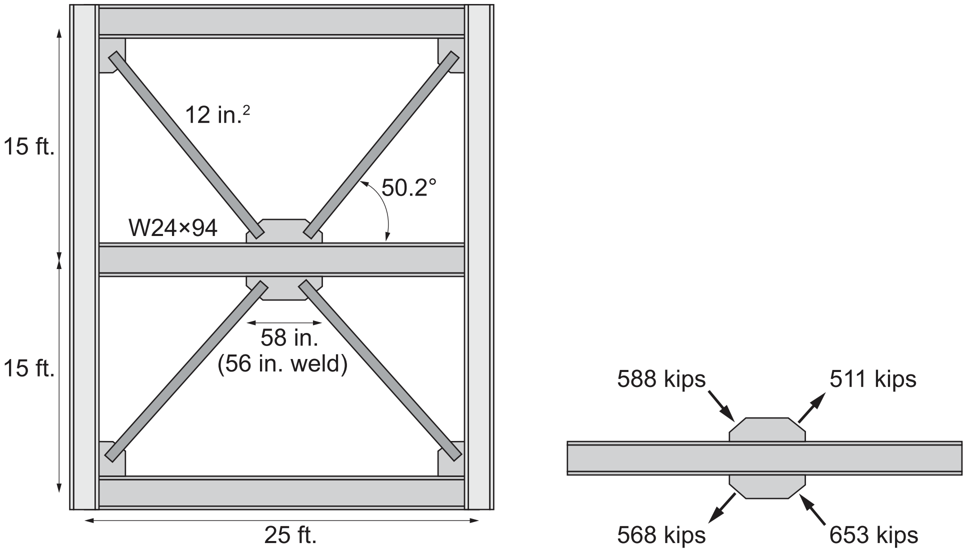

(a) Geometry

(b) Design loads

Fig. 2. Frame from the CSM example.

modeled with solid elements (SOLID186) [Figure 3(a)-(c)]. The beam mesh in the connection region had an element dimension of 1 in. [Figure 3(b)]. The gusset-to-beam welds were modeled explicitly [Figure 3(c)]. Outside the gusset region, the beam was represented with elastic beam elements (BEAM188) [Figure 3(a)] with the cross-sectional properties of a W24×94. The braces were represented with elastic truss elements (LINK180) to force the beam shear yielding mechanism to form. Effective areas were used for the brace elements so that the magnitudes of the brace forces (relative to each other) would match the relative magnitudes of the forces in the design example [Figure 2(b)].

The boundary conditions and loading in the model were for a pushover-type analysis [Figure 3(a)]. The bottom nodes of the bottom braces were pinned in space. The beam ends and top brace nodes were on rollers that prevented movement in the *y*-direction and had displacements imposed in the *x*-direction. The relative magnitudes of the top and bottom applied displacements [0.526*x* in Figure 3(a)] were calibrated so that the magnitudes of the brace forces in the two stories would match the relative magnitudes of the forces in the design example [Figure 2(b)]. Out-of-plane restraint was applied to all nodes, including the beam web and gusset.

The materials in the FE model simulated nominal steel and weld properties. In the CSM example, the beam and gusset were Grade 50 material. In the FE model, the gusset and beam material had an elastic modulus of 29,000 ksi, a Poisson's ratio of 0.3, a yield stress of 50 ksi, and a post-yield modulus of 290 ksi (1% of elastic). A capping stress of 65 ksi was set, after which the material had negligible further hardening. The weld material in the FE model had an elastic modulus of 29,000 ksi, a yield stress of 70 ksi, and negligible further hardening. These material models, with nominal material strengths, were appropriate for comparison with design procedures that assumed nominal material strength.

The FE model was pushed to a point beyond where the beam shear mechanism was fully developed. Figure 4 shows the pushover curve, where the lateral force is the total applied load on the frame. Figure 4 shows six particular load points, and Table 1 summarizes the significance of each point. Figures 5 through 9 show stress and strain information corresponding to those particular points.

The evolution of the von Mises stress is shown in Figure 5. At a load of 616 kips [Figure 5(a)], there was a region of the beam web at midspan where the von Mises stress exceeded 50 ksi. This region propagated until it reached the extents of the gusset around 815 kips [Figure 5(d)]. At 873 kips [Figure 5(e)], the von Mises stress exceeded 50 ksi for a continuous region of the gusset plate between brace ends. The von Mises plot at 1024 [Figure 5(f)] shows regions with stresses over 55 ksi, reflecting strain hardening.

The evolution of the plastic strains is shown in Figures 6 and 7. At a load of 616 kips [Figure 6(a)], there were no plastic strains greater than 0.002. At 782 kips [Figure 6(c)], localized plastic strains in the beam coalesced to form a full-depth region of the beam web at midspan with plastic strain over 0.002. This plastic region expanded toward the gusset edges. At 873 kips [Figure 6(e)], most of the beam in the gusset region was plastic, as well as a region of the bottom gusset plate between the braces. Figure 7 shows closeup views of the gusset-to-beam weld at the same points. At 1024 kips [Figure 7(f)], the plastic regions of the weld extended 4 in. in from the ends of the weld (beam elements have a 1 in. dimension in the figure), and peak plastic strains exceeded 0.1.

Figure 8 shows the evolution of the shear stresses in the beam and gussets. In the beam, the shear stress exceeded

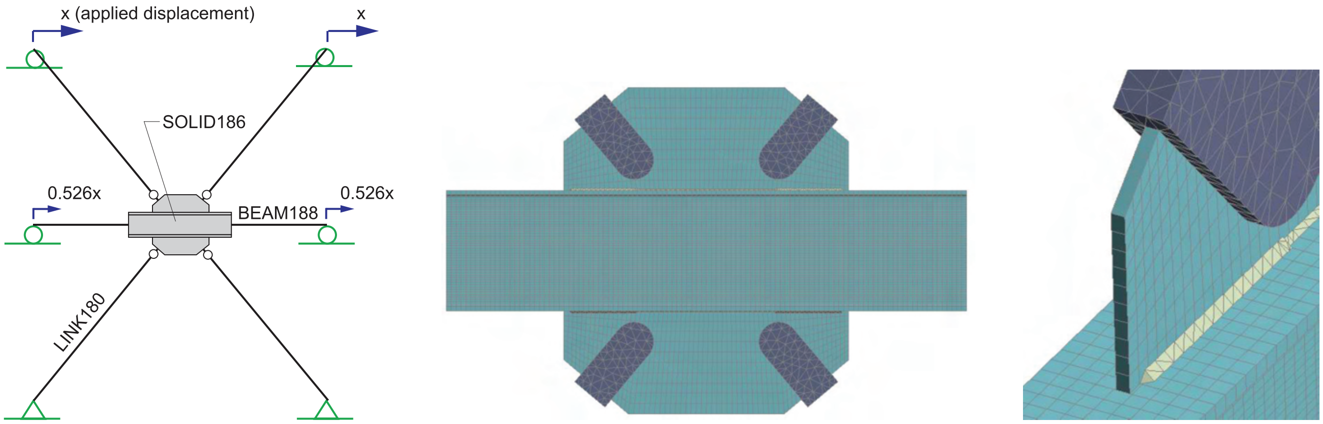

(a) Element types and boundary conditions

(b) Solid element mesh in the connection region

(c) Explicit modeling of the welds

Fig. 3. Finite element modeling techniques.

Table 1. Pushover Points for Discussion

Point	Load (kips)	Significance
a	616	Von Mises stress exceeded 50 ksi in a localized region of the beam web.
b	744	Localized plastic strains exceeded 0.002 in the beam web and gusset-to-beam welds.
c	782	Localized plastic strains in the beam, over 0.002, coalesced to a full-depth region of the beam web.
d	815	Von Mises stress exceeded 50 ksi for a continuous region between braces in the bottom gusset. Change in tangent stiffness.
e	873	Shear stresses exceeded 30 ksi ($0.6F_y$) for a full-depth region of the beam web.
f	1024	Maximum load was applied.

25 ksi at midspan when the applied lateral load was 616 kips [Figure 8(a)], and the elevated region expanded as the loads increased. However, the shear stress in the beam web did not exceed 30 ksi through an entire section until the load was 873 kips [Figure 8(e)].

At all stages of loading, the shear stresses in the gusset were highest at midspan and decreased near the gusset ends. In fact, the shear stresses changed sign in the regions at the end of the gusset [Figure 8; signs changed at interface of light blue and medium blue], a finding that was documented in Richards et al. (2018). The gusset locations where the shear stress changed sign corresponded with the regions with high normal stress (Figure 9).

Figure 9 shows the evolution of y-direction normal stresses in the beam and gussets, which were generally low. For most regions, the normal stresses were between ±20 ksi throughout loading. For loading of 744 kips and above [Figure 9(b)–(f)], regions of concentrated normal stress (above 20 ksi) developed at the ends of the gusset plates. Normal stresses above 50 ksi developed at the highest levels of loading considered.

DISCUSSION

In the CSM example, the effective gusset length of 56 in. was selected to preclude beam yielding under a lateral force of 782 kips (the maximum force that could be delivered by the braces). If the CSM were accurate, the beam shear yielding limit state would be observed in the FE model at a load slightly greater than 782 kips.

The results in Figure 4 through 10 indicate that the beam shear yielding limit state was reached at a load a little greater than 782 kips. The pushover plot (Figure 4) shows softening around 782 kips that continued to develop

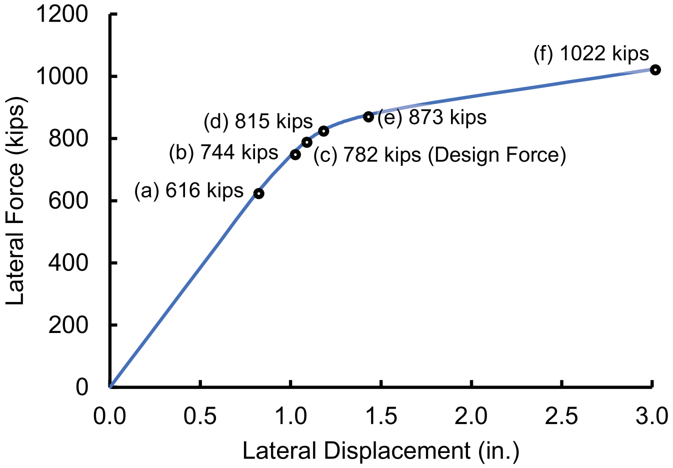

Fig. 4. Pushover curve for the finite element model.

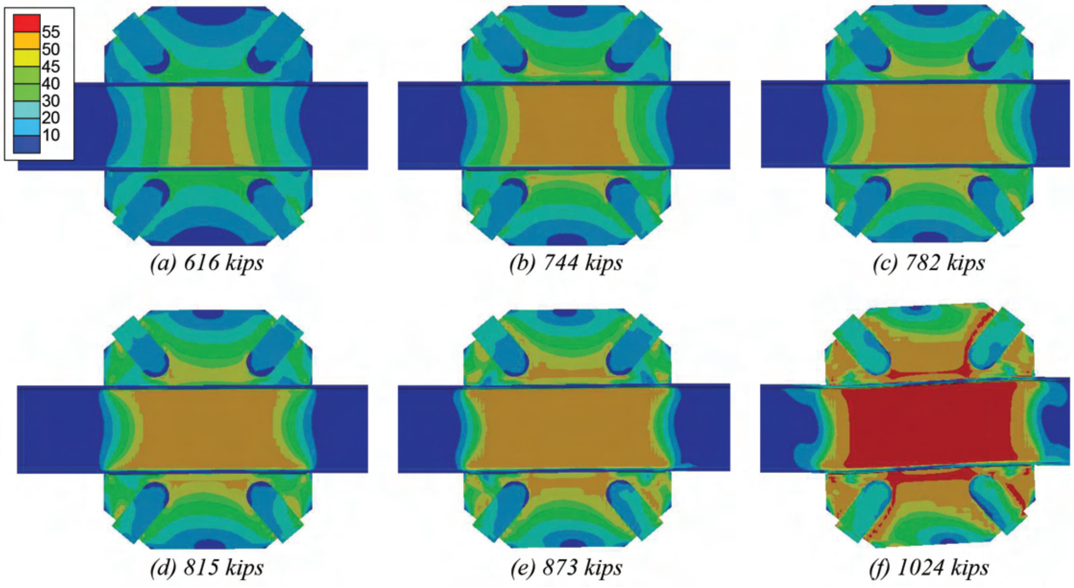

Fig. 5. Equivalent (von Mises) stress (ksi) contours in the beam and gussets.

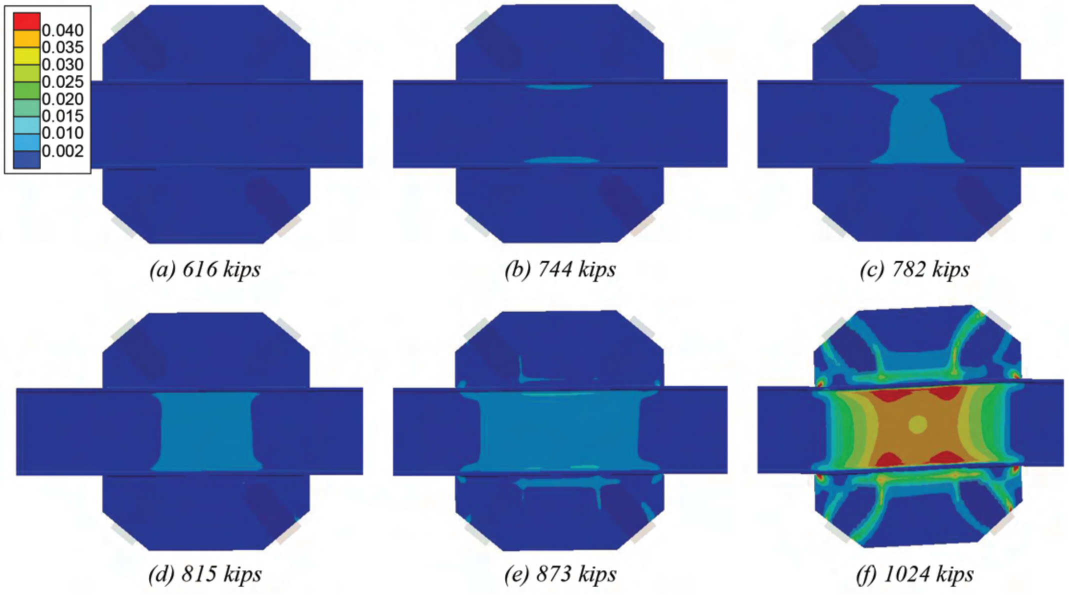

Fig. 6. Plastic strain contours in the beam and gussets.

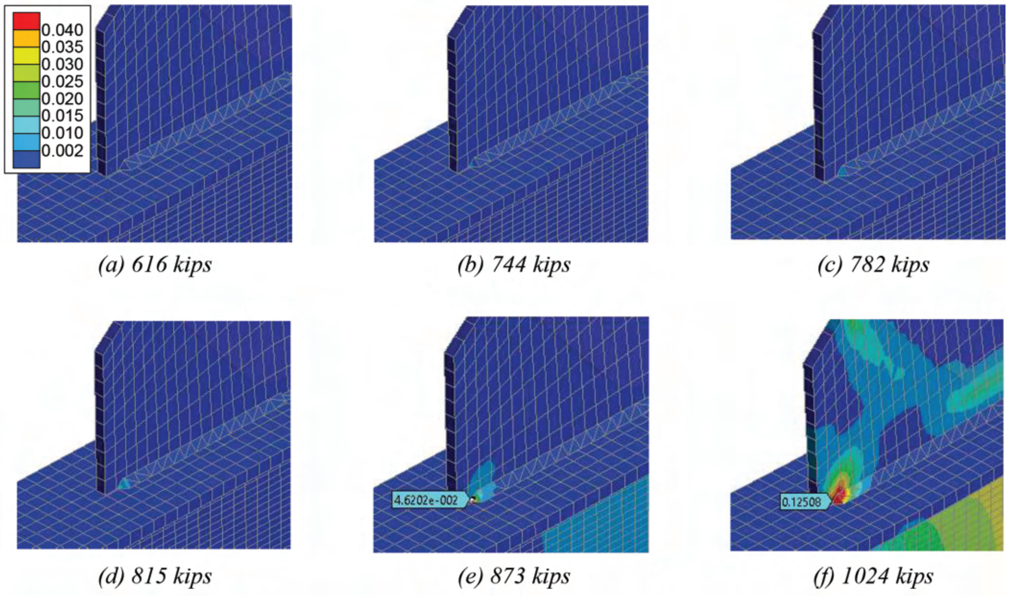

(a) 616 kips (b) 744 kips (c) 782 kips

(d) 815 kips (e) 873 kips (f) 1024 kips

Fig. 7. Plastic strains at the gusset-to-beam welds (beam flange elements have 1 in. edge length).

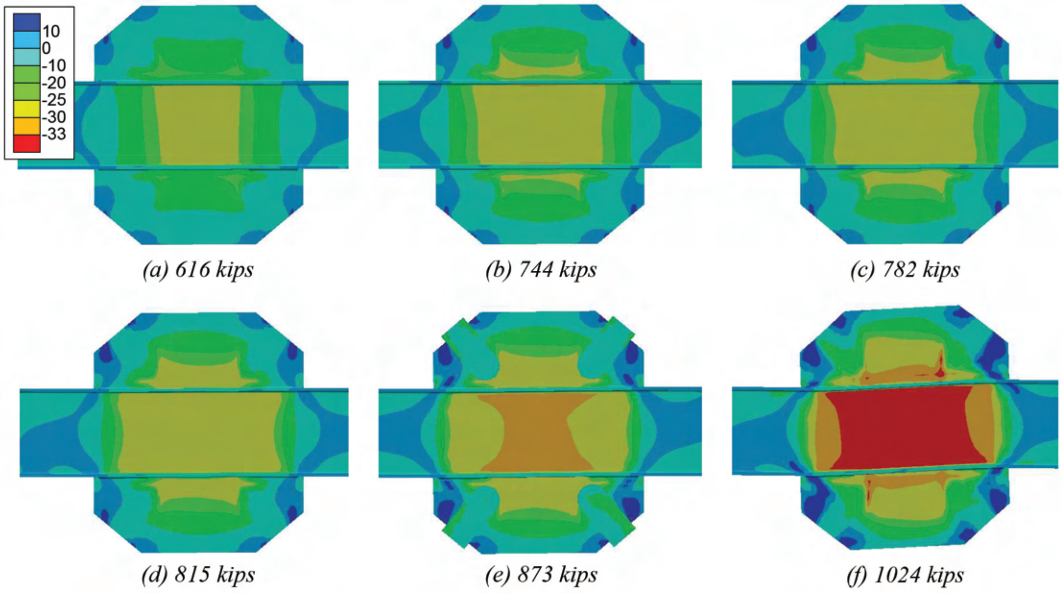

(a) 616 kips (b) 744 kips (c) 782 kips

(d) 815 kips (e) 873 kips (f) 1024 kips

Fig. 8. Shear stresses (ksi) in the beam and gussets.

to the stable post-yield stiffness by 873 kips. The plastic strain plot [Figure 6(c)] shows that at 782 kips, localized plastic strains above 0.002 had coalesced at the center of the beam. These strains propagated outward, with the beam web yielding being fully developed by 873 kips.

It is difficult to quantify precisely where the beam shear yielding limit state was reached, but Figure 10 offers additional insight. Figure 10 shows the tangent stiffness, k_t, normalized by the elastic stiffness $k_{elastic}$ for the different levels of lateral force. There appears to be an inflection point around 815 kips that suggests that the yielding is mature. As a sidenote for Figure 10, the stabilized post-yield stiffness (lateral forces greater than 900 kips) was about 10% of the elastic stiffness, even though the material hardening was only 1% of elastic because of the ratio of plastic beam rotation to story drift (to be discussed in the next section).

All these results support the conclusion that the CSM used by Sabelli and Saxey (2021) is reasonable for design.

The stress and strain contours in Figures 7 through 9 suggest some refinements for the CSM. In the CSM example,

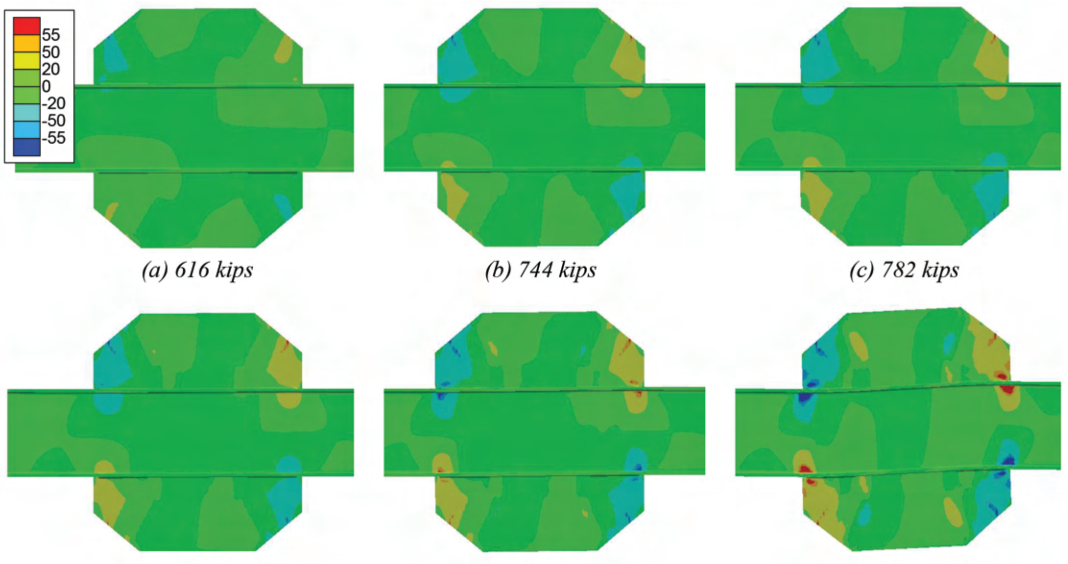

(a) 616 kips

(b) 744 kips

(c) 782 kips

(d) 815 kips

(e) 873 kips

(f) 1024 kips

Fig. 9. Normal stresses (ksi) in the beam and gussets.

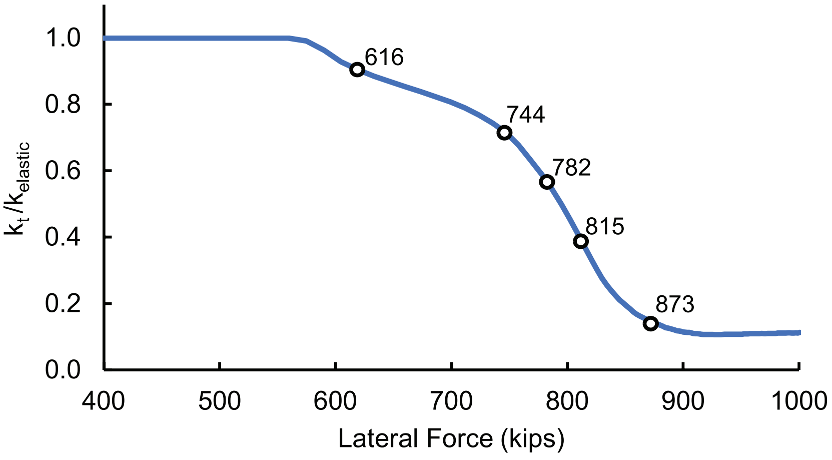

Fig. 10. Normalized tangent stiffness corresponding to various levels of lateral force.

a z_1 distance of 7.38 in. was used in design to designate the region of the gusset that is assumed to resist the moment at the connection through concentrated normal stresses. The FE model (Figures 7 and 9) indicated that the actual region of concentrated normal stress was somewhat smaller, more like 5.0 in. Another point of possible refinement is the assumption of the length that is effective for shear transfer. In the CSM example, the gusset-to-beam shear is assumed to be transferred evenly over the entire length of the gusset plate. The FE model demonstrated, as did Richards et al. (2018), that z regions did not transmit much shear. A refined CSM, with smaller z and shear transfer only in-between z regions, may better predict the demands on the gusset-to-beam welds.

BROADER DISCUSSION OF BEAM SHEAR YIELDING AND COMPARISON TO EBF

The CSM example frame would not be expected to experience significant beam yielding because the forces that could be delivered by the braces were lower than the forces required to reach the beam shear limit state. However, there may be other braced frames where local shear demands were not considered in the design and a beam yielding mechanism might occur. It is also possible that someone might contemplate a new seismic system that intentionally yields the beam. In those contexts, results about the extreme post-yield behavior of concentrically braced frames with beam yielding may be of interest.

The evolution of the shear stress in the beam web (Figure 8) is similar to that documented in experimental and finite element studies of shear-yielding links in eccentrically braced frames (EBF) (Hjelmstad and Popov, 1983; Richards et al., 2007). In discussing the post-yield behavior of a concentrically braced frame (CBF) with beam yielding, it is informative to compare and contrast with an EBF. An EBF FE model was developed to make comparisons with the CBF FE model as an academic exercise, see Figure 11.

The EBF model did not represent a code-compliant seismic design, just as the CBF model with a yielding beam did not represent a code-compliant seismic design. The purpose of the academic exercise was to compare and contrast beam yielding mechanisms. The EBF FE model had the same beam size (W24×94), beam length, and story heights as the CBF (Figure 5). The length of the shear link was 44 in. to match the observed intense yielding region in the CBF [Figure 5(f), red region]. The braces were modeled with elastic truss elements (infinitely strong, LINK180). As with the CBF model, the beam web and gusset plates were restrained against out-of-plane deformations, so stiffeners in the link beam or on the gussets were not necessary in the model. The nonlinear material properties for the beam were the same in the EBF model as they were in the CBF.

Figure 12 compares the inelastic pushover curves for both models. Results are shown up to an inelastic drift of 0.004. The lateral force that was required to yield the EBF was substantially lower than for the CBF with the same beam size because the eccentricity of the brace work points in the EBF was a more direct and effective way to impose shear on the beam web. Also, the CBF gussets help to carry some shear, as determined using the CSM. The lower post-yield stiffness in the EBF was a reflection of lower strains in the beam (less strain hardening).

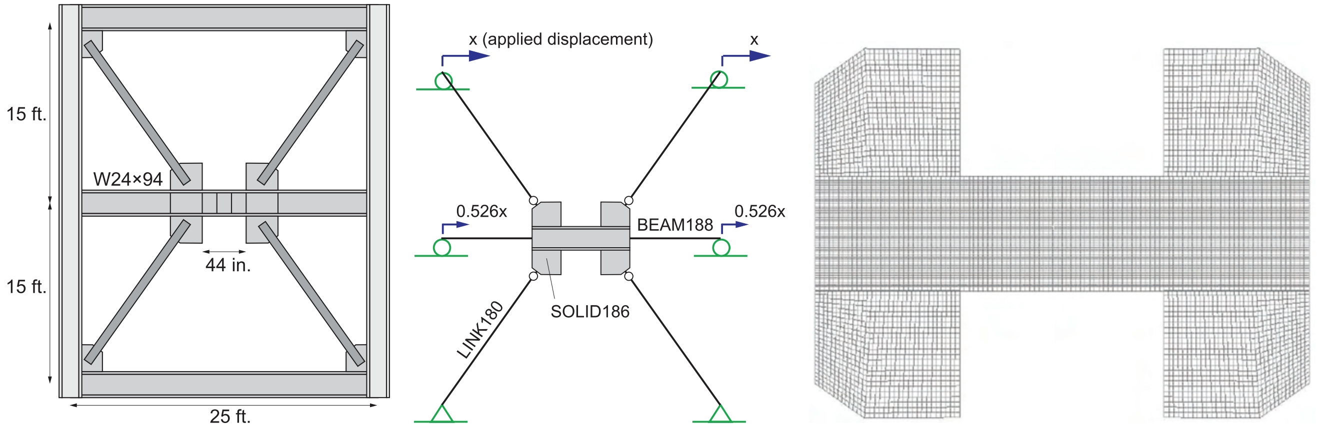

(a) Geometry *(b) FE model boundary conditions* *(c) FE mesh*

Fig. 11. EBF frame for comparison with the CBF.

Figure 13 compares the inelastic beam rotations versus the inelastic story drift for CBF and EBF. The EBF relationship between inelastic beam rotation and inelastic drift was within 13% of an estimate from a rigid plastic mechanism (Figure C-F3.4, AISC, 2016). The higher inelastic beam rotations for the CBF for a particular inelastic drift would make the CBF less attractive than EBF for an intentional beam yielding mechanism unless high post-yield stiffness were the primary aim.

Figure 14 compares the plastic strains and deformed geometries of both models at 0.004 rad inelastic story drift. The displacements have been scaled by a factor of 6 in both cases to illustrate the plastic mechanisms. The maximum web plastic strain in the CBF (0.035) is 75% more than the maximum plastic strain in the EBF (0.020) at the same inelastic drift. Also, the plastic strains are more uniformly distributed in the EBF.

The plastic mechanism in Figure 14 has the same form as the one postulated by Sabelli and Bolin (2022), where the plastic section of the beam is less than the full length of the gusset. The plastic strains in the gusset in Figure 14(a), including the concentrations of strain at the ends, illustrate the gusset/weld deformations required for compatibility with the yielding beam.

This academic exercise demonstrates that it is theoretically possible to design a CBF with a beam yielding mechanism, even though current seismic design provisions do not allow it. There are advantages and disadvantages of CBF

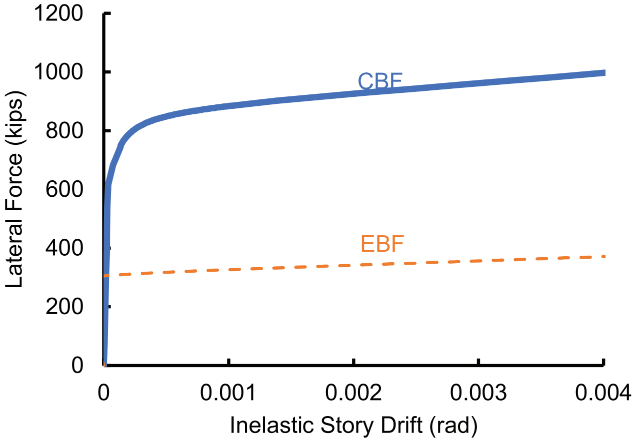

Fig. 12. Inelastic story drift vs. lateral force for CBF and EBF.

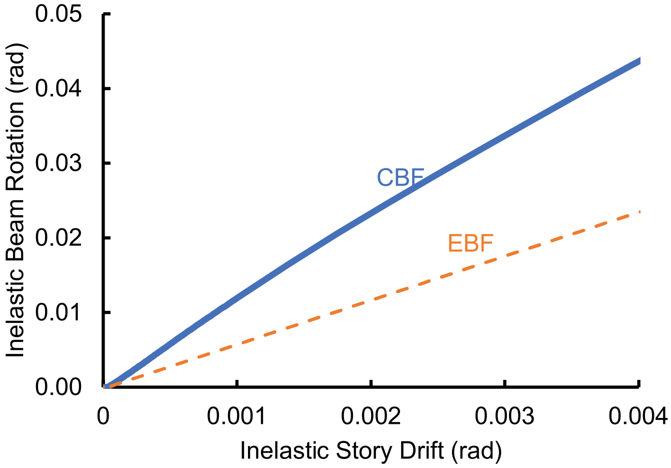

Fig. 13. Inelastic beam rotation vs. inelastic story drift for CBF and EBF FE models.

with beam yielding as compared to an EBF. The CBF advantages are greater elastic stiffness, strength, and post-yield stiffness. The CBF disadvantages are higher beam rotation and higher beam strains to achieve a particular inelastic drift (although less inelastic drift might be required for a CBF since the elastic stiffness is greater).

If existing chevron frames have been unintentionally designed such that yielding would occur in the beam web, these analyses demonstrate the expected plastic mechanism.

CONCLUSIONS

A finite element (FE) model was developed to investigate the design procedure presented by Sabelli and Saxey (2021). The braces in the model had unlimited strength to force a beam-yielding mechanism to occur. A pushover analysis was performed to check if the Concentrated Stress Method (CSM) used by Sabelli and Saxey (2021) in their CSM example was accurate in predicting the beam shear yielding limit state. Here are the conclusions from the exercise:

- The CSM used by Sabelli and Saxey (2021) was reasonable for design. The FE model confirmed that the CSM example frame would not have experienced a beam yielding limit state under the design forces (maximum forces that could be delivered by the braces).
- While there was not a clear method for defining when the beam yielding limit state was reached in the FE model, an inflection point for the tangent stiffness suggested about 815 kips, which was 4% higher than the design force used in the CSM example.
- The method for estimating the *z* regions in the CSM example might be refined. A higher value for *z* was used in the CSM example than observed in the FE model.
- The method for assigning regions of the gusset to transmit shear in the CSM example might be refined. In the CSM example, shear was assumed to be transmitted along the entire length of the gusset, but the FE models indicate the *z* regions are not effective for shear transfer.

An additional FE model of an EBF was used for an academic exercise, comparing the post-yield plastic mechanism of a CBF (with beam yielding) with an EBF with the same beam. This discussion was outside the scope of Sabelli and Saxey (2021) but pertinent to the broader topic of local member shear demands. Conclusions were as follows:

- The CBF FE model developed the plastic mechanism discussed by Sabelli and Bolin (2022) and confirmed their assumption that the yielding region of the beam was shorter than the total gusset length.
- The shear yielding mechanism in the CBF beam (when braces had unlimited strength), was similar to an EBF shear link; however, the lateral forces to trigger the mechanism were much higher for the CBF. At the same inelastic story drift, the inelastic beam rotation and plastic strains were higher in the CBF with beam yielding than in the EBF with the same beam size.

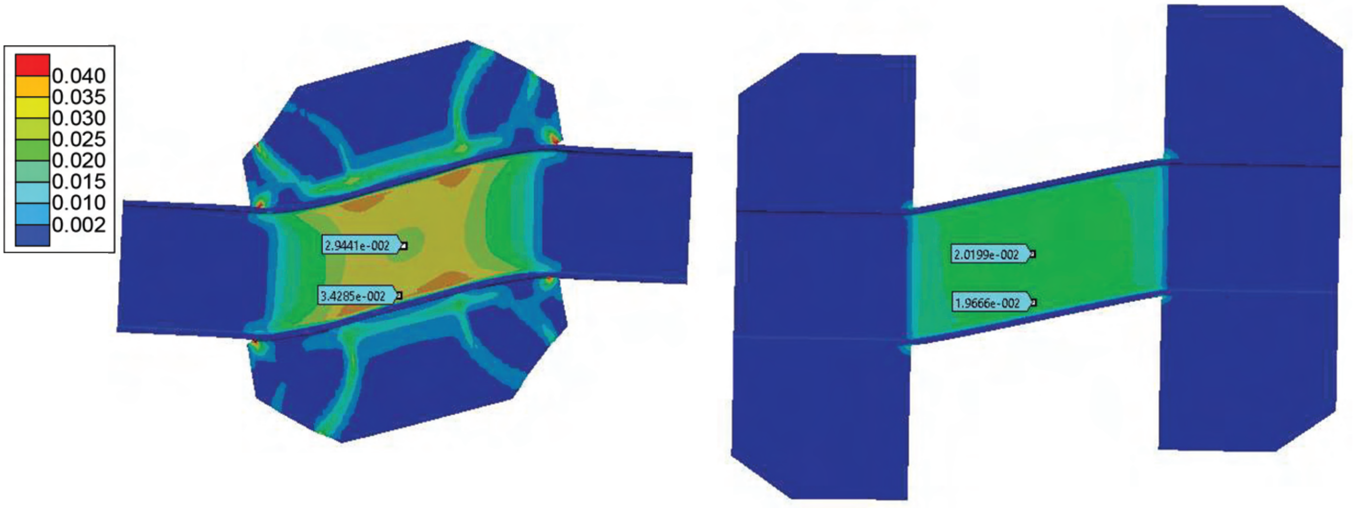

(a) Chevron *(b) EBF*

Fig. 14. Plastic strains in the chevron and EBF models at 0.004 rad inelastic story drift.

REFERENCES

AISC (2016), *Seismic Provisions for Structural Steel Buildings*, ANSI/AISC 341-16, American Institute of Steel Construction Chicago, Ill.

ANSYS (2022), Ansys Mechanical, Release 22.1, Help System, ANSYS, Inc.

Fortney, P.J. and Thornton, W.A. (2015), "The Chevron Effect—Not an Isolated Problem," *Engineering Journal*, Vol. 52, No. 2, pp. 125–164.

Fortney, P.J. and Thornton, W.A. (2017), "The Chevron Effect and the Analysis of Chevron Beams—A Paradigm Shift," *Engineering Journal*, Vol. 54, No. 4, pp. 263–296.

Hadad, A.A. and Fortney, P.J. (2020), "Investigation on the Performance of a Mathematical Model to Analyze Concentrically Braced Frame Beams with V-Type Bracing Configurations," *Engineering Journal*, Vol. 57, No. 2, pp. 91–108.

Hadad, A.A. and Thornton, W.A. (2022), "Closure: Investigation on the Performance of a Mathematical Model to Analyze Concentrically Braced Frame Beams with V-Type Bracing Configurations," *Engineering Journal*, Vol. 59, No. 1, pp. 1–4.

Hjelmstad, K.D. and Popov, E.P. (1983), "Cyclic Behavior and Design of Link Beams," *Journal of Structural Engineering*, Vol. 109, No. 10, pp. 2,387–2,403.

Richards, P.W., Miller, B., and Linford, J. (2018), "Finite Element Evaluation of the Chevron Effect in Braced Frames," SSRP-2018/02, Brigham Young University, Provo, Utah.

Richards, P., Okazaki, T., Engelhardt, M., and Uang, C.-M. (2007), "Impact of Recent Research Findings on Eccentrically Braced Frame Design," *Engineering Journal*, Vol. 44, No. 1, pp. 41–53.

Roeder, C.W., Lehman, D.E., Tan, Q., Berman, J.W., and Sen, A.D. (2021), "Discussion: Investigation on the Performance of a Mathematical Model to Analyze Concetrically Braced Frame Beams with V-Type Bracing Configurations," *Engineering Journal*, Vol. 58, No. 1.

Sabelli, R. and Bolin, E. (2022), "The Chevron Effect: Reserve Strength of Existing Chevron Frames," *Engineering Journal*, Vol. 59, No. 3, pp. 209–224.

Sabelli, R. and Saxey, B. (2021), "Design for Local Member Shear at Brace and Diagonal-Member Connections: Full-Height and Chevron Gussets," *Engineering Journal*, Vol. 58, No. 1, pp. 45–78.

Sabelli, R., Saxey, B., Li, C.-H., and Thornton, W. A. (2021), "Design for Local Web Shear at Brace Connections: An Adaptation of the Uniform Force Method," *Engineering Journal*, Vol. 58, No. 4, pp. 223–266.

Effects of Accident Thermal Loading on In-Plane Shear Behavior of Steel-Plate Composite Walls

Saahastaranshu R. Bhardwaj, Kadir C. Sener, and Amit H. Varma

ABSTRACT

Structural walls in safety-related nuclear facilities are required to be designed for seismic and accident thermal (due to postulated high-energy pipe break events) loading combination. Current U.S. and international codes provide limited guidance for analysis and design of walls for this loading combination. This paper describes the experimental results and observations from tests conducted on a laboratory-scale (1:4 to 1:5) test unit representing steel-plate composite (SC) walls subjected to combined in-plane (seismic) and accident thermal loading. The test unit was subjected to surface temperatures of up to 450°F in combination with cyclic in-plane loading. Results of similar experiments recently conducted in Japan are also summarized (with surface temperatures up to 570°F). Surface heating combined with the low thermal conductivity and high specific heat of concrete resulted in nonlinear thermal gradients through the thickness of the specimens. These nonlinear thermal gradients and the associated self- or internal restraint led to extensive concrete cracking. This concrete cracking reduced the initial and secant stiffness of the specimens. The initial stiffness of the heated specimens reduced to 30 to 40% of the initial stiffness of the control (unheated) specimen. The secant stiffness of the heated specimens reduced up to 50% of the secant stiffness of the control (unheated) specimen. However, the in-plane shear strength of the heated SC specimens was still approximately 10 to 30% greater than the nominal in-plane shear strength calculated, for the limit state of steel plate von Mises yielding, using AISC N690 equations and measured material properties. Evaluation of the experimental results and observations suggests that the in-plane shear strength of SC walls subjected to typical accident surface temperatures (up to 570°F) can be estimated conservatively using the current provisions of AISC N690. The stiffness for accident thermal loading combinations can be considered to reduce from cracked composite stiffness at ambient temperature to fully cracked—that is, steel-only stiffness as the surface temperature increases up to typical accident value.

Keywords: steel-plate composite, structural walls, accident thermal, seismic, in-plane shear, shear stiffness, flexural stiffness.

INTRODUCTION

Strutural walls in safety-related facilities may be a part of labyrinthine structures (with cross-walls, typical to nuclear construction), or stand-alone shear walls [typical in Department of Energy (DOE)–type nuclear facilities or commercial construction]. These structural walls may be reinforced concrete (RC) or steel-plate composite (SC) walls depending on the overall structure or plant design. While RC walls have been traditionally used, SC structures are also being used for the third generation of nuclear power plants and being considered for small modular reactors (SMR) of the future. SC walls are comprised of structural steel modules filled with plain concrete. The modules consist of two steel faceplates that form the opposite surfaces of the wall and define its total thickness. The faceplates are connected to each other using ties spaced uniformly in both the vertical and horizontal directions. These ties consist of steel rods or structural shapes (angles, channels, plates, etc.) that are typically welded to the steel faceplates. The ties provide structural stability during transportation, handling, and erection. Steel headed stud anchors may be welded to the interior surfaces of the steel faceplates. Stud anchors and/or ties provide composite action, faceplate local buckling restraint, and anchorage to the infill after concrete placement. The ties also provide composite action and anchorage to the concrete infill and serve as out-of-plane shear reinforcement for the composite SC walls. The steel modules—consisting of faceplates, ties, and stud anchors—can be prefabricated in the shop, transported to the site, assembled into larger modular structures, and then filled with plain concrete, thus leveraging modular construction approaches to expedite construction schedule and optimize overall project costs (NRC, 2011, 2012; Schlaseman and Russell, 2004).

Advantages of modular SC walls in terms of structural efficiency and construction economy (Varma et al., 2015; Sener et al., 2015b; Booth et al., 2015; Bruhl et al., 2015;

Saahastaranshu R. Bhardwaj, Assistant Professor, University of Alabama, Tuscaloosa, Ala. Email: saahas.bhardwaj@ua.edu (corresponding author)

Kadir C. Sener, Assistant Professor, Auburn University, Auburn, Ala. Email: sener@auburn.edu

Amit H. Varma, Karl H. Kettelhut Professor and Director of Bowen Laboratory, Purdue University, West Lafayette, Ind. Email: ahvarma@purdue.edu

Paper No. 2022-05

ISSN 0013-8029

Bruhl and Varma, 2018) have led to the SC walls being considered for commercial construction. There has been recent research on the commercial building application of SC walls with boundary elements (Selvarajah, 2013; Bruneau et al., 2013; Ji et al., 2017; Varma et al., 2017). The current building codes, namely, ASCE 7 (ASCE, 2022) and AISC 341 (AISC, 2016), permit the use of composite plate shear walls-concrete filled (C-PSW/CF), with boundary elements, in seismic regions (Bruneau et al., 2013; Alzeni and Bruneau, 2014).

There are some significant differences between SC walls used in safety-related nuclear facilities and those used in commercial building projects. Safety-related nuclear facilities are labyrinthine in plan and consist of numerous cross-connecting, intersecting, squat (or short) SC walls with height-to-length ratios less than 1.0. There are typically no other structural frames or lateral force-resisting systems besides this network of SC walls. Commercial building structures typically use steel gravity frames and a lateral force-resisting system for wind and seismic loads. The lateral-force resisting system may consist of individual SC walls (with or without boundary elements) as distributed shear walls or coupled composite SC shear walls with adequate coupling action. In both cases, the SC walls are tall slender structures with height-to-length ratios greater than 3.0 and are governed by their in-plane flexure behavior. Another major difference is that SC walls in safety-related nuclear facilities have to be designed for the accident thermal plus seismic loading combination as specified in the *Code Requirements for Nuclear Safety-Related Concrete Structures and Commentary* (ACI 349, 2013), the *Specification for Safety-Related Steel Structures for Nuclear Facilities* (AISC N690, 2018), and the U.S. Nuclear Regulatory Commission's RG 1.142 (NRC, 2020) and RG 1.243 (NRC, 2021). During this challenging design-basis load combination, the facility is expected to shut down safely, which requires all the equipment to function and the structure to respond with limited inelastic deformations. The SC structure stiffness and strength during the combined accident thermal plus seismic loading combination are required to check the structure design strength against the design demands calculated using appropriate models and to verify the in-structure response spectra for equipment performance. The Fukushima nuclear accident of 2011 emphasized the importance of this design-basis load combination. Although the probability of multiple design-basis events occurring simultaneously is low, severe impact of one hazard may trigger other hazards; for example, earthquake shocks may lead to accident thermal events. Subsequent aftershocks (potentially as intense as the main shock) may occur during the accident thermal event. This load combination of accident thermal loading and safe shutdown earthquake (SSE) also presents a significant design challenge for small modular reactors (SMRs) since postulated accident scenarios may cause higher magnitudes of elevated temperatures for longer durations in their smaller constrained spaces.

Current design codes and standards offer limited procedural guidance for including the effects of accident thermal loading on seismic behavior (stiffness, strength, ductility, or reserve margin) of structures. Existing research focuses on the individual effects of either seismic or accident thermal loading, but not the combination of these loads. There is a need to develop design guidelines (based on experimental and numerical studies) for structural walls subjected to combined accident thermal and seismic loading.

This paper presents an experimental evaluation of the seismic (in-plane) behavior of squat SC wall specimens (with boundary elements) subjected to typical accident temperatures for Generation III pressurized water reactors (PWRs). Since the behavior of SC walls (with boundary elements or flanges, which may be cross-SC walls or closure steel flange plates, as seen in Figure 3) is fundamentally different from the behavior of SC wall piers (without boundary elements) (Kurt et al., 2016), the evaluation of SC wall piers for combined seismic and thermal loading is presented in Bhardwaj et al. (2019a). The authors have also conducted similar studies for RC beams (Sener et al., 2019a) and RC walls (Bhardwaj et al., 2018; Anwar et al. 2019). This paper first discusses relevant research conducted on SC walls subjected to individual hazards like seismic and accident thermal loads. Recent experimental studies conducted in Japan on SC walls subjected to combined thermal and seismic loading are also summarized. The paper then discusses the experimental studies conducted by authors in detail. This discussion includes the experimental approach, setup, test unit design and testing procedure, and instrumentation layout. The experimental measurements, results, and observations are used to evaluate the performance of SC walls. Results of experiments conducted by the authors, and findings reported by Japanese researchers are compared with current specifications for design of SC walls in safety-related nuclear facilities, AISC N690 (2018). These results are used to develop stiffness and strength recommendations for SC walls subjected to combined seismic and thermal loads.

BACKGROUND

In the past, experimental and numerical research was conducted to evaluate the response of SC walls to seismic (in-plane) loading. Numerical studies were conducted to investigate the effect of accident thermal loading on SC structures. The existing body of research on the in-plane response of SC walls, and material and structural response to accident thermal loading are discussed in this section.

In-Plane Loading

For SC walls, in-plane flexure (bending moment) is primarily resisted by the boundary elements (flanges—e.g., cross SC walls or steel flange plates). In-plane shear is resisted primarily by the web of the wall. The in-plane shear behavior of SC walls was developed by Ozaki et al. (2004) and extended by Varma et al. (2014). The in-plane behavior can be represented by a tri-linear shear force–strain (S_{xy}–γ_{xy}) curve. As described in Ozaki et al. (2004) and Seo et al. (2016), the in-plane response of SC walls can be defined by a mechanics-based behavior model (MBM) that uses composite plate theory. The in-plane behavior was idealized into three parts: (1) before concrete cracking, where concrete and steel plates are elastic and perfect bond between them can be assumed; (2) post-cracking, where cracks form in the concrete while steel plates remain elastic; and (3) post-yield, where faceplates undergo von Mises yielding. The in-plane shear strength (based on von Mises yielding) and stiffness (tripartite stiffness) requirements in AISC N690 (2018) are based on the trilinear MBM. Seo et al. (2016) verified the tri-linear curve using a large in-plane shear test experimental database and observed that AISC N690 equations estimated the in-plane strength conservatively.

Booth et al. (2020) demonstrated that SC walls have additional in-plane strength beyond the von Mises yielding of faceplates. The authors provided mechanics-based equations for calculating the ultimate in-plane shear strength, V_u, of SC walls. This additional post-yield shear resistance is provided by the concrete compression strut (concrete arch action) that develops along the compression diagonal and is anchored into the boundary elements. The post-yield strength contribution depends on the compression capacity of the concrete diagonal strut, which is subjected to crack opening by the transverse tensile strain field, and the strength of the boundary elements and the connection between the wall (web) and boundary elements to anchor and resist the thrust being delivered by the concrete compression diagonal strut.

Thermal Loading

Structural walls in safety-related nuclear facilities may be subjected to accident thermal loads due to postulated high-energy pipe break events in pressurized water reactors. These accidents result in thermal and pressure loading on the walls. This article focuses on the effect of thermal loading on the in-plane shear behavior of SC walls. Accident pressures may result in out-of-plane loading on the walls. Behavior of SC wall piers under biaxial loading (in-plane and out-of-plane loading) is discussed elsewhere in Bhardwaj et al. (2019b). For accident thermal loading, thermal-hydraulic analyses are conducted to estimate the temperature histories (*T-t* plots) for the surfaces of walls exposed to accidents. Sener et al. (2015a) identified and developed typical accident temperature-time histories for the containment internal structure of pressurized water reactors using the envelopes of *T-t* histories published in design control documents for various plant designs. The *T-t* curves used for this experimental study were representative of these typical accident temperature-time histories.

The surface *T-t* curve, and concrete and steel thermal properties govern the evolution of the through-thickness nonlinear thermal gradients for the walls. The thermal and mechanical properties of steel and concrete depend on the associated temperature. Significant research has been conducted on the change in steel and concrete properties at elevated temperatures (Hong and Varma, 2009; Naus, 2009; Takeuchi et al., 1993; Kodur et al., 2010). However, most of the research has focused on elevated temperatures associated with fire scenarios that are significantly higher (1500–1800°F) than typical accident temperatures (up to 570°F) in safety-related nuclear facilities. The recommendations for steel and concrete material properties at elevated temperatures are provided in Eurocode 2 and 3 (CEN, 2004, 2005) and AISC N690 (AISC, 2018). For the range of accident temperatures (up to 572°F), the steel yield and tensile strength values do not reduce. However, the steel stress-strain curves become nonlinear before reaching the yield plateau, and this nonlinearity increases with increase in temperature. The modulus of elasticity of steel reduces by about 20% as the temperature increases from ambient, 68°F, to 572°F. Unlike steel, the concrete compression strength reduces considerably for the range of accident thermal temperatures. While there is no reduction for temperatures up to 212°F, the compressive strength reduces by 10% for 390°F and by 15% for 572°F. Additionally, the reduction in initial modulus of elasticity is higher for concrete than that for steel. The modulus of elasticity of concrete in compression reduces by 40% as concrete temperature increases from ambient, 68°F, to 572°F. Material properties such as the thermal conductivity, specific heat, and thermal expansion are also provided as functions of elevated temperatures in Eurocode 2 and 3.

Thermal loading on structures results in internal stresses in the walls. These thermal stresses differ from stresses generated by mechanical loads in the sense that they are generated by restraints against thermal deformations rather than to equilibrate applied loads. Thermally induced internal stresses are self-relieving—that is, thermal (tensile) stresses can be relieved as the restraint reduces due to concrete cracking, reinforcement yielding, creep, and relaxation. Bhardwaj et al. (2015) discussed the effect of accident thermal loads (from postulated pipe break scenarios) on the structural behavior of wall structures, and the evolution of through thickness nonlinear thermal gradients for accident thermal loads. During the first few hours (up to one day) of the thermal accident, structural members are subjected to significantly nonlinear thermal gradients through the thickness. These nonlinear thermal gradients induce concrete cracking due to internal or self-restraint (Sener et al., 2019a; Bhardwaj et al., 2015). After the first few days of the accident, the thermal gradients become relatively uniform through the thickness. The concrete crack widths, produced during the first few hours due to self-restraint, may reduce or even close due to the uniformity of temperatures (elimination of nonlinear gradient and corresponding internal restraint) through the thickness. Additionally, the uniform temperature magnitudes are lower than the maximum values reached earlier. However, the concrete does not regain its uncracked stiffness for mechanical loads.

This structural response to thermal loads was numerically validated by Bhardwaj et al. (2015), by subjecting 48 in. thick RC structures to idealized *T-t* curves. The response was also experimentally verified by Vecchio and Sato (1990) on an RC portal frame structure that was subjected to surface temperature change of up to 144°F from one side. The experimental results indicated that the internal forces, strains, and deformations (demands) induced by thermal loading were largest shortly after the peak surface temperatures were attained, when the nonlinearity in the thermal gradient was greatest. The thermally induced demands gradually reduced as the through-depth thermal gradient became uniform with continued heating. The test results also verified that thermally induced concrete cracking was observed in the externally unrestrained sections of the portal frame due to the internal restraints to free thermal expansion associated with the nonlinear temperature gradient. The mechanical load test results performed following thermal loading showed that the frame response was in accordance with the cracked section stiffness, and uncracked section stiffness overestimated the response significantly. Recently, Sener et al. (2019a) subjected six reinforced beam specimens to different combinations of accident thermal and out-of-plane shear loadings. The beam specimens had two different clear covers (0.75 in. and 1.5 in.), two surface temperature magnitudes (300°F and 450°F), and different heating locations (two-sided vs. one-sided, shear span vs. constant-moment region). The authors observed that section shear stiffness reduced due to thermal loading. Lower clear cover or higher surface temperatures resulted in measured shear strength values marginally lower than those calculated per ACI 349 (2013).

PREVIOUS STUDIES

Kitajima et al. (2017) have conducted experimental studies on the seismic behavior of squat (shear-critical) SC walls subjected to accident thermal loading. Details of the specimens (Specimens 2, 3, 4, 5, and 7) are presented in Table 1. The table includes the specimen height (h), length (l_w), thickness (T), faceplate thickness (t_p), flange plate thickness (t_f), aspect ratio, faceplate reinforcement ratio ($\rho = 2t_p/T$), faceplate stud spacing (s/T), faceplate slenderness ratio (s/t_p), flange plate slenderness ratio (s_f/t_f), tie spacing (S/T), faceplate (F_{yw}) and flange plate (F_{yf}) yield strengths, concrete compressive strength (f_c'), maximum surface temperature (T_{max}), lateral loading protocol (cyclic or monotonic), and duration of heating for the specimens. The tested specimens were 1:7 scale models of SC walls for the containment vessel structure. The specimens had a height-to-length ratio of 1.0, wall thickness of 11.2 in., steel faceplate thickness of 0.091 in., and flange plate (end plate) thickness of 0.87 in. The specimens were restrained against rotation at top and bottom, resulting in a shear aspect (moment-to-shear) ratio of 0.5.

These identical specimens were tested for different combinations of lateral and accident thermal loading, including (1) monotonic lateral loading at ambient temperature (Specimen 2, Control specimen); (2) monotonic lateral loading with accident temperature of 293°F, heated for 30 days (Specimen 3); (3) cyclic lateral loading with accident temperature of 293°F, heated for 30 days (Specimen 4); (4) monotonic lateral loading with accident temperature of 347°F, heated for 60 minutes (Specimen 5); and (5) monotonic lateral loading with accident temperature of 572°F, heated for 30 days (Specimen 7). The measured concrete compressive strengths, f_c', for the specimens are presented in Table 1. Kitajima et al. (2017) did not report the measured strengths for steel plates. However, the measured properties for the plate material used (SPV 490) were reported in a companion paper (Hirama et al., 2015) and have been included in Table 1.

Table 2 summarizes the measured lateral strength, $V_{n\text{-}ip}$, initial stiffness, K_{in}, and secant stiffness, K_{sec}, for specimens tested by Kitajima et al. (2017). The table also shows the reduction in strength and initial, K_{in}, and secant, K_{sec}, stiffnesses of the heated specimens in comparison with those of the ambient (control) specimen, Specimen 2. For example, $V_{n\text{-}ip}/V_{n\text{-}ip\text{-}2}$ is the ratio of measured strength of the heated specimens with respect to that of the control Specimen 2. A reduction of 15–30% in lateral strength, $V_{n\text{-}ip}$, of the heated specimens was observed with respect to the strength for control specimen. In spite of this reduction, the lateral strengths of the heated specimens were greater than the nominal strength calculated using measured properties and the AISC N690 (2018) equation for in-plane shear strength (V_n^{AISC}, corresponding to von Mises yielding of faceplates), with a safety margin ranging from 9% to 36% (as seen in Table 4, discussed later).

The initial stiffness of the heated specimens was reduced to 30–40% of the initial stiffness of the ambient (Control) Specimen 2. This significant reduction in initial stiffness

Table 1. Specimen and Test Unit Details

Identifier[1]	Height, h (in.)	Length, l_w (in.)	Thickness, T, (in.)	Faceplate Thickness, t_p (in.)	Flange Plate Thickness, t_f (in.)	Aspect Ratio	Faceplate Reinforcement Ratio, ρ	Faceplate Stud Spacing, s/T	Faceplate Slenderness Ratio, s/t_p	Flange Plate Slenderness Ratio, s_f/t_f	Tie Spacing, S/T	Faceplate F_{yw} (ksi)	Flange Plate F_{yf} (ksi)	Concrete f'_c (ksi)	Lateral Loading[2]	Maximum Surface Temperature, T_{max} (°F)	Duration of Heating (hours)
2	27.6	27.6	11.2	0.091	0.87	0.5[#]	0.016	0.16	20	2.1	N.A.	103	103	6.7	M	Ambient	NA
3														5.9	M	293	720
4														6.9	C	293	720
5														6.1	M	347	1
7														5.5	M	572	720
SC-W-H	36[3]	48	10	0.104	0.75	0.75	0.021	0.25	24	3.33	0.5	57	60	6.4	C	300 and 450	1 and 3

[1] Specimens 2–5 and 7 were tested by Kitajima et al. (2017); test unit SC-W-H was tested by the authors.

[2] Lateral loading: M = monotonic, C = cyclic.

[3] Corresponds to lateral loading location.

[#] Specimens were restrained against rotation at top and bottom, resulting in a shear aspect (moment-to-shear) ratio of 0.5.

Table 2. Results of Experiments by Kitajima et al. (2017)

Specimen	T_{max} (°F)	$V_{n\text{-}ip}$ (kips)	K_{in} (kips/in.)	K_{sec} (kips/in.)	$V_{n\text{-}ip}/V_{n\text{-}ip\text{-}2}$	$K_{in}/K_{in\text{-}2}$	$K_{sec}/K_{sec\text{-}2}$
2	Ambient	790	8800	3630	1.00	1.00	1.00
3	293	561	3650	2330	0.71	0.41	0.64
4	293	699	3120	2330	0.88	0.35	0.64
5	347	600	2790	2090	0.76	0.32	0.58
7	572	609	2510	1870	0.77	0.29	0.52

is attributed primarily to the concrete cracking caused by the thermal loads and the slight reduction in the elastic and shear moduli of steel and concrete materials, as discussed previously. The secant stiffness of the heated specimens was calculated at 60% of the peak load for the control Specimen 2. The secant stiffness of the heated specimens reduced to about 50–60% of the secant stiffness of the ambient Specimen 2. While Specimens 3 and 4 had similar stiffness reductions, the reduction in strength for the monotonically loaded specimen (Specimen 3) was greater than that for the specimen with cyclic loading (Specimen 4), which was an unexpected result.

Most of the specimens tested by Kitajima et al. (2017) were subjected to heating, while maintaining surface temperatures at the target value, for 30 days (except Specimen 5, for which the heating duration was only 60 minutes). Because the specimens were scaled (1:7 scale), the heating duration of 30 days will actually correspond to several months of accident temperature for the physical structure, which is not representative of the accident scenarios. The probability of powerful aftershocks (potentially as intense as the main shock), during or after a thermal accident initiated by a seismic event, is highest during the first few hours after the main seismic event. Therefore, the accident durations should be scaled for the specimens to better simulate the nonlinear thermal gradient history. The duration of heating (30 days) for the scaled specimens tested by Kitajima et al. (2017) would have resulted in uniform temperature through the thickness [based on the discussion in Bhardwaj et al. (2015)], which is not representative of the critical state (with nonlinear thermal gradient) for the wall. Kitajima et al. (2017) also do not provide any information about the reduction in the shear stiffness of these (shear-critical) specimens due to accident thermal temperatures.

To address these concerns, and to supplement the knowledge obtained from the tests by Kitajima et al. (2017), the authors conducted experiments to evaluate the ambient stiffness and the stiffness and strength of SC walls for combined thermal and seismic loading. The experiments were designed to evaluate the effects of different magnitudes and durations of accident temperatures on the stiffness and strength of SC walls. Instrumentation layout was designed to calculate the secant wall stiffness and the component shear and flexural stiffnesses of the SC walls for ambient and accident thermal conditions.

DESIGN OF EXPERIMENTS

This section discusses the design of the test unit, the experimental setup and procedure, and the instrumentation layout for the tests conducted by the authors.

Design of Test Unit

Table 1 presents the details of the SC wall test unit (SC-W-H) subjected to combinations of accident thermal and seismic loading protocols. The faceplate and flange plate slenderness ratios were designed to meet the limits recommended by AISC N690 (2018)—that is, to develop yielding in compression before local buckling, based on Zhang et al. (2014). The test unit had a shear aspect (wall height-to-length) ratio of 0.75, and the flange plate thickness was designed to ensure that the specimen has a shear-critical response similar to squat walls in safety-related nuclear facilities. Three-dimensional nonlinear inelastic finite element models were developed for the specimen tested by Kitajima et al. (2017) and analyzed using ABAQUS (Simulia, 2014). The modeling details are provided in Sener et al. (2019b) and Bhardwaj (2018), and not repeated here for brevity. Figure 1(a) compares the results from the finite element analysis of Specimen 2 with the lateral force-deformation response reported from the test conducted under monotonic loading. The figure also includes horizontal lines corresponding to the in-plane shear strength, V_n^{AISC}, and in-plane flexural capacity, M_{ny}, of the wall. The in-plane shear strength was calculated using Equation A-N9-20 in AISC N690 (2018), and the in-plane flexural capacity was calculated using the plastic stress distribution method in Section NI.2 of AISC N690, both while using measured material properties. As shown in Figure 1(a), the stiffness and strength estimated by the numerical model compared favorably with the experimental results. The benchmarked modeling approach was then used to predict the behavior and finalize the design of the SC wall test unit. The numerical models considered

60 ksi yield strength for both the faceplates and the flange plates. The flange plate thickness of the SC wall test unit was varied to evaluate behavior and to ensure that the test unit with wall aspect ratio of 0.75 was shear critical—that is, have lateral loading corresponding to in-plane flexural strength greater than that corresponding to in-plane shear strength. As shown in Figure 1(b), three different thicknesses for flange plates were used in the models (0.50, 0.75, and 1.00 in.). A comparison of these responses indicated that 0.75 in. flange plate thickness provided sufficient flexural capacity for the test unit to be shear critical and was, therefore, used for SC-W-H.

Loading and Heating Protocols

Table 3 summarizes the loading and heating protocols for the test unit SC-W-H. Similar protocols were employed for SC wall pier and RC wall units tested by the authors (Bhardwaj et al., 2018, 2019a, 2019b). The test unit was subjected to two surface temperature magnitudes (300°F and 450°F), and force/displacement cycles at heating durations of 1 hr and 3 hr. The temperature magnitudes were based on typical containment internal structure (CIS) surface time-temperature histories for postulated pipe break scenarios as obtained from public domain documents (discussed in Sener et al., 2015a). These temperature magnitudes are also consistent with those used by Kitajima et al. (2017). Based on the discussion in Bhardwaj et al. (2015): (1) 1 hr heating duration was selected to develop significant nonlinear thermal gradient (resulting in extensive concrete cracking) through the cross section, and (2) 3 hr heating duration was selected to reduce the nonlinearity of thermal gradients through the cross section (potentially reducing the crack widths). These heating durations (of 1 and 3 hr) result in through thickness temperature profiles in the scaled test unit (1:3 to 1:4 scale) similar to those observed in full-scale (36- to 48-in.-thick) walls. The test unit was cooled down to ambient temperature after completing the load cycle at 3 hr of heating and then heated-loaded to the next temperature-load level.

Figure 2 presents the loading and heating time history for test unit SC-W-H. The loading and heating cycles are plotted together against the duration of testing (for clarity, the time for the test unit to cool down between heating cycles has not been plotted). Loading cycle numbers are also mentioned in the figure. As shown in Table 3 and Figure 2, the first three load cycles were performed at ambient temperature and load levels corresponding to 25, 50, and 75% of the estimated test unit strength, F_n (Cycles 1, 2, and 3, respectively). F_n was the force corresponding to nominal in-plane shear strength (using measured properties) of the test unit, based on AISC N690 (2018). These initial cycles were performed to investigate the ambient response of the wall pre- and post-cracking and before faceplate yielding and to compare the ambient response with responses (obtained in later cycles) for thermal loading. The ambient cycles were followed by heated cycles, where the faceplates and flange plates were heated to a surface temperature of

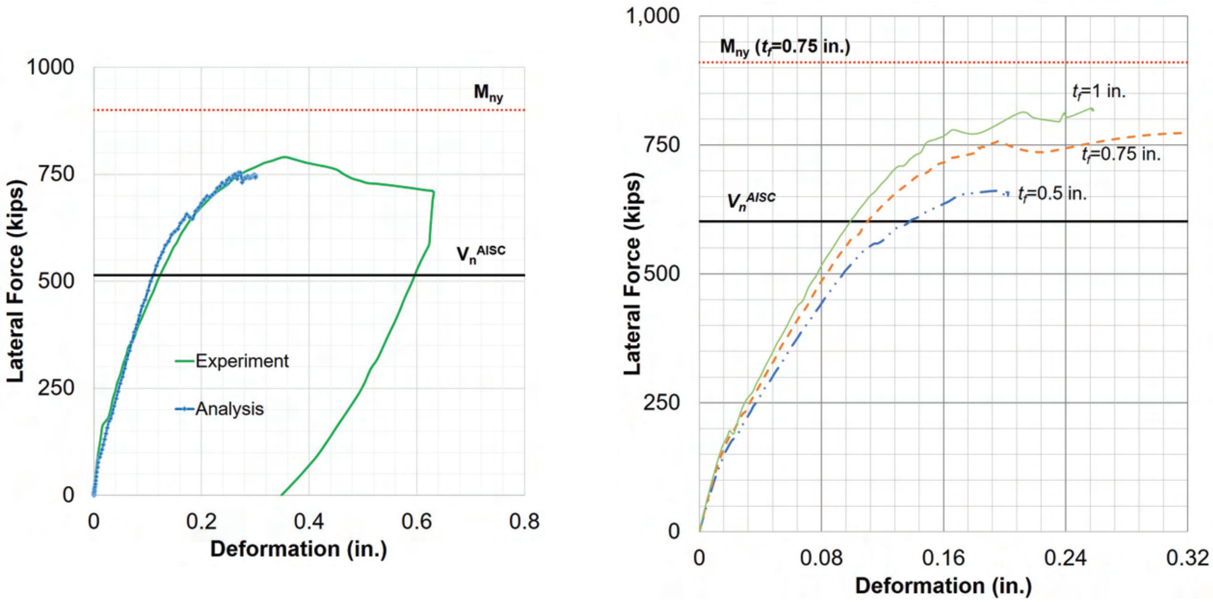

(a) Lateral load-deformation response of Specimen 2 from Kitajima et al. (2017)

(b) Comparison of lateral load-deformation response of proposed SC wall test unit

Fig. 1. Benchmarking analysis for design of SC-W-H test unit.

Table 3. Loading and Heating Protocol for SC-W-H			
Cycle No.	**Surface Temperature (°F)**	**Heating Duration (hours)**	**Target Force/ Displacement Level**
1	Ambient	NA	$0.25F_n$
2	Ambient	NA	$0.5F_n$
3	Ambient	NA	$0.75F_n$
4	300	1	$0.75F_n$
5	300	3	$0.75F_n$
6	450	1	$0.75F_n$
7	450	3	$0.75F_n$
8	450	1	$1.0\Delta_y$
9	450	3	$1.0\Delta_y$
10	Ambient	NA	$1.0\Delta_y$
11	450	1	$1.5\Delta_y$
12	450	3	$1.5\Delta_y$
13	Ambient	NA	$1.5\Delta_y$
14	450	1	$2.0\Delta_y$
15	450	3	$2.0\Delta_y$

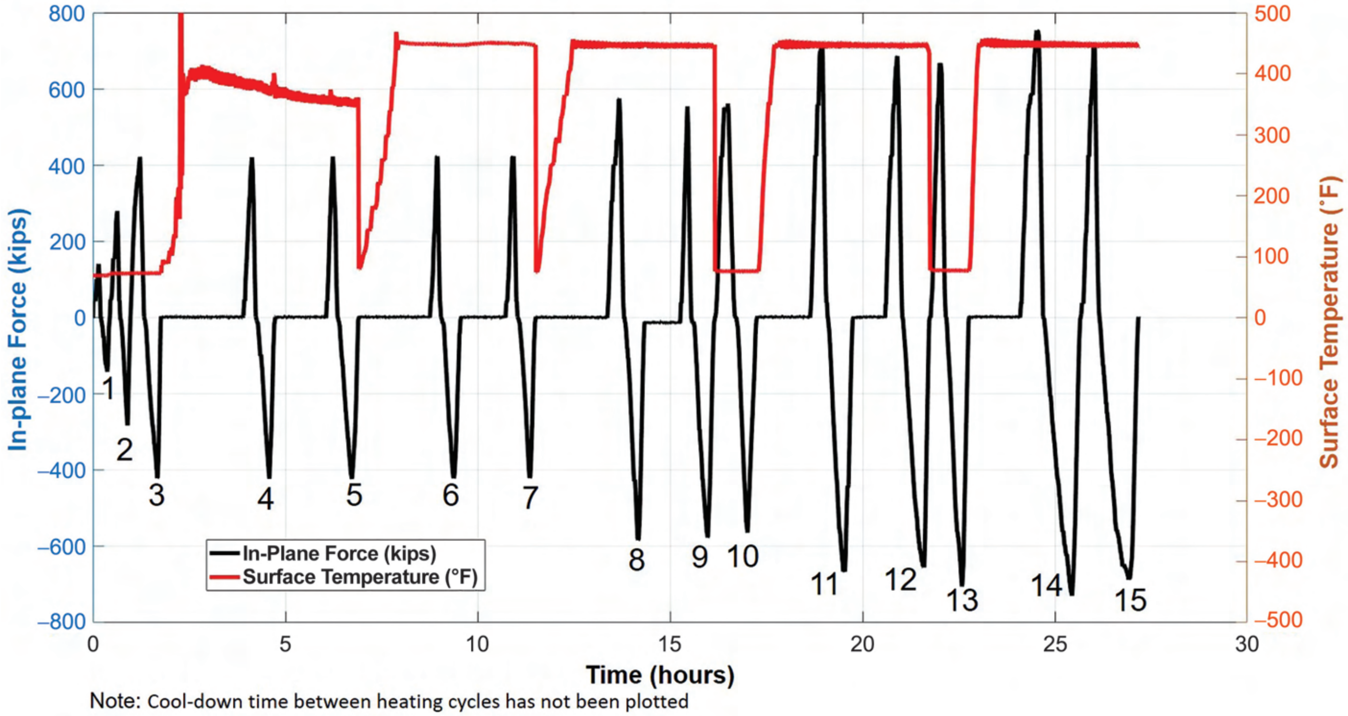

Fig. 2. Load and temperature time history for test unit SC-W-H.

300°F for 1 and 3 hr (Cycles 4 and 5, respectively; some regions of the wall were subjected to surface temperatures between 350 and 400°F). Similar heated cycles were conducted for surface temperature of 450°F (Cycles 6 and 7). The cycles that followed (Cycle 8 onward) were conducted in displacement control. Yield displacement (Δ_y) was estimated as the displacement corresponding to nominal yield load (F_n) of the test unit, based on the average secant stiffness observed in Cycles 6 and 7. The test continued with thermal and displacement cycles at $1.0\Delta_y$ (Cycles 8 and 9) and $1.5\Delta_y$ (Cycles 11 and 12). Additional ambient loading cycles (10 and 13) were performed after the heated cycles at target displacement levels of $1.0\Delta_y$ and $1.5\Delta_y$ to determine if the stiffness increased after cooling. After the $1.5\Delta_y$ cycles, the test unit was subjected to $2.0\Delta_y$ (Cycles 14 and 15) cycles with surface temperatures maintained at 450°F for heating durations of 1 and 3 hr.

Test Setup

Figure 3 shows a photograph of the test unit and setup (without heaters) in Bowen Lab. Lateral loading was applied using two 660-kip-capacity, double-acting, 12 in. stroke hydraulic actuators, which were post-tensioned to the laboratory reaction wall through a clevis-and-pin detail and a built-up wall box. The actuators applied lateral loading through loading beams that were bolted to the test unit. The steel assembly for the test unit (with flange plates, faceplates, studs, and ties) was fabricated, welded to a reusable baseplate foundation, and concrete was poured into the steel assembly. The steel baseplate was 60 in. long, 21.375 in. wide, and 1 in. thick. The baseplate had sixty ⅜-in.-diameter shear studs (in three rows) on the top surface to transfer the forces from concrete infill to the baseplate. The baseplate was anchored to a concrete foundation block using 85 A706 #6 rebar that were 47 in. long. The rebars were attached to the baseplate using Lenton C3J welded couplers.

The foundation block was post-tensioned to the strong floor using sixteen 1¾-in.-diameter DYWIDAG bars, each post-tensioned to 250 kips. The wall-to-basemat connection was designed in accordance with AISC N690 (2018) and following AISC Design Guide 32 (Bhardwaj and Varma, 2017) to be 25% stronger than the wall, and thus limit inelastic deformations, yielding, failure, etc., to the wall portion outside of the wall-to-basemat connection. The wall-to-basemat connection included the steel faceplate-to-baseplate welded connection, the steel flange plate-to-baseplate welded connection, the wall concrete infill-to-baseplate connection achieved using shear stud anchors, and the steel baseplate-to-concrete basemat connection achieved using rebar anchors welded to the baseplate and embedded (fully developed) into the concrete foundation block. Thermal loading was applied to the faceplates and the flange plates (region between the loading beams and baseplate on the foundation block in Figure 3) using ceramic fiber radiant heating panels that were powered and controlled by a custom-built control system described in detail in Bhardwaj (2018).

Instrumentation of Test Unit

Instrumentation layout for the test unit is presented in Figure 4. Displacement sensors [SPs in Figure 4(b)] were used to measure the lateral displacement at the loading location and bottom of the wall. The displacement measurements were used to obtain lateral force-displacement response of the test unit, base slip corrections (and to calculate the flexural deformation of the SC wall). Rotation meters (clinometers) were installed at the base of the wall in the in-plane [CM1 and CM2 in Figure 4(b)] direction. The in-plane

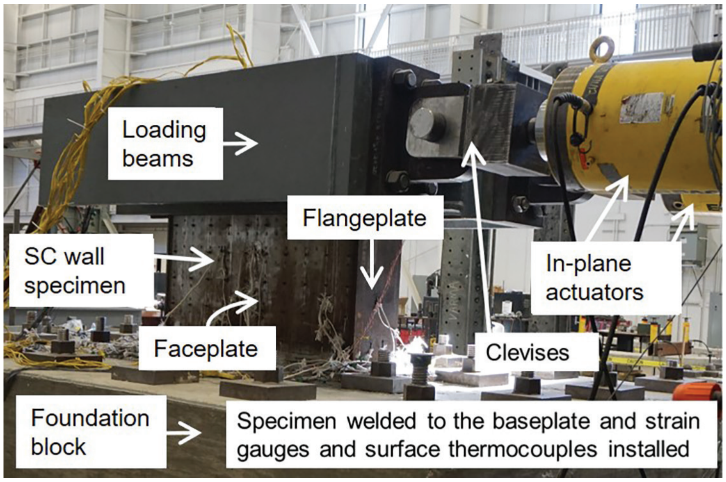

Fig. 3. Test unit and setup (without heaters).

rotation data was used to apply base rotation corrections to in-plane force-displacement plots [to subtract the rigid body displacement (due to base rotations) from the measured displacements]. High-temperature strain gauges were installed on the faceplates to evaluate the behavior of faceplates (flexural or shear stresses, buckling, yielding) for lateral loading. Figure 4(a) presents the strain gauge (S) layout for the exposed surfaces of the faceplates. Similar layout of strain gauges was used for the inside of the faceplate. High-temperature strain gauges were also installed in the bottom region of the inside and outside faces of the flange plates. Type-K thermocouples were used to measure the surface temperatures and temperature through the thickness of the wall. The surface thermocouples [ST as shown in Figure 4(b)] were installed on the steel plates to control the ceramic heaters and to record the surface temperatures. Thermocouple trees [TT and CT in Figure 4(a)] were embedded in the concrete (placed in steel assembly before concrete casting) to measure the temperature through the thickness of the wall. A thermocouple tree consisted of

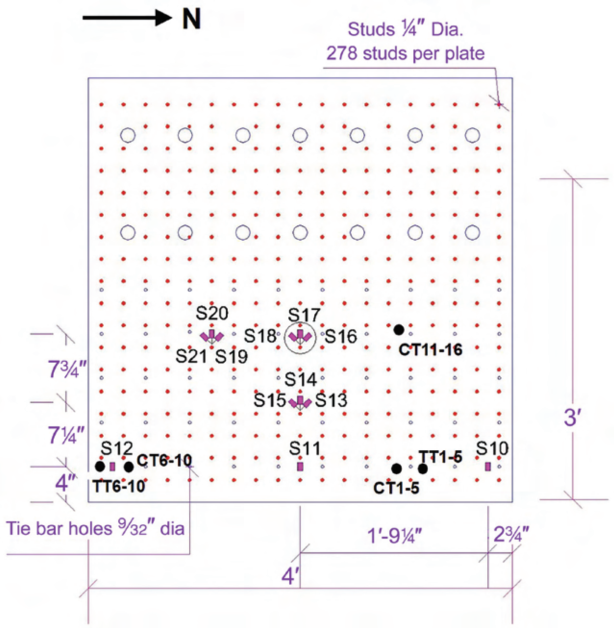

(a) Test unit details, strain gauge, and thermocouple tree layout

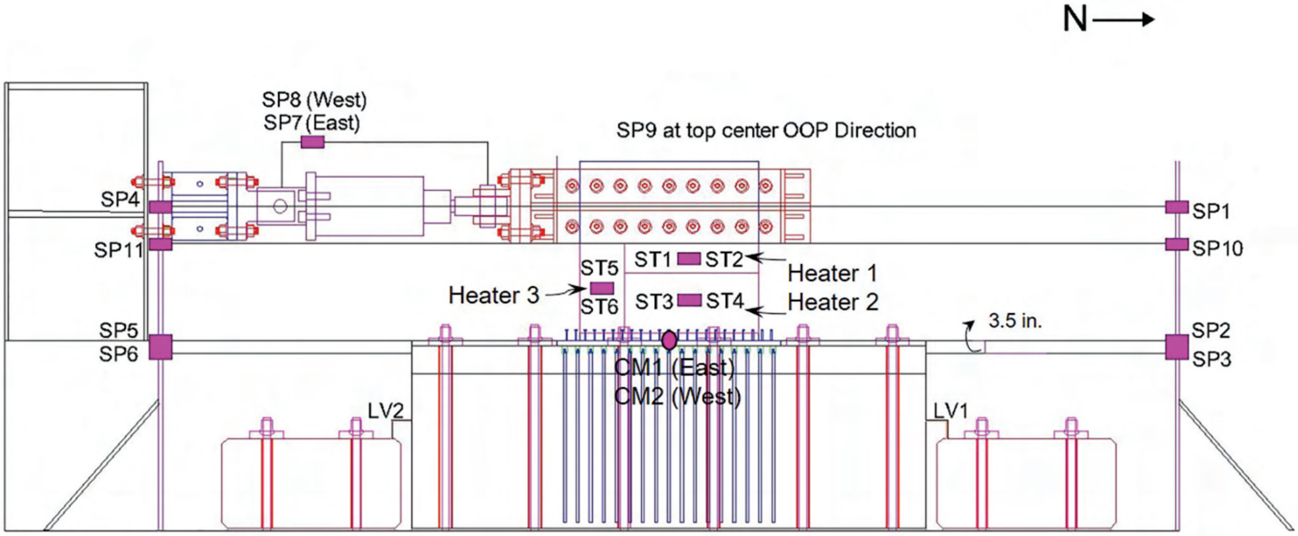

(b) String pots, clinometers, surface heaters, and surface thermocouples

Fig. 4. Sensor layout for test unit SC-W-H.

five thermocouples along the thickness of the wall (at 1, 2, and 5 in. from the surface of the wall). Layout of the heater assembly for the East faceplate is also shown in Figure 4(b) (Heater 1, 2, and 3).

EXPERIMENTAL OBSERVATIONS AND RESULTS

Table 1 reports the material properties measured on the day-of-test for the test unit SC-W-H. The test unit SC-W-H was subjected to loading and heating protocols presented in Table 3, and histories summarized in Figure 2.

Thermal Gradient

Figure 5(a) illustrates the evolution of through-thickness thermal gradient for surface temperature of 450°F [obtained from CT 6-10 in Figure 4(a)]. Even after 3 hr of heating, a nonlinear thermal gradient persisted through the wall thickness, with the wall center at approximately 265°F. The nonlinear thermal gradients and internal restraint resulted in thermally induced concrete cracking in the wall. For the case with surface temperature at 300°F (not included in Figure 5), the nonlinearity in the thermal gradient was lower and was reduced further as the duration of heating increased (after 3 hr of heating, the wall mid-thickness was about 230°F). An equivalent uniform through-thickness temperature of concrete infill can be estimated by assuming the thermal gradient distribution to be parabolic. The equivalent uniform concrete temperatures (for 3 hr heating) were 253°F and 326°F for surface temperatures of 300°F and 450°F, respectively.

Force-Displacement

Figure 5(b) presents the lateral force-top displacement response of SC-W-H. The nominal in-plane shear strength (V_n^{AISC}, using measured properties) of the test unit, based on AISC N690 (2018) provisions is also indicated in the figure. The test unit reached an average peak load of 742 kips (+755 kips/−728 kips). Consistent with observations for heated specimens by Kitajima et al. (2017), the peak load for the test unit was 29% higher than V_n^{AISC}. This confirms that the strength of SC walls subjected to typical accident temperatures can be estimated conservatively using current U.S. code provisions. However, accident thermal loads did reduce the stiffness of the test units. Heated cycles (shown with solid red lines) are less stiff than the corresponding ambient cycles (shown with dotted black lines). In order to look closely at the stiffness reduction due to accident thermal loads, ambient and heated (3 hr duration) $0.75F_n$ cycles are plotted in Figure 5(c). The heated cycles were less stiff than the ambient cycle, and the reduction in stiffness was higher for the cycle with surface temperature of 450°F. As seen in Figure 5(b), the test unit exhibited pinched force-displacement hysteretic response after thermal loading. The hysteretic response for thermal cycles exhibited more extensive pinching than that typically observed at ambient temperatures because thermally induced strains result in the concrete crack widths to be larger. This resulted in a low initial stiffness, but the stiffness increased as compressive stresses (due to lateral loading) gradually closed the thermally induced cracks.

Progression of Damage

Incremental lateral loading resulted in additional concrete flexural and shear cracking, followed by faceplate yielding in tension. Figure 5(d) presents the lateral force-longitudinal strain response of the faceplates for ambient and heated (450°F, 1 hr) cycles at $0.75F_n$ and $1.0\Delta_y$ (cycles 3, 6, and 8 and 10 in Table 3 and Figure 2). Strain gauges S3 and S10 were located at the base of the wall between the first and second row of studs [location of S10 shown in Figure 4(a); S3 was located on the opposite faceplate, corresponding to the location of S12 in Figure 4(a)]. Faceplates started yielding in tension during the ambient $0.75F_n$ cycle, as S3 and S10 strains reached tensile strains of around 2000 με (net tensile strains in S3 and S10 were 1750 and 2300 με, respectively, compared to yield strain of 1980 με). For the $0.75F_n$ heated cycle, the net tensile strains were similar. There was no compression yielding in the faceplates for $0.75F_n$ cycles. For the $1.0\Delta_y$ heated and ambient cycles, the faceplate tensile strains exceeded the yield strain.

Because the test unit was designed to have a shear critical response, the flange plates were not expected to yield until after the Δ_y cycles. Figure 5(e) presents the lateral force-longitudinal strain response of the flange plates for ambient $0.75F_n$, $1.0\Delta_y$ and $1.5\Delta_y$ cycles (cycles 3, 10, and 13 in Table 3 and Figure 2). As the faceplate strains for ambient and heated cycles were similar [Figure 5(d)], only the ambient cycle strains have been plotted in Figure 5(e). Strain gauges S45 (north flange plate) and S47 (south flange plate) were installed between the bottom two rows of studs on flange plates, at 5 in. (125 mm) from the base. The flange plates did not undergo yielding for the cycles shown in the figure (tensile and compressive strains are lower than yield strain, 2070 με). However, a reversal of incremental strains was observed during the $1.5\Delta_y$ cycle [encircled in Figure 5(e)]. Since the flange plate studs were detailed to ensure that the slenderness criteria of AISC N690 (2018) was satisfied, the flange plates were not expected to undergo buckling before compression yielding. However, as the lateral loading increased and the faceplates underwent von Mises yielding, the magnitude of concrete compression strut force anchored at the toe of the wall-to-basemat connection (i.e., at the flange plate-faceplate-baseplate joint) increased. This compression strut, in combination with the vertical compressive

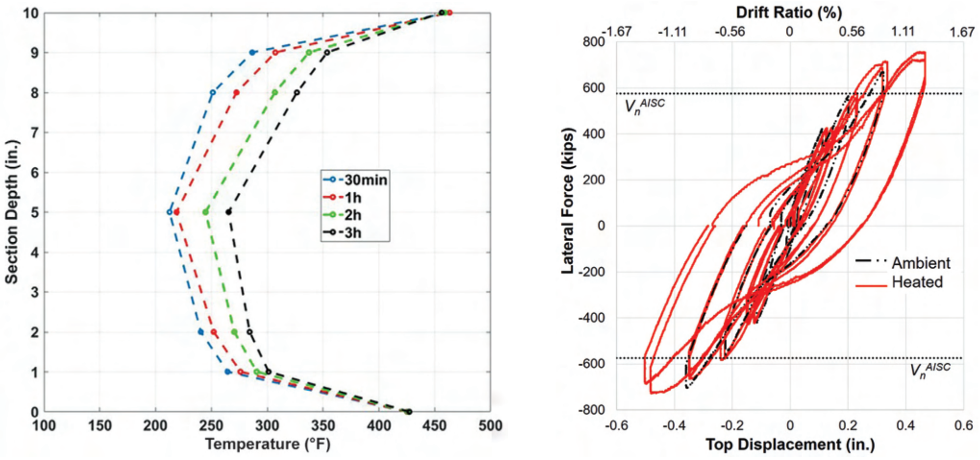

(a) Thermal gradient (surface at 232°C) *(b) Lateral force-top displacement* (F–Δ)

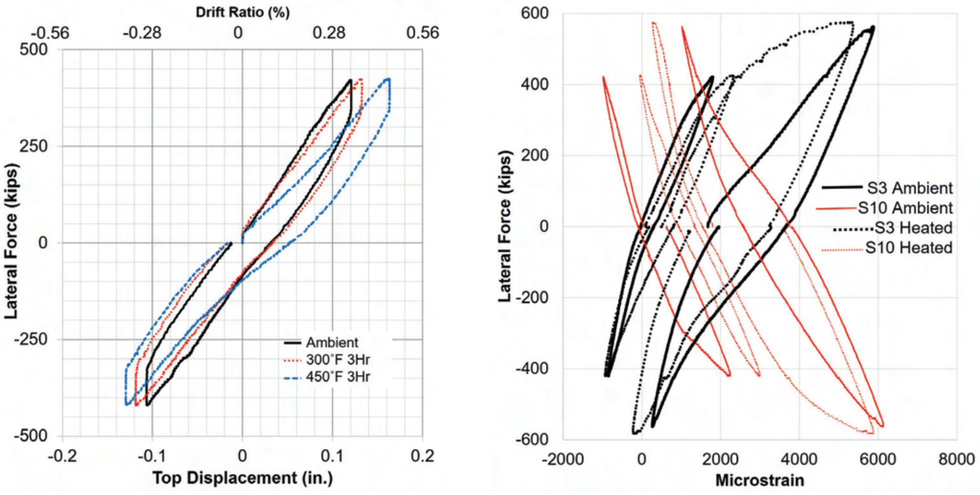

*(c) Lateral force-top displacement (for 0.75*F_n *cycles)*

(d) Faceplate F–ε *for ambient and heated 0.75*F_n *and* Δ_y *cycles*

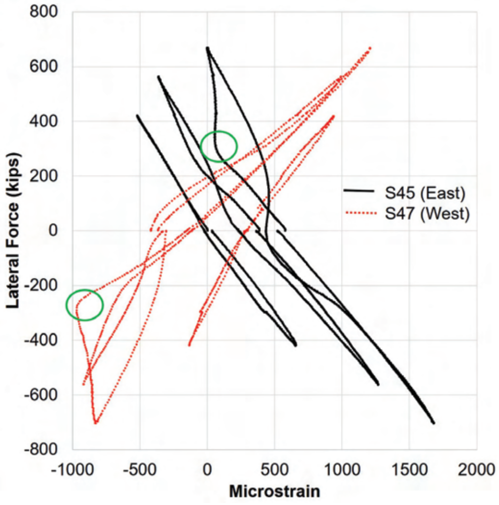

(e) Flange plate F–ε *for ambient 0.75*F_n, Δ_y *and 1.5*Δ_y *cycles*

Fig. 5. Experimental results for SC-W-H.

force in flange plate (from the overturning moment induced by the lateral load), forced the flange plate (and faceplates near the corners) to bulge out between the bottom two rows of studs. This flange plate bulging resulted in the reversal of strains on the exterior face of flange plates [as observed in Figure 5(e)].

The concrete compression strut also caused additional stresses in the weld between the faceplate-flange plate-baseplate. These additional stresses at the weld location, compounded by the weld detail being highly constrained (due to discontinuities), resulted in the initiation of weld fracture at the corner joint during the second $2\Delta_y$ cycle (cycle 13). The weld fracture is shown inset (top right) in Figure 6(a). The fracture progressed upward into the faceplate-flange plate weld and downwards into the flange plate-baseplate weld [shown in bottom right inset in Figure 6(a)]. This fracture resulted in faceplate and flange plate rupture and failure of the test unit in the next cycle. Steel rupture of the test unit is shown in Figure 6(a) (zoomed in to bottom of the test unit). The weld fracture [shown in top right inset in Figure 6(a)] propagated to fracture the flange plate and then the faceplates. The bulging of the faceplates due to the concrete compression strut (as discussed previously) is also visible in Figure 6(a).

After the failure of the test unit, one of the faceplates was removed to inspect the state of the concrete infill. Figure 6(b) shows the concrete cracking and damage in the test unit at failure. Concrete infill cracked predominantly in shear (the cracking angle varied between 35 and 45°). Rupture of the faceplates and flange plate at the base during the failure cycle resulted in the concrete infill being subjected to large rotation about the compression toe. This rotation caused large residual tensile strains and crack opening in the concrete, which is visible in Figure 6(b). Since the test unit failed due to plate rupture, there was no concrete compression crushing or faceplate shear buckling in the test unit.

Stiffness Degradation

The lateral force-top displacement response of the test unit [Figures 5(b) and (c)] indicated a reduction in wall stiffness due to thermal loading. Because the test unit was shear controlled, the effect of thermal loads on the shear stiffness on the test unit is of particular interest. This shear stiffness of the test unit can be compared with stiffness provisions for analysis provided in AISC N690 (2018). Per AISC N690, shear stiffness of the SC wall depends on the magnitude of lateral loading. For lateral loads lower than a cracking threshold, S_{cr}^{AISC}, uncracked shear stiffness, GA_{uncr}^{AISC}, is considered. For lateral loads greater than $2S_{cr}^{AISC}$, the stiffness is considered to reduce to cracked secant stiffness, GA_{cr}^{AISC}, considering orthotropic cracked concrete and plane stress steel plate behavior. For lateral loads between S_{cr}^{AISC} and $2S_{cr}^{AISC}$, the stiffness can be linearly interpolated between uncracked and cracked stiffnesses. For thermal load combinations, the shear stiffness is considered to be cracked, GA_{cr}^{AISC}.

Figure 7(a) presents the lateral force-shear strain response of the test unit (for $0.25F_n$ and $0.5F_n$ ambient cycles), where the slope of the response is the experimentally observed shear stiffness. Shear strain for the test unit was calculated from strain gauge rosettes (S4-6, S7-9, S13-15, S16-18). The location of strain gauges S13-18 is shown in Figure 4(a). S4-9 were located on the other faceplate at locations corresponding to S13-18 in Figure 4(a). The strain values from rosettes were used to obtain principal strains and direction. Shear strain, γ_{xy}, was calculated using the principal strains and direction. Average shear strain for the four strain gauge rosettes was plotted in Figure 7(a). The figure includes lines corresponding to the secant shear stiffness estimated using AISC provisions—namely, GA_{uncr}^{AISC}, GA_{cr}^{AISC}, and a line corresponding to GA_{cr}^{TAN}, which is the tangent cracked shear stiffness for SC walls estimated using equations in Seo et al. (2016), also discussed in the AISC N690 commentary.

It is observed that the uncracked stiffness, GA_{uncr}^{AISC}, was not manifest in the test unit (even at ambient conditions). This may be due to shrinkage-related cracking and concrete cracking at low magnitude of lateral loads. The test unit developed shear cracks at force level approximately equal to S_{cr}^{AISC}, and the stiffness reduced further thereafter. Shear stiffness for the $0.25F_n$ cycle was approximately equal to the cracked secant stiffness, GA_{cr}^{AISC}. For the $0.5F_n$ cycle, the stiffness dropped below GA_{cr}^{AISC}. However, the shear stiffnesses for both the cycles were higher than the tangent cracked stiffness, GA_{cr}^{TAN}. This suggests that the lower-bound shear stiffness of the test unit can be estimated as GA_{cr}^{TAN}. AISC recommended secant stiffness, GA_{cr}^{AISC}, was higher than experimentally observed secant stiffness. This may be because the uncracked stiffness was not manifest (or the test unit cracked at low magnitude of lateral force).

Figure 7(b) presents the degradation of the experimentally measured shear stiffness of the test unit, where the measured shear stiffness is normalized with the cracked tangent stiffness, GA_{cr}^{TAN}. The experimental shear stiffness was estimated using data from the strain gauge rosettes [as discussed for Figure 7(a)]. The shear stiffness of the test unit was also estimated using lateral displacement measurements in order to cross-check the values estimated using strain gauge rosettes and to obtain stiffness values for cycles where strain gauges were damaged due to heating. The corrected top displacement values (corrected for rigid body displacements associated with base slip and rotation) consist of both shear and flexural deflections. The flexural deflection was estimated using EI_{cr} (cracked flexural stiffness). For calculation of EI_{cr}, the neutral axis location was considered to be at one-third of the length of the test unit (consistent with observations based on strain gauge data and the cross-section moment curvature relationship). For heated cycles, the flexural stiffness is considered to linearly reduce from EI_{cr} to EI_{steel} for surface temperature increase, ΔT, from 0°F to 270°F (based on the observations and recommendations discussed later). The shear deflection was then calculated by subtracting the flexural deflection from the total deflection, and the shear strain was estimated as the shear deflection divided by the test unit loading height. The shear stiffnesses estimated using the strain gauge data, and lateral displacement data are compared in Figure 7(b).

For the pre-yield $0.5F_n$ and $0.75F_n$ ambient cycles, the shear stiffness estimated using the lateral displacement data is slightly higher than the stiffness estimated using strain gauge data, but the trends are similar. For the $0.75F_n$, 300°F cycles, some of the strain gauge rosettes were damaged due to heating, and the average shear strain consists of only the functioning rosettes. For the $1.0\Delta_y$ cycles, stiffnesses estimated using displacement data are slightly higher because the test unit was undergoing shear yielding, which was not considered in displacement data stiffness calculations. Based on the comparisons in Figure 7(b), the stiffnesses estimated using lateral displacement data can be considered cautiously in the absence of complete or adequate strain gage data.

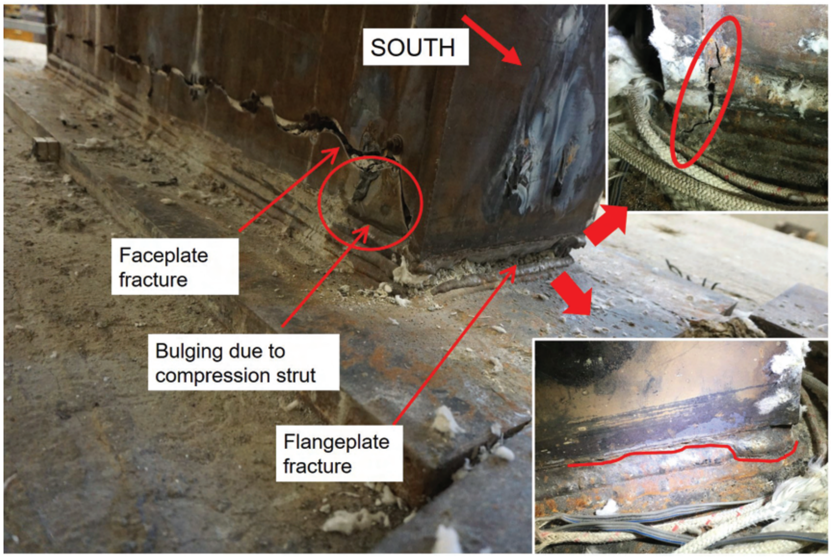

(a) Steel failure

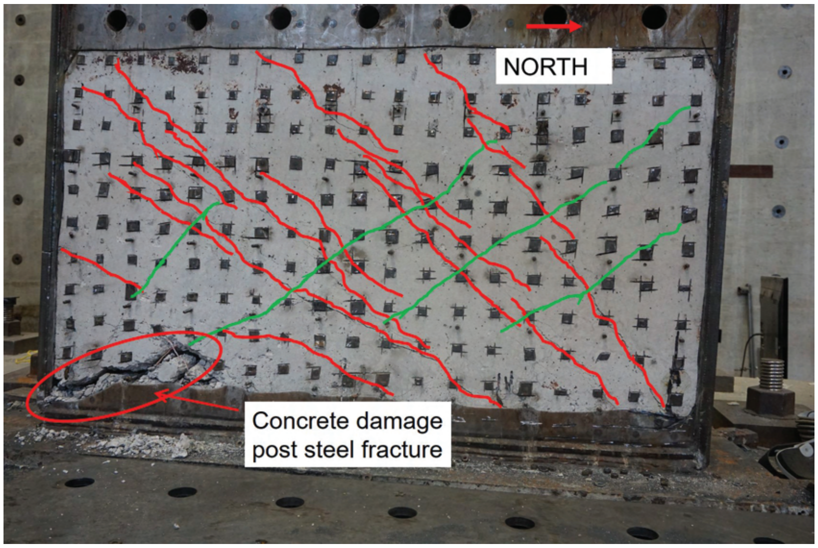

(b) Concrete cracking

Fig. 6. Test unit SC-W-H at failure.

As observed in Figures 7(a) and 7(b), the shear stiffness for the $0.25F_n$ and $0.5F_n$ ambient cycles was higher than the cracked tangent shear stiffness, GA_{cr}^{TAN}. The ambient shear stiffness corresponding to $0.75F_n$ was approximately equal to GA_{cr}^{TAN}. However, the normalized stiffness for $0.75F_n$ cycles dropped considerably as thermal loading was applied. The normalized stiffness reduction was 21% for 300°F and 38% for 450°F in comparison to the ambient stiffness. As mentioned earlier, the reduction in normalized stiffness can be attributed to (1) the temperature-dependent reduction in elastic and shear moduli of steel and concrete materials and (2) concrete cracking effects. Calculations indicate that the stiffness reduction due to item 1 is 16% for 300°F and 26% for 450°F. The remaining reduction is due to item 2, which is concrete cracking induced by thermal strains, nonlinear gradient, and internal restraint. These experimental results, observations, and discussion indicate that the reduction in shear stiffness due to items 1 and 2 needs to be considered for seismic and thermal loading combinations. Figure 7(b) also includes a horizontal line corresponding to the ambient shear stiffness of the steel alone, GA_{steel}, while ignoring the contribution of the concrete infill due to extensive cracking. Based on Figure 7(b), the shear stiffness can be considered to reduce linearly from GA_{cr}^{TAN} to GA_{steel} for a surface temperature increase, ΔT, from 0°F to 270°F. This would provide a lower-bound estimate of the shear stiffness and also eliminate the need for using temperature-dependent properties for typical accident temperatures.

The overall stiffness response of the SC wall is a combination of its flexural and shear stiffnesses. The stiffness degradation of the SC-W-H test unit was evaluated by considering the reduction of the normalized stiffness, K_{sec}/K_{cr}, with loading and heating cycles. The secant stiffness, K_{sec}, was calculated as the average of push (+) and pull (–) stiffnesses. The push and pull stiffnesses were calculated from the peak force and corresponding displacement values (corrected for base slip and base rotation) for a cycle. The cracked stiffness, K_{cr}, was calculated using the cracked flexural and shear stiffness—namely, EI_{cr} and GA_{cr}^{TAN}. EI_{cr} was calculated considering the neutral axis at one-third of the test unit length (as discussed previously). Figure 7(c) presents the degradation of the normalized secant stiffness, K_{sec}/K_{cr}, of the test unit with loading and heating cycles. As observed previously in Figure 7(a), the uncracked stiffness did not manifest in the wall (even for the initial cycles). The secant stiffness, K_{sec}, of the wall for $0.25F_n$ cycles was 1.9 times K_{cr} (which is also 0.52 times the uncracked stiffness). The secant stiffness reduced for higher lateral loads as the concrete developed shear and flexural cracks. The secant stiffness corresponding to $0.75F_n$ ambient cycles was approximately equal to $0.9K_{cr}$.

As shown in Figure 7(c), accident thermal loading reduced the normalized stiffness significantly. The secant stiffness reduced to $0.70K_{cr}$ for the $0.75F_n$, 300°F cycles and to $0.58K_{cr}$ for the $0.75F_n$, 450°F cycles. The duration of heating (1 hr or 3 hr) did not seem to have a significant influence on the normalized stiffness because concrete cracking occurs early upon the introduction of heating due to the nonlinear thermal gradient and internal restraints. While the additional heating duration reduces the nonlinearity of the thermal gradient, it does not result in an increase in the stiffness. To evaluate any change in stiffness upon cooling down of specimens, ambient cycles were performed after the heated cycles (i.e., the test unit was allowed to cool down) for the $1.0\Delta_y$ and $1.5\Delta_y$ displacement levels. The normalized ambient stiffness for the $1.0\Delta_y$ cycle is 20% higher than normalized heated stiffness. Similarly, for the $1.5\Delta_y$ cycle, the ambient stiffness is marginally higher than heated stiffness.

EVALUATION OF SC WALL BEHAVIOR AND RECOMMENDATIONS

Thermal Gradient

The specimens tested by Kitajima et al. (2017) were subjected to surface temperatures ranging from 293°F to 572°F for heating duration of 30 days (Specimen 4 was heated for 60 min). The specimens (except Specimen 4) were expected to develop uniform temperature distribution through the thickness [based on Bhardwaj et al. (2015)]. No information was provided regarding the through thickness thermal gradients. The unit tested by the authors was subjected to two surface temperature magnitudes (300°F and 450°F) and two heating durations (1 hr and 3 hr). A nonlinear thermal gradient developed through the wall thickness due to the thermal loads. The extent of nonlinearity reduced as the duration of heating increased. The thermal gradient was higher for surface temperature of 450°F. The mid-thickness of the test unit was at 265°F corresponding to a surface temperature of 450°F and heating duration of 3 hr. The nonlinear thermal gradient resulted in concrete-cracking due to self-restraint and external restraints, which reduced the stiffness of the test unit.

Strength and Stiffness

Table 4 presents the summary of experimental results discussed in the paper. The table presents the maximum surface temperature, T_{max}, maximum increase in surface temperature (ΔT_{max}, considering ambient temperature of 68°F), measured lateral strength, $V_{n\text{-}ip}$, and the ratios of measured strength with nominal strength per AISC N690 (V_n^{AISC}, using measured properties) and the ultimate shear strength (V_u) per Booth et al. (2020). The strength of the heated specimens tested by Kitajima et al. (2017) was higher than the nominal in-plane shear strength (using measured properties) per AISC N690 (2018), with a safety margin ranging from 9% to 36%. The experiments indicated that the strength of SC wall specimens reduced by 15 to 30% for accident thermal loads in comparison to strength of the ambient specimen. Additionally, the strengths of the heated specimens were up to 15% lower than the calculated ultimate shear strength at ambient conditions per Booth et al. (2020). The measured peak strength for the test unit SC-W-H was 29% higher than V_n^{AISC} (about 25% lower than the ultimate shear strength). Based on the experimental results, the strength of specimens subjected to typical accident thermal temperatures and durations can be conservatively estimated using existing strength equations (per U.S. codes, based on von Mises yielding of steel plates) for ambient conditions.

Table 4 also presents the normalized initial, K_{in}, and secant stiffnesses, K_{sec}, and the corrected failure drift ratio for the specimens and the test unit. Initial stiffness of the specimens is normalized with theoretical uncracked stiffness, K_{uncr}, for the specimens. K_{uncr} is calculated considering

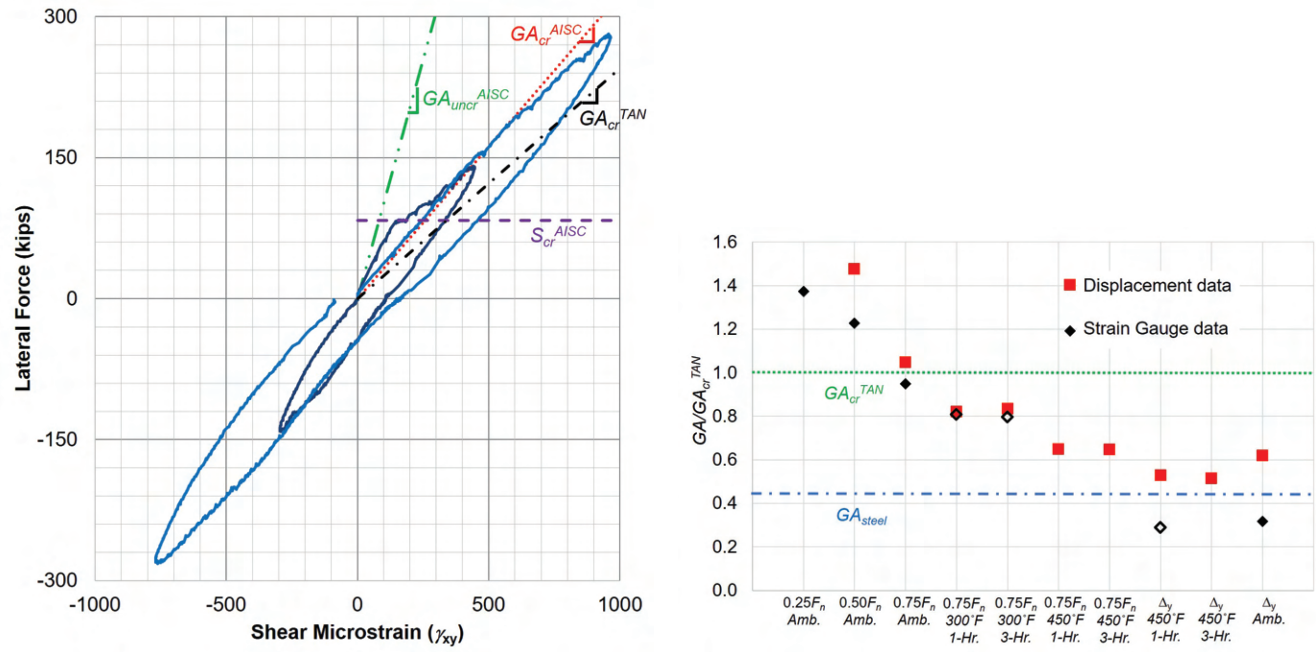

(a) *Shear stiffness: 0.25*F$_n$ *and 0.5*F$_n$ *cycles*

(b) *Shear stiffness degradation*

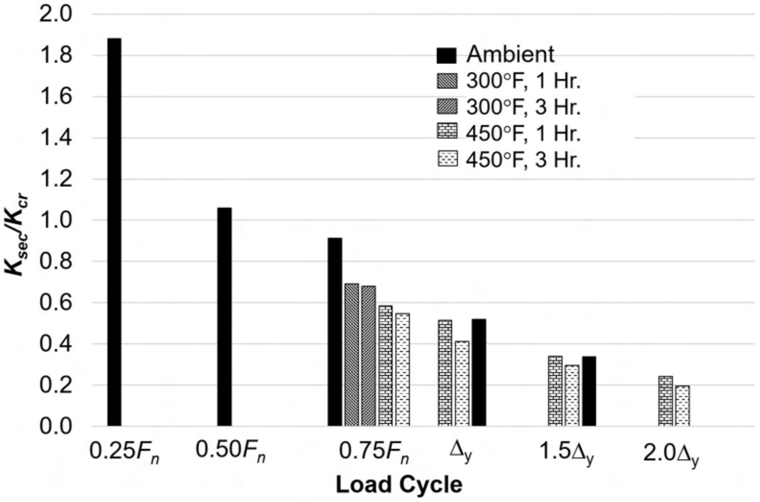

(c) *Secant stiffness degradation*

Fig. 7. Shear and wall secant stiffness for SC-W-H.

Table 4. Summary of Experimental Results

Identifier[1]	T_{max} (°F)	ΔT_{max} (Δ°F)	$V_{n\text{-}ip}$ (kips)	$V_{n\text{-}ip}/V_n^{AISC}$	$V_{n\text{-}ip}/V_u$	K_{in}/K_{uncr}	K_{sec}/K_{cr}	Drift Ratio Failure (%)	K_{sec}/K_{eff}
2	Ambient	NA	790	1.54	1.08	0.67	0.95	2.3	0.95
3	293	225	561	1.09	0.84	0.29	0.62	4.3	1.02
4	293	225	699	1.36	0.94	0.23	0.61	4.6	1.01
5	347	279	600	1.17	0.87	0.22	0.55	4.0[2]	1.11
7	572	504	609	1.18	0.95	0.20	0.50	4.0[2]	1.04
SC-W-H	Ambient	NA	742[3]	1.29	0.72	0.52	0.91	1.17[3]	0.91
	300	232				—	0.68		1.13
	450	382				—	0.55		1.10

[1] Specimens 2–5 and 7 were tested by Kitajima et al. (2017); test unit SC-W-H was tested by the authors.

[2] The force-displacement response beyond this drift not presented in Kitajima et al. (2017).

[3] Specimen failure initiated by weld fracture.

uncracked shear and flexural stiffnesses of the specimens. Experimental results indicate that uncracked stiffness was not manifest in the specimens (even at ambient conditions). This may be due to shrinkage-induced cracking in the concrete and the concrete cracking in the test unit at low magnitude of lateral loads. The stiffness of the ambient specimens reduced further as the magnitude of shear force applied exceeded the cracking threshold.

Heated specimens by Kitajima et al. (2017) indicated a reduction of 60 to 70% in initial stiffness due to accident thermal loading. Secant stiffness of the specimens is normalized with theoretical cracked stiffness, K_{cr}, of the specimens (without considering temperature dependent properties). Calculation of K_{cr} was discussed previously (it can also be calculated by cross-section moment-curvature analysis). Since the specimens tested by Kitajima et al. were similar to the test unit SC-W-H, the neutral axis location for those specimens is also considered at one-third of the specimen length (confirmed with cross-section moment-curvature analysis). Ambient secant stiffness of SC wall specimens can be reasonably estimated as K_{cr}. Accident thermal loads significantly reduce the stiffness of the specimens. The extent of reduction in stiffness depends on the temperature magnitude of thermal accident. Heated specimens tested by Kitajima et al. experienced a secant stiffness reduction of up to 50% in comparison to secant stiffness for ambient specimen. Heated secant stiffness (and shear stiffness) for test unit SC-W-H reduced by about 25% for 300°F and 40% for 450°F, in comparison to ambient secant (and shear) stiffness. Kitajima et al. specimens failed at drift ratios ranging from 2.3 to 4.6% with significant post-peak ductility. SC-W-H failed due to weld fracture, but still reached a drift ratio of 1.17%.

Based on the experimental results, the secant stiffness (flexure and shear stiffness) for shear-controlled SC walls can be considered to linearly reduce from cracked stiffness to steel-only stiffness for surface temperature change, ΔT, from 0°F to 270°F. The effective in-plane flexural and shear stiffnesses for SC walls can be calculated as shown in Equations 1 and 2, respectively (all values in U.S. units). While the equations are consistent with those proposed for SC wall piers (Bhardwaj et al., 2019a), the calculation of individual terms is different for SC walls and SC wall piers.

$$EI_{eff} = EI_{cr} - \frac{(EI_{cr} - E_s I_s)}{270} \Delta T \geq E_s I_s \tag{1}$$

$$GA_{eff} = GA_{cr}^{TAN} - \frac{(GA_{cr}^{TAN} - G_s A_s)}{270} \Delta T \geq G_s A_s \tag{2}$$

Table 4 also presents the comparison of secant stiffnesses for the specimens normalized with recommended effective stiffnesses, K_{sec}/K_{eff}. K_{eff} is calculated considering EI_{eff} and GA_{eff} as recommended in Equations 1 and 2. The secant (ambient and heated) stiffnesses of the specimens can be reasonably estimated using the recommendations. Because the recommended stiffness reductions provide lower-bound estimates of stiffness, they eliminate the need to consider temperature-dependent properties (for typical accident temperatures up to 572°F). The stiffness recommendations are based on the experiments discussed in this paper. Further experimental or numerical research is needed to validate the recommendations for range of parameters not considered in this paper. The recommended stiffness values can be used to conduct analyses for seismic and accident thermal loading combination per AISC N690 (2018) and as illustrated in Bhardwaj and Varma (2017).

CONCLUSIONS

Steel-plate composite walls in labyrinthine safety-related nuclear facilities need to be designed for combination of accident thermal scenarios with design basis shaking. This paper describes the experimental results for SC walls subjected to combination of accident thermal temperature and seismic loads. The results of SC wall specimens tested by Japanese researchers and the unit tested by the authors were presented in this paper. The following conclusions can be drawn from the experiments:

Based on the data available in design control documents, typical accident temperatures for nuclear facilities may range from 300°F to 570°F, with the temperatures maintained for up to a few days after the accident. The thermal accidents result in the evolution of nonlinear thermal gradients through the cross section. The thermal gradients are highly nonlinear for the first few hours after the accident, and the extent of nonlinearity reduces as the concrete temperature increases with time.

The nominal in-plane shear strength of SC walls at ambient temperatures can be conservatively estimated using the provisions of AISC N690 (2018), which correspond to the limit state of von Mises yielding of the steel faceplates. The ultimate in-plane shear strength of SC walls at ambient temperatures may be calculated using equations by Booth et al. (2020). The in-plane shear strength of specimens subjected to typical accident thermal temperatures (up to 570°F) and durations should be limited to that calculated using the current AISC N690 strength equations for ambient temperatures (based on von Mises yielding of the steel plates); that is, the Booth et al. (2020) equations cannot be used for calculating in-plane shear strength at accident thermal temperatures.

Ambient secant stiffness of SC walls can be reasonably estimated considering cracked flexural, EI_{cr}, and shear stiffnesses, GA_{cr}. EI_{cr} can be calculated from the moment-curvature relationship, and GA_{cr} can be estimated as the tangent shear stiffness, GA_{cr}^{TAN}, based on composite plate theory (Seo et al., 2016). The stiffness of SC walls may be significantly reduced depending on the magnitude of surface temperature and the duration of the accident. The SC unit tested by the authors exhibited reduction in secant stiffness (and shear stiffness) of 25% for surface temperature of 300°F and 40% for surface temperature of 450°F in comparison to the ambient secant stiffness.

The specimens tested by Kitajima et al. (2017) exhibited stiffness reductions of up to 50% of the ambient secant stiffnesses. The reduction in stiffness is due to concrete cracking and reduced elastic and shear moduli of the steel and concrete at elevated temperatures. Concrete cracking also leads to higher stress in steel plates, which may cause the steel plates to yield at lower loads. The stiffness reduction due to accident thermal loads can be considered in analysis by using effective flexure and shear stiffnesses. The effective stiffnesses can be assumed to linearly reduce from cracked stiffness to steel-only stiffness for surface temperature change, ΔT, from 0°F to 270°F. The effective stiffness recommendations are based on the experimental studies discussed in this paper. Additional experimental or numerical research is recommended to further verify and improve the applicability of these recommendations for range of parameters not considered in this paper. For example, this article does not consider the effect of one-sided heating on the strength and stiffness of SC walls. Additional studies are needed to evaluate these effects.

DATA AVAILABILITY STATEMENT

The data for the unit tested by the authors (SC-W-H) are available from the corresponding author by request. The data for the tests conducted by the Japanese researchers, which are used in this paper, are obtained from their publications (Hirama et al., 2015; Kitajima et al., 2017).

ACKNOWLEDGMENTS

The research presented in this article was funded through the FY 2014 Nuclear Energy Enabling Technologies Research & Development and Infrastructure Awards by the U.S. Department of Energy, grant number DOE-ID-14-032. The authors thank Mr. Tom Bradt for his assistance in conducting the tests at Bowen Laboratory.

REFERENCES

ACI (2013), *Code Requirements for Nuclear Safety-Related Concrete Structures and Commentary*, ACI 349, American Concrete Institute, Farmington Hills, Mich.

AISC (2016), *Seismic Provisions for Structural Steel Buildings*, ANSI/AISC 341-16, American Institute of Steel Construction, Chicago, Ill.

AISC (2018), *Specification for Safety-Related Steel Structures for Nuclear Facilities*, ANSI/AISC N690-18, American Institute of Steel Construction, Chicago, Ill.

Alzeni, Y. and Bruneau, M. (2014), "Cyclic Inelastic Behavior of Concrete Filled Sandwich Panel Walls Subjected to In-Plane Flexure," *Technical Report MCEER-14-0009*, MCEER, University at Buffalo, Buffalo, N.Y.

Anwar, H.S., Bhardwaj, S.R., and Varma, A.H. (2019), "On the Response of Squat Reinforced Concrete Walls for Combined Lateral and Accident Thermal Loading," *Proceedings of SMiRT25*, IASMiRT, Charlotte, N.C. https://www.lib.ncsu.edu/resolver/1840.20/37803

ASCE (2022), *Minimum Design Loads for Buildings and Other Structures*, ASCE 7-22, American Society of Civil Engineers, Reston, Va.

Bhardwaj, S.R. (2018), "Multi-Hazard In-Plane Response of Steel-Plate Composite Walls: Out-of-Plane and Accident Thermal Loadings," *Open Access Dissertations*, 1689, Purdue University, West Lafayette, Ind. https://docs.lib.purdue.edu/open_access_dissertations/1689

Bhardwaj, S.R., Sener, K.C., and Varma, A.H. (2018), "Experimental Evaluation of Structural Walls for Seismic and Thermal Forces," in *Proceedings of 11th U.S. National Conference on Earthquake Engineering*, Los Angeles, Calif.

Bhardwaj, S.R., Sener, K.C., and Varma, A.H. (2019a), "Multi-Hazard Investigation and Testing of Steel-Plate Composite (SC) Wall Piers: Seismic and Thermal Loads," *Nuclear Engineering and Design*, Vol. 348, pp. 121–130, Elsevier. DOI: 10.1016/j.nucengdes.2019.03.026

Bhardwaj, S.R. and Varma, A.H. (2017), *Design of Modular Steel-Plate Composite Walls for Safety-Related Nuclear Facilities*, Design Guide 32. American Institute of Steel Construction, Chicago, Ill. https://www.aisc.org/Design-Guide-32-Modular-Steel-Plate-Composite-Walls-for-Safety-Related-Nuclear-Facilities

Bhardwaj, S.R., Varma, A.H., and Orbovic, N. (2019b), "Behavior of Steel-Plate Composite Wall Piers under Biaxial Loading," *Journal of Structural Engineering*, ASCE, Vol. 145, No. 2. https://doi.org/10.1061/(ASCE)ST.1943-541X.0002247

Bhardwaj, S.R., Varma, A.H., and Sener, K.C. (2015), "On the Calculation of Design Demands for Accident Thermal Loading Combination," Transactions of SMiRT 23 in Manchester, UK, Paper ID 850, *IASMIRT*, North Carolina State University, Raleigh, N.C., pp. 1–10. http://www.lib.ncsu.edu/resolver/1840.20/34279

Booth, P.N., Bhardwaj, S.R., Tseng, T., Seo, J., and Varma, A.H., (2020), "Ultimate Shear Strength of Steel-Plate Composite (SC) Walls with Boundary Element," *Journal of Constructional Steel Research*, Vol. 165, Elsevier Science. https://doi.org/10.1016/j.jcsr.2019.105810

Booth, P.N., Varma, A.H., Sener, K., and Malushte, S. (2015), "Flexural Behavior and Design of Steel-Plate Composite (SC) Walls for Accident Thermal Loading," *Nuclear Engineering and Design*, Vol. 295, pp. 817–828, Elsevier Science. http://dx.doi.org/10.1016/j.nucengdes.2015.07.036

Bruhl, J. and Varma, A.H. (2018), "Experimental Evaluation of Steel-Plate Composite Walls Subject to Blast Loads," *Journal of Structural Engineering*, ASCE, Vol. 144, No. 9. DOI: 10.1061/(ASCE)ST.1943-541X.0002163

Bruhl, J., Varma, A.H., and Johnson, W.H. (2015), "Missile Impact Behavior and Design of Composite SC Walls," *International Journal of Impact Engineering*, Vol. 75, pp. 75–87, Elsevier Science. http://dx.doi.org/10.1016/j.ijimpeng.2014.07.015

Bruneau, M., Alzeni, Y., and Fouché, P. (2013), "Seismic Behavior of Concrete-Filled Steel Sandwich Walls and Concrete-Filled Steel Tube Columns," *Steel Innovations 2013 Conference*, Christchurch, New Zealand.

CEN (2004), *Eurocode 2: Design of Concrete Structures—Part 1–2: General Rules—Structural Fire Design*, Comite Européen de Normalisation, EN-1992-1-2, Brussels, Belgium.

CEN (2005), *Eurocode 3: Design of Steel Structures—Part 1–2: General Rules—Structural Fire Design*, Comite Européen de Normalisation, EN-1993-1-2, Brussels, Belgium.

Hirama, T., Kumagai, H., Tanabe, M., Saigou, S., Sawada, S., and Akase, T. (2015), "Applicability Evaluation of Steel Plate Reinforced Concrete Structure to Primary Containment Vessel of BWRs: (2) Mechanical and Thermal Properties of Steel under High Temperature Conditions," *Transactions of SMiRT 23*, IASMIRT, Manchester, U.K.

Hong, S. and Varma, A.H. (2009), "Analytical Modeling of the Standard Fire Behavior of Loaded CFT Columns," *Journal of Constructional Steel Research*, Vol. 65, No. 1, pp. 54–69.

Ji, X., Cheng, X., Jia, X., and Varma, A.H. (2017), "Cyclic In-Plane Shear Behavior of Double-Skin Composite Walls in High-Rise Buildings," *Journal of Structural Engineering*, ASCE, Vol. 143, No. 6. https://doi.org/10.1061/(ASCE)ST.1943-541X.0001749

Kitajima, Y., Tanabe, M., Hirako, S., Hirama, T., Kumagai, H., and Abiru, T. (2017), "Applicability Evaluation of Steel Plate Reinforced Concrete Structure to Primary Containment Vessel of BWRs: (8) Shear Loading Test of Steel Plate Reinforced Concrete Structure under High Temperature Conditions," *Transactions of SMiRT 24*, IASMIRT, Busan, Republic of Korea.

Kodur, V., Dwaikat, M., and Fike, R. (2010), "High Temperature Properties of Steel for Fire Resistance Modeling of Structures," *Journal of Material and Civil Engineering*, Vol. 22, pp. 423–434.

Kurt, E.G., Varma, A.H., Booth, P.N., and Whittaker, A. (2016), "In-Plane Behavior and Design of Rectangular SC Wall Piers without Boundary Elements," *Journal of Structural Engineering*, ASCE, Vol. 142, No. 6.

Naus, D.J. (2009), "A Compilation of Elevated Temperature Concrete Material Property Data and Information for Use in Assessments of Nuclear Power Plant Reinforced Concrete Structures," Oak Ridge National Laboratory, prepared for U.S. Nuclear Regulatory Commission.

NRC (2011), "Design Control Document for AP1000," U.S. Nuclear Regulatory Commission, Washington, D.C.

NRC (2012), "Design Control Document for US-APWR," U.S. Nuclear Regulatory Commission, Washington, D.C.

NRC (2020, May), "Safety-Related Concrete Structures for Nuclear Power Plants (Other than Reactor Vessels and Containments)," *Regulatory Guide 1.142*, Rev. 3, U.S. Nuclear Regulatory Commission, Washington, D.C.

NRC (2021, August), "Safety-Related Steel Structures and Steel-Plate Composite Walls for Other Than Reactor Vessels and Containments," *Regulatory Guide 1.243*, Rev. 0, U.S. Nuclear Regulatory Commission, Washington, D.C.

Ozaki, M., Akita, S., Oosuga, H., Nakayama, T., and Adachi, N. (2004), "Study on Steel Plate Reinforced Concrete Panels Subjected to Cyclic In-Plane Shear," *Nuclear Engineering and Design*, Vol. 228, pp. 225–244.

Schlaseman, S. and Russell, J. (2004), "Application of Advanced Construction Technologies to New Nuclear Power Plants," *Report MPR-2610*, Rev. 2, Report for U.S. Department of Energy, under contract for DE-AT01-02NE23476.

Selvarajah, R. (2013), "Behavior and Design of Earthquake-Resistant Dualplate Composite Shear Wall Systems," Doctoral Dissertation, Purdue University, West Lafayette, Ind.

Sener, K.C., Bhardwaj, S.R. and Varma, A.H. (2019a), "Effects of Accident Thermal Loading on Shear Behavior of Reinforced Concrete Members," *ACI Structural Journal*, Vol, 116, No. 3. DOI: 10.14359/51713305.

Sener, K.C., Varma, A.H., and Bhardwaj, S.R. (2015a), "Accident Thermal Loading Effects on Seismic Behaviour of Safety-Related Nuclear Structures," *Transactions of SMiRT 23*, Paper ID 701, IASMIRT, Manchester, UK, pp. 1–10.

Sener, K., Varma, A.H., Booth, P.N., and Fujimoto, R. (2015b), "Seismic Behavior of a Containment Internal Structure Consisting of Composite SC Walls," *Nuclear Engineering and Design*, Vol. 295, pp. 804–816, Elsevier Science. http://dx.doi.org/10.1016/j.nucengdes.2015.07.038

Sener, K.C., Varma, A.H., and Chu, M. (2019b), "Seismic Performance of an Idealized Steel-Plate Composite (SC) Structure Subjected to Accident Thermal Loading," *Nuclear Engineering and Design*, Vol. 352. https://doi.org/10.1016/j.nucengdes.2019.05.029

Seo, J., Varma, A.H., Sener, K. and Ayhan, D. (2016), "Steel-Plate Composite (SC) Walls: In-Plane Shear Behavior, Database, and Design," *Journal of Constructional Steel Research*, Vol. 119, pp. 202–215, Elsevier Science. http://dx.doi.org/10.1016/j.jcsr.2015.12.013

Simulia (2014), *ABAQUS 6.14 Documentation*, Dassault Systemes Simulia Corporation Providence, R.I.

Takeuchi, M., Hiramoto, M., Kumagai, N., Yamazaki, N., Kodaira, A., and Sugiyama, K. (1993), "Material Properties of Concrete and Steel Bars at Elevated Temperatures," *Transactions of SMiRT12*.

Varma, A.H., Lai, Z., and Seo, J. (2017), "An Introduction to Coupled Composite Core Wall Systems for High-Rise Construction," *Proceedings of the 8th International Conference on Composite Construction in Steel and Concrete*, Wyo.

Varma, A.H., Malushte, S.R., and Lai, Z., (2015), "Modularity & Innovation Using Steel-Plate Composite (SC) Walls for Nuclear and Commercial Construction," *Proceedings of the 11th International Conference on Advances in Steel-Concrete Composite Structures (ASCCS)*, Tsinghua University, Beijing, China. http://dx.doi.org/10.13140/RG.2.1.4665.4804

Varma A.H., Malushte S.R., Sener K., and Lai Z. (2014), "Steel-Plate Composite (SC) Walls for Safety Related Nuclear Facilities: Design for In-Plane Force and Out-of-Plane Moments," *Nuclear Engineering and Design*, Vol. 269, pp. 240–249, Elsevier Science. http://dx.doi.org/10.1016/j.nucengdes. 2013.09.019

Vecchio, F J. and Sato, J.A. (1990), "Thermal Gradient Effects in Reinforced Concrete Frame Structures," *ACI Structural Journal*, Vol. 87, No. 3, pp. 262–275.

Zhang, K., Varma, A.H., Malushte, S.R., and Gallocher, S. (2014), "Effect of Shear Connectors on Local Buckling and Composite Action in Steel Concrete Composite Walls," *Nuclear Engineering and Design*, Vol. 269, pp. 231–239, Elsevier Science. http://dx.doi.org/10.1016/j.nucengdes.2013.08.035

Electroslag Welding Applications for Steel Building Construction in Japan: A State-of-the-Art Review

Yukihiro Harada, Jun Iyama, Yuka Matsumoto, Kazuaki Suzuki, and Koji Oki

---

ABSTRACT

Electroslag welding (ESW) is advantageous for the improvement of the efficiency of welding thick steel plates, and the application of ESW has been gradually spreading to civil structures such as steel bridges and steel building structures. This paper presents a review of state-of-the-art ESW application for steel building structures in Japan. A brief history of the development of ESW technology, which involves the installation of interior diaphragm plates in welded built-up box columns for high-rise steel buildings, is first introduced, followed by a recent recommendation for the design and fabrication of ESW joints to prevent brittle fracture under earthquake loading.

Keywords: electroslag welding, built-up box column, interior diaphragm, brittle fracture, seismic application.

INTRODUCTION

Electroslag welding (ESW) was originally developed in the Soviet Union in 1951, initially as an efficient vertical welding method. It was developed to complete the joining process by simultaneously melting and solidifying the solid electrode wire and base metal in the molten slag by enclosing a large weld pool with a water-cooled copper sliding plate (Yamaguchi, 1997; Chambers and Manning, 2016), as shown in Figure 1. ESW could significantly improve the efficiency of welding thick steel plates; thus, this welding method was first implemented as a welding technology in shipbuilding in response to a demand for improved productivity and economic efficiency.

The ESW method has various advantages over general arc welding. First, it can efficiently weld a wide range of plate thicknesses in a single pass, resulting in less heat distortion than that of arc welding with multiple passes. Second, because arc heat is not used as a heat source, spatter generation is reduced, and shielding gas supply is not required, resulting in superior welding workability. Third, it has a wide margin of accuracy for groove processing and can be welded with a square groove without gas cutting; therefore, the bevel preparation is simple. However, owing to the high welding heat input, the ESW has a disadvantage that the crystal grains of the weld metal and heat affected

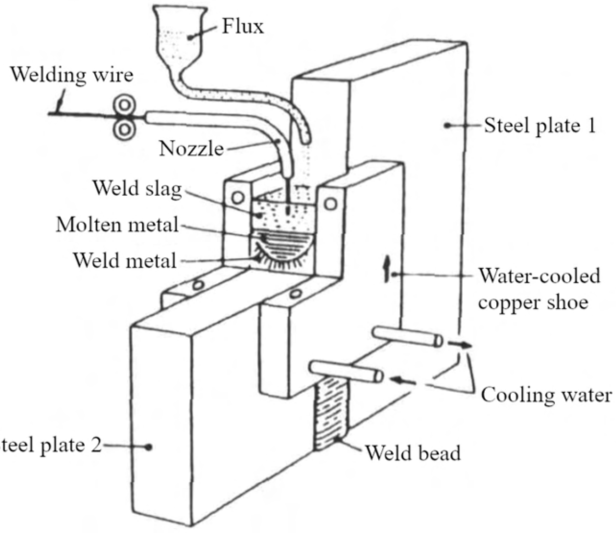

Fig. 1. Schematic of the earliest ESW (adapted from Yamaguchi, 1997).

Yukihiro Harada, Professor, Department of Architecture, Faculty of Engineering, Chiba University, Chiba, Japan. E-mail: yharada@faculty.chiba-u.jp (corresponding)

Jun Iyama, Associate Professor, Department of Architecture, Faculty of Engineering, University of Tokyo, Tokyo, Japan. E-mail: iyama@arch1.t.u-tokyo.ac.jp

Yuka Matsumoto, Professor, Department of Architecture and Building Science, College of Urban Sciences, Yokohama National University, Yokohama, Kanagawa, Japan. E-mail: matsumoto-yuka-kg@ynu.ac.jp

Kazuaki Suzuki, Architectural Committee, Japan Iron and Steel Federation, Nihonbashi Kayabacho, Tokyo, Japan (Nippon Steel Corporation). E-mail: suzuki.953.kazuaki@jp.nipponsteel.com

Koji Oki, Architectural Committee, Japan Iron and Steel Federation, Nihonbashi Kayabacho, Tokyo, Japan (JFE Steel Corporation). E-mail: k-oki@jfe-steel.co.jp

Paper No. 2022-10

Table 1. Timeline of ESW Development for Building Structures in Japan

1951	ESW was developed in the Soviet Union
1965	First ESW application to shipbuilding at Kawasaki Heavy Industry in Japan
1968	Kasumigaseki Building completed; the first full-fledged application of ESW to steel building structures in Japan
1970–1971	Two-sided ESW for weld box column was developed
1971	Four-sided ESW for weld box column was developed
1971	"Specification of Consumable ESW" published by Architectural Institute of Japan
1990s	Simplified nonconsumable ESW was developed
1995	Hyogo-ken Nanbu Earthquake
2016	"Guidebook for Prevention of the Occurrence of Brittle Fractures of Inner Diaphragm Plate Electroslag Welds" published by Japanese Society of Steel Construction

zone (HAZ) tend to be coarsened, making it difficult to obtain high toughness, which may be a serious problem in steel structures, particularly in seismic applications.

In the United States, ESW applications have spread to civil steel structures due to their high welding efficiency. The application of ESW for steel structures began in steel bridges (Chambers and Manning, 2016). However, problems with ESW joints were found in several steel bridges in the 1970s, and thus ESW has not been widely used in steel bridges. The situation is similar for steel building structures. There have been limited applications of ESW for steel building structures in the United States (e.g., Agic and Hampton, 1968). Recently, the ESW has been successfully applied to weld gusset plates to embedded panels and box columns to connect seismic buckling braces at the Wilshire Hotel in downtown Los Angeles, California (Lee et al., 2014).

In contrast, in Japan, using ESW to install interior diaphragm plates in welded built-up box columns for the construction of high-rise steel buildings is a common practice. This paper aims to present state-of-the-art research and development on ESW applications in steel building structures in Japan. A history of ESW technology development is first presented in Table 1, and then the essence of a design recommendation on ESW welding of interior diaphragm plates, which was recently published based on a series of research coordinated by the Japan Iron and Steel Federation, is introduced. Welding thicker steel plates by using technologies like ESW is expected to increase, particularly in earthquake-prone countries, as more tall buildings are being constructed. Furthermore, experience and knowledge gained on ESW in Japan over the years is expected to benefit for the future development of high-rise building structures worldwide.

DEVELOPMENT OF ESW FOR STEEL BUILDING STRUCTURES IN JAPAN

The Beginning of ESW Application to Building Steel

In 1964, a simplified ESW method with a consumable nozzle and fixed cooling plates was developed and implemented by several Japanese companies, as shown in Figure 2 (Ishiguro et al., 1975), which was applied to the outer panel of a ship for the first time (Yamaguchi, 1997). The consumable nozzle melts and gets consumed as the welding progresses; thus, the nozzle lift mechanism that is used with the conventional consumable ESW, as shown in Figure 1, is unnecessary. The disadvantage of this method is that the weld length is limited to the length of the consumable nozzle.

The simplified consumable ESW was first used in 1965 for the construction of steel building beam-to-column connections; the Kintetsu Terminal Building in Nagoya was one of the earliest applications (Sakurai and Takahara, 1966). Thereafter, the efficiency of welding thick steel plates for building applications became a major concern. At that time, concerns were raised regarding the decrease in the toughness of heat affected steel materials around ESW joints due to high heat input (Yamaguchi, 1997).

In the Kasumigaseki Building in Tokyo, which was completed in 1968 with the height of 147 m and is recognized as the first high-rise building in Japan, ESW was adopted in earnest to build the steel frameworks. Thick I-beams were used for both columns and beams. The beam-to-column connection was a split-tee type, and a consumable nozzle type ESW was adopted to efficiently weld the beam flange and the top plate of the tee, as shown in Figure 3 (Ueno and Ariyasu, 1968; Matsumoto, 2000).

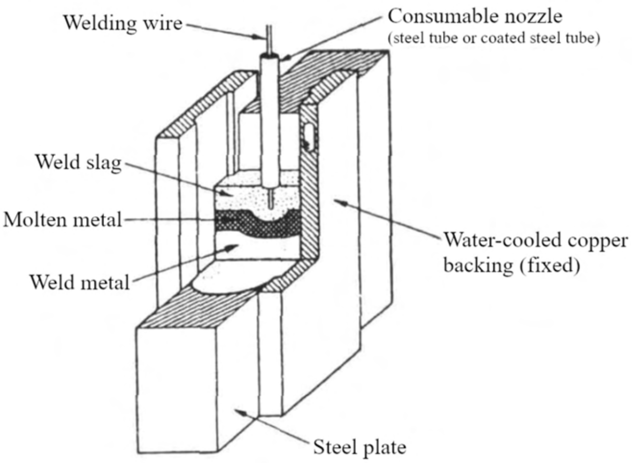

Fig. 2. Schematic of simplified consumable ESW (adapted from Yamaguchi, 1997).

In the 1960s, wide-flange (H-section) shapes were widely used for columns in high-rise steel buildings because wide-flange steel was less expensive than a box section. However, structural designers considered the box section to be structurally more efficient than the wide-flange shape. During that era, two fabrication procedures for built-up box columns were used. Figure 4(a) shows one approach in which each diaphragm plate had to be extended beyond one face of the column; the flange plate of the column at that face also had to be made discontinuous first and to be welded later. Figure 4(b) shows the second approach, in which a beam-to-column connection assembly was inserted between two column segments. Both approaches were labor intensive and expensive—and therefore not widely adopted.

This situation changed after ESW was introduced to weld interior diaphragms in built-up box columns in the 1960s, which significantly reduced the fabrication cost, especially for columns with thicker plates. With this method, faceplates of the column could be made continuous without the need to cut and re-weld. Since then, shop-welded built-up box columns with ESW have been widely used for high-rise steel building construction in Japan.

In the earliest application of ESW, three sides of a box column were first assembled in a U-shape as shown in

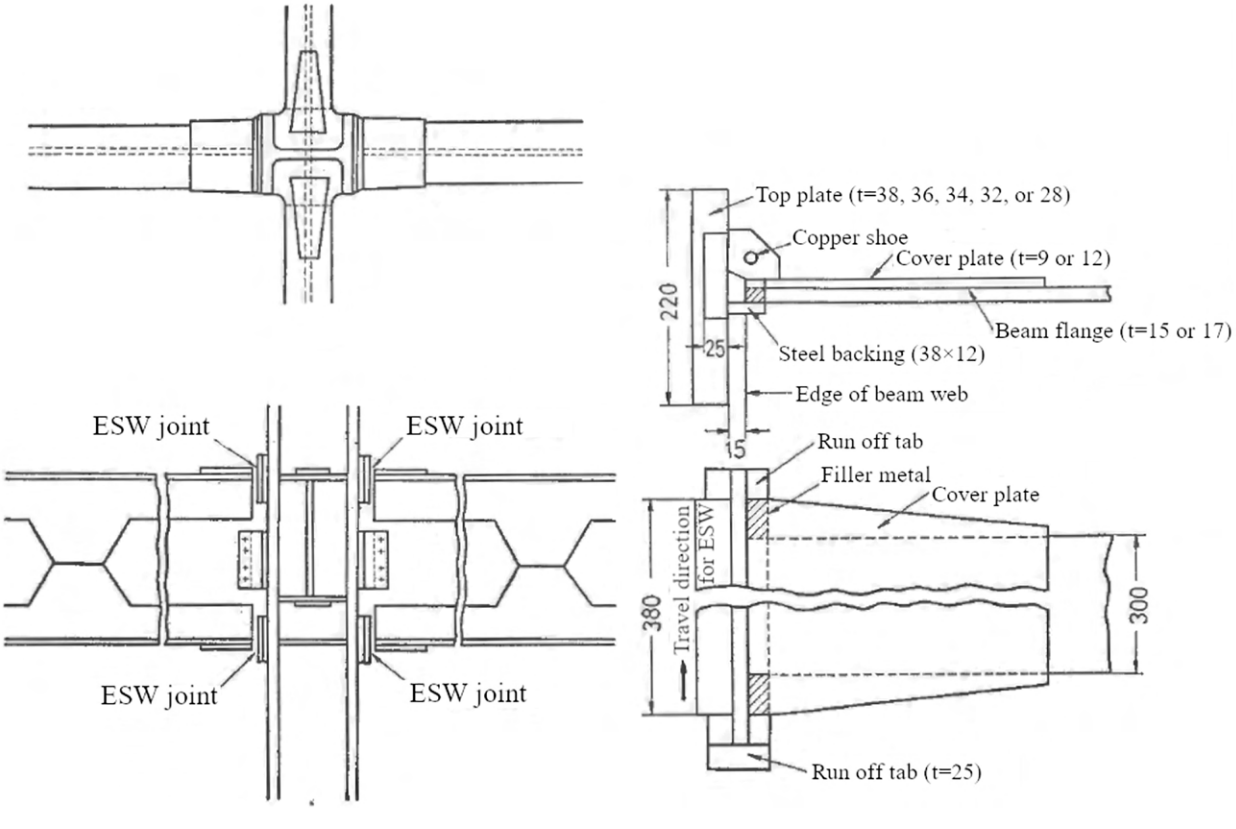

Fig. 3. ESW applications in Kasumigaseki Building (unit: mm) (adapted from Ueno and Ariyasu, 1968).

Figure 5(a). After that, three sides of the interior diaphragm plate were manually welded to the column plates. In this method, the column plates distorted by the weld heat, and the distorted column faceplates had to be straightened. After enclosing the box column with the remaining faceplate, the fourth side of the interior diaphragm plate, which was enclosed within the box column, was welded with the consumable ESW as shown in Figures 5(b) and (c) (Japan Welding Engineering Society, 2004). Since welding with ESW introduced a large amount of heat input, a considerable amount of effort was required again to straighten the distorted face plates.

A two-sided ESW method was developed in 1970 to solve these problems. In this fabrication method, the column was assembled in a U-shape, and only two sides of the diaphragm plate were manually welded with semi-automatic CO_2-gas shielded metal arc welding. With the enclosing plate in position, then ESW was applied to complete the remaining two welds of the diaphragm plate (Japan Welding Engineering Society, 2004). After the two-sided ESW method was introduced for several years, a four-sided ESW method was developed in 1971, as shown in Figure 6. In response to this trend in ESW applications to steel building structures, the Architectural Institute of Japan (AIJ) published the welding standard for consumable ESW in 1971 (AIJ, 1971). In the 1980s when the labor cost became more expensive, fabricators were motivated to automate steel fabrication and preferred the four-sided ESW method. Since then, the four-sided ESW method has been a standard practice for welding interior diaphragm plates in built-up box columns.

Development of Simplified Nonconsumable ESW

Because the consumable ESW had been widely applied in fabricating built-up box columns for high-rise construction, the disadvantage of the consumable ESW had become recognized. The high heat input [several hundred thousand Joules per centimeter (several hundred thousand Joules per in.)] due to the low travel speed (less than several centimeters per minute) produced a HAZ with mechanical properties significantly deteriorated (Wada et al., 1990).

One of the solutions to avoid these defects was to develop a highly efficient welding method with a reduced heat input. A simplified nonconsumable ESW method with an elevating nozzle was developed by Nippon Steel Corporation (Nippon Steel Welding & Engineering, 2019) to address the problem in 1980s, as shown in Figure 7. The welding process is called by its trade name ("simplified electroslag

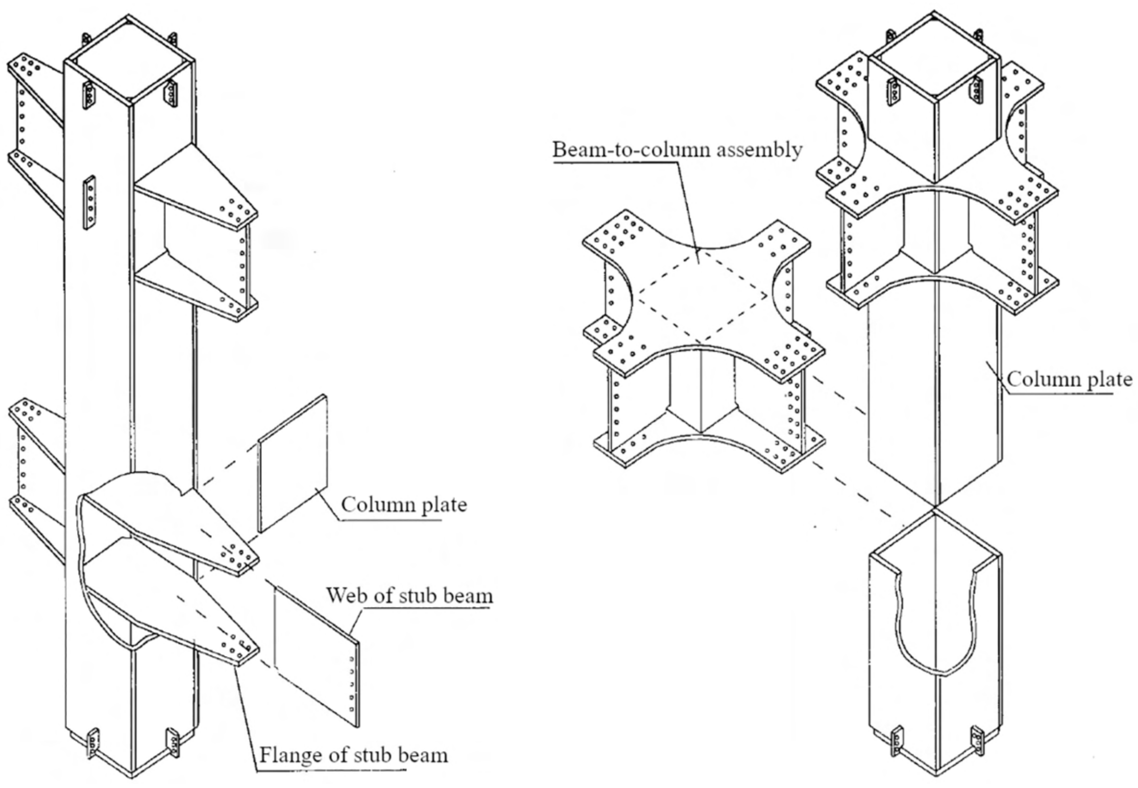

(a) Extended beam flange type

(b) Beam-to-column assembly type

Fig. 4. Box column fabrication before ESW application (adapted from Japan Steel Structure Journal*, 1998).*

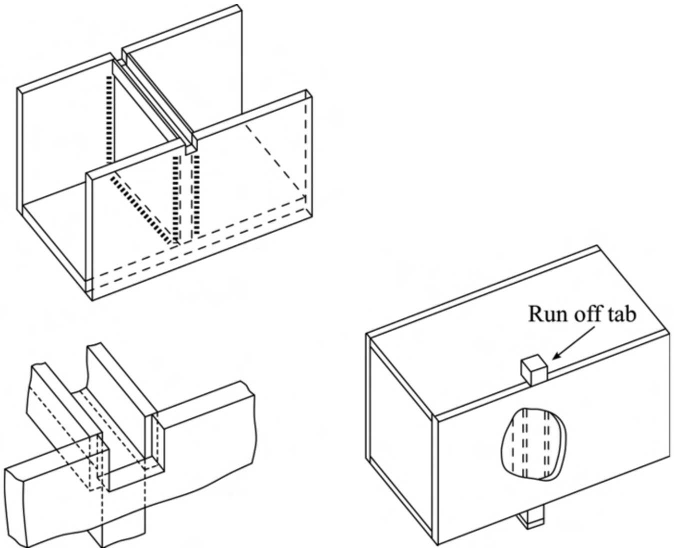

Fig. 5. First application of ESW for interior diaphragms of box columns (adapted from Japan Welding Engineering Society, 2004).

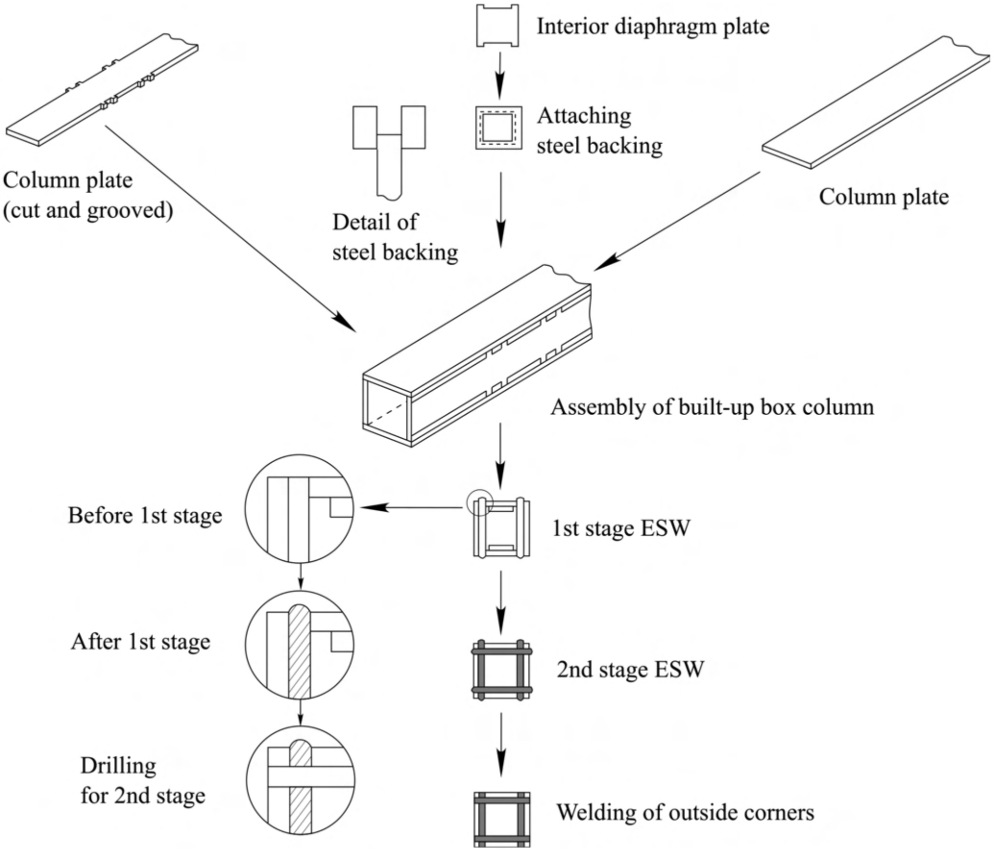

Fig. 6. Four-sided ESW method in current practices (adapted from Japan Welding Engineering Society, 2004).

welding process with nonconsumable elevating tip") and has been applied to almost all diaphragm welding of box column in Japan.

The welding wire in this process is fed into the welding slag in a groove through a nonconsumable nozzle at an electrode extension that depends on the welding current. A high travel speed is possible with a thin weld wire of 1.6 mm and a longer electrode extension. The welding speed was approximately doubled, and the heat input was reduced by about a half. The simplified nonconsumable ESW is also economical because it does not require consumable nozzles and the cooling plates were omitted. The heat source can be increased to obtain sufficient melting by oscillating the nozzle in the direction of the diaphragm thickness. With the simplified ESW, almost the same welding conditions can be used regardless of the diaphragm thickness, making the operation more effortless. The nozzle moves upward automatically as the welding progresses, allowing almost unsupervised welding after welding initiation. Therefore, multiple ESW units can be operated simultaneously by a single person.

RECOMMENDATIONS FOR BRITTLE FRACTURE PREVENTION OF INTERIOR DIAPHRAGM ELECTROSLAG WELDS

Background of the Publication of the Recommendation

The Hyogo-ken Nanbu Earthquake in 1995 caused significant damage to steel structures, and this event was recognized as the first one in which many brittle fracture damages were observed in beam-to-column connections in steel building structures in Japan. The typical fracture involved a crack initiating from the beam flange weld in through-diaphragm-type beam-to-column connections, as shown in Figure 8(a). No damage was reported on the ESW joint in welded box columns, as shown in Figure 8(b).

A series of dynamic loading tests on full-scale beam-to-column subassemblages was conducted after the earthquake, and fracture at the ESW part in the interior diaphragm of built-up box columns was observed (Akiyama et al., 2002); this failure mode was similar to the fracture observed in the through-diaphragm-type beam-to-column connections. In the beam-to-built-up box column connection, a brittle

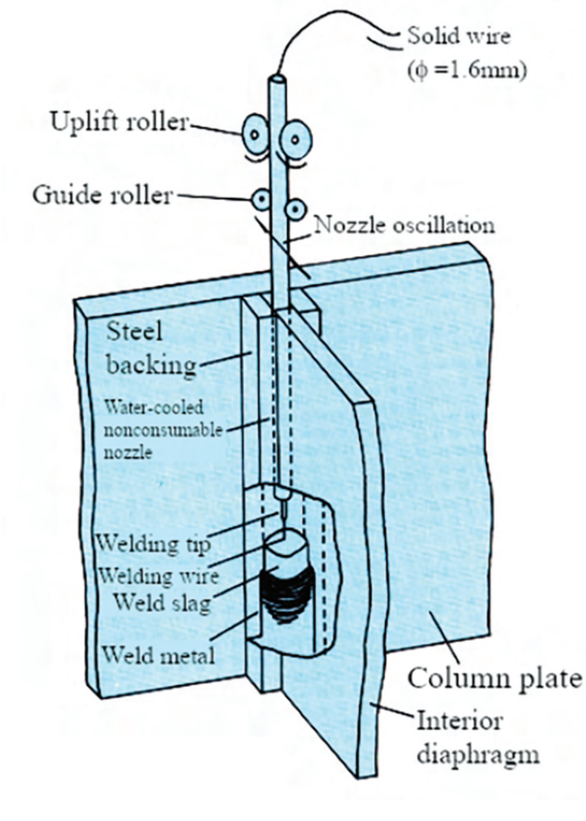

Fig. 7. Simplified nonconsumable ESW (adapted from Nippon Steel Welding & Engineering, 2019).

fracture initiating from the slit tip—that is, the tip of the slit, which is the gap between the column face plate and a steel backing—in the ESW part was observed, as shown in Figures 9 and 10. This was the first reported brittle fracture case of an ESW joint for steel building construction in Japan. This failure mode drew a strong interest from the engineers and researchers involved in high-rise steel building construction because there had been concerns about the decrease in the toughness of heat affected steel materials around the ESW due to high heat input presented earlier.

A series of coordinated research on fracture prevention of the ESW joint was then conducted in Japan starting in the early 2000s (Shimanuki et al., 2003). For the column

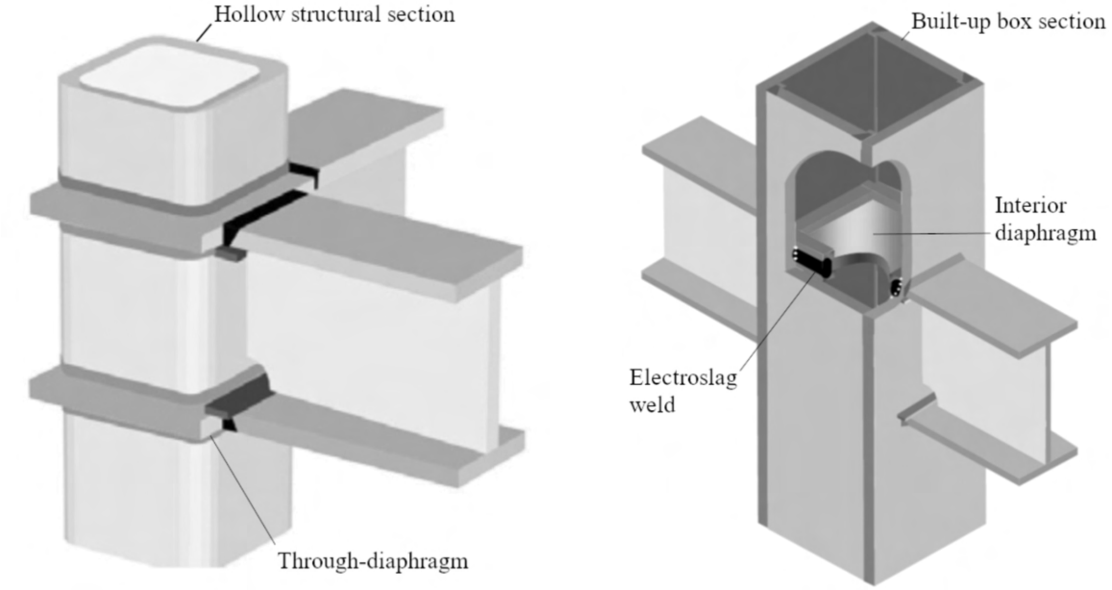

(a) Through-diaphragm-type beam-to-column joint

(b) Interior diaphragm type

Fig. 8. Types of beam-box column joints (adapted from JSSC, 2016b).

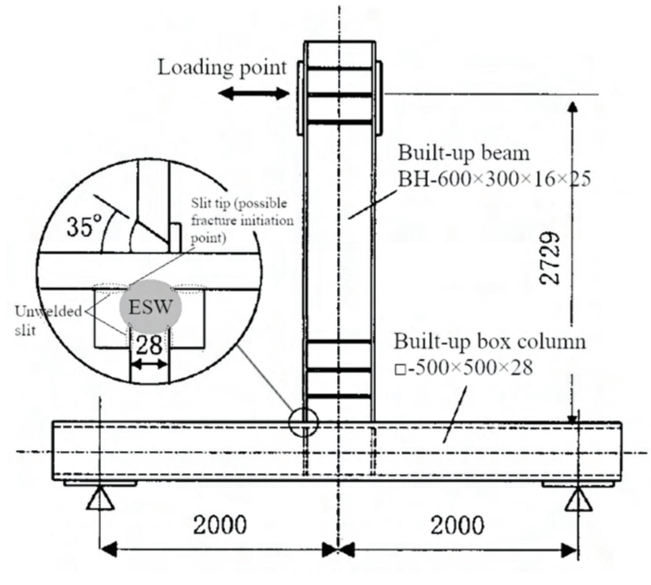

Fig. 9. Example of subassemblage specimen with fractured ESW at the interior diaphragm (unit: mm) (adapted from Akiyama et al., 2002).

plates, the studies focused on a commonly used 490 N/mm^2 (71 ksi) class steel (by ultimate strength) in the SN grade steel, which is specified as rolled steels for building structure in Japanese Industrial Standards. Both loading tests and numerical simulations were conducted to determine the failure mechanism in the ESW joint and identify conditions under which brittle fracture would occur. Two types of loading tests were conducted to reproduce the fracture of the ESW joint: biaxial tensile tests of ESW joints, as shown in Figure 11, and the beam-to-column subassemblage tests with built-up box columns incorporating interior diaphragms welded by ESW. This coordinated research obtained considerable technical data and findings on the toughness of ESW welds required to avoid fracture. In 2016, the Japanese Society of Steel Construction (JSSC) published a recommendation entitled *Guidebook for Prevention of the Occurrence of Brittle Fractures of Inner Diaphragm Plate Electroslag Welds* (JSSC, 2016a), hereafter referred to as the *Guidebook*, to share the findings and provide recommendations for the three parties involved in steel building construction: structural designers, steel fabricators, and construction engineers.

Fundamental Idea of Fracture Prevention of ESW Joint at the Interior Diaphragm

Shimokawa et al. (2019) summarized the experimental results of a series of loading tests. Figure 12 shows an example of the observations from the testing of three beam-to-built-up box column subassemblage specimens. In the example, if the Charpy V-notch (CVN) value, E_v, at the HAZ, fusion zone (FL), or weld metal (WM) of the ESW joint was lower, brittle fracture would occur, and both the

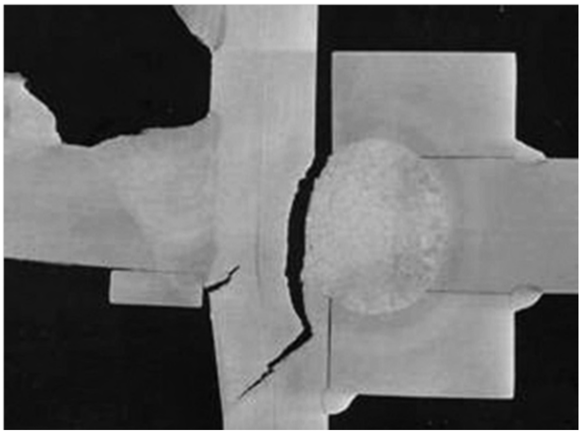

Fig. 10. Example of ESW joint fracture in beam-to-box column subassemlage loading tests (JSSC, 2016a).

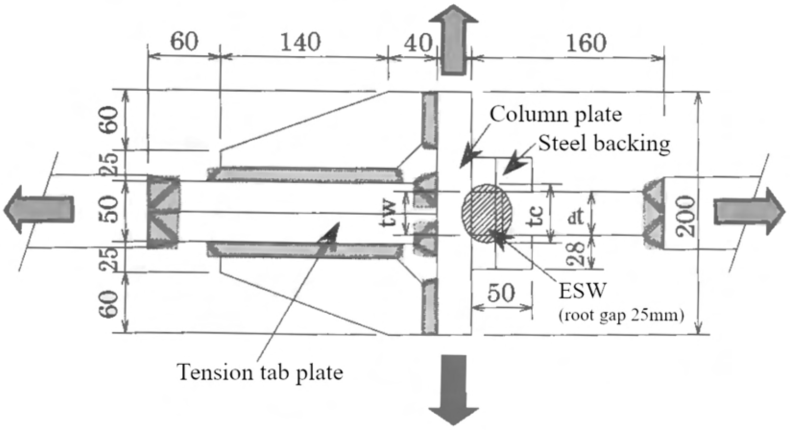

Fig. 11. Biaxial tensile test of ESW joint (unit: mm) (adapted from JSSC, 2016a).

ultimate strength and ductility were smaller (the sampling positions of CVN specimens for the HAZ, FL, and WM correspond to "HAZ1," "Bond," and "Depo1," respectively, in the later section, Weld Testing Method for ESW at the Interior Diaphragm). In Specimens H-2 [the smallest E_v = 14 J (11 ft-lb) at the fusion zone] and H-3 [the smallest E_v = 14 J (11 ft-lb) at the weld metal], a crack initiated at the slit tip and propagated from the interface between the ESW joint and the HAZ, and then propagated to the column plate due to the tensile force acting perpendicular to the HAZ at the slit tip, as shown in Figures 12(c) and (d). In contrast, Specimen H-1 (the smallest E_v = 69 J (51 ft-lb) at the weld metal) showed a ductile fracture at the interior diaphragm, not at the ESW joint, as shown in Figure 12(b). Based on the results from a series of experiments, the following findings were confirmed:

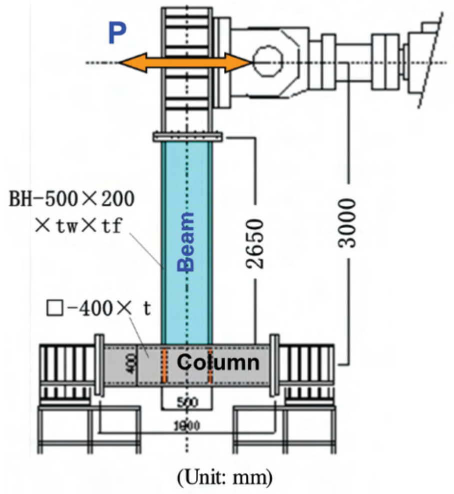

No.	Column		Beam section	Test temp.
	Section	Steel		
H-1	□-400×28	High toughness SN490C	SN490B BH-500×200×22×40	−20°C
H-2				−40°C
H-3				−40°C

No.	Column	Test temp.	HAZ		F.L.		W.M.	
			E_v (J)	B (%)	E_v (J)	B (%)	E_v (J)	B (%)
H-1	High toughness SN490C	−20°C	74	72	75	77	69	73
H-2		−40°C	29	91	14	97	44	82
H-3		−40°C	19	94	18	93	14	92

(B: percent brittle fracture)

(a) Outline of the subassemblage tests

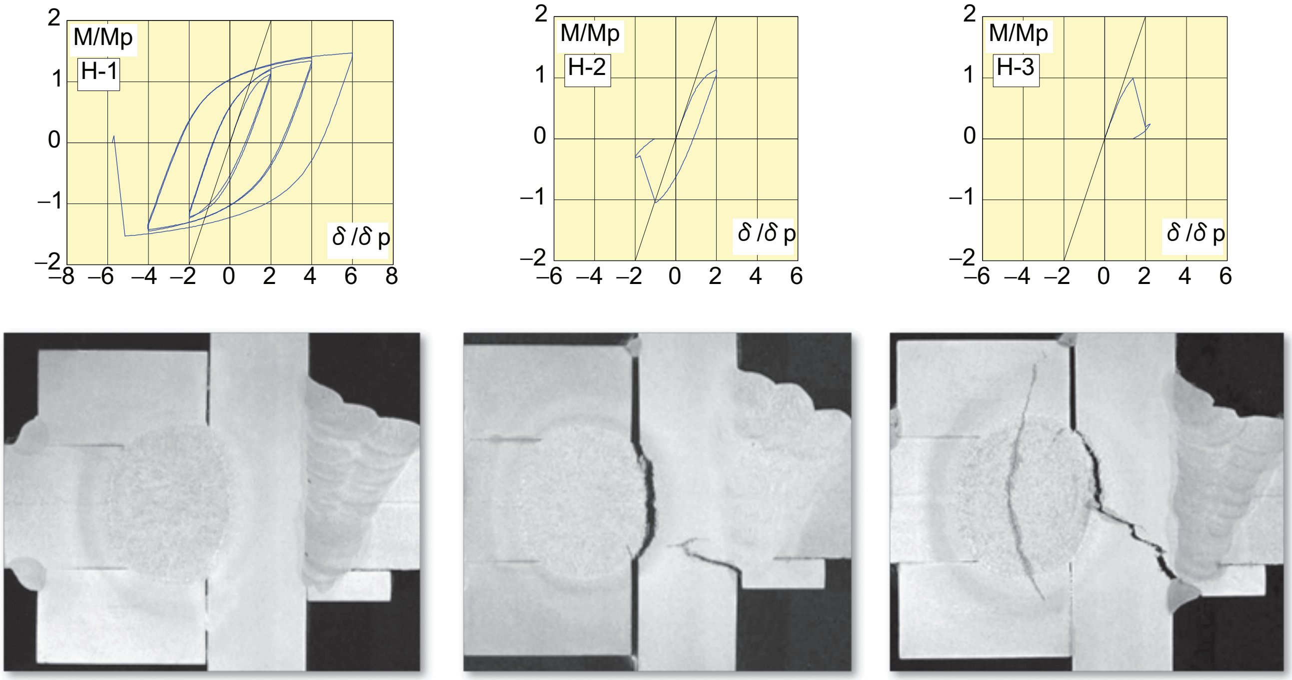

(b) Specimen H-1 *(c) Specimen H-2* *(d) Specimen H-3*

Fig. 12. Example results of beam-to-built-up box column subassemblage loading tests (adapted from Shimokawa et al., 2019).

1. Brittle fracture was caused by the crack initiation and propagation from the slit tip at the ESW joint.
2. Brittle fracture did not occur in specimens with CVN toughness at the designated zone where brittle fracture could initiate exceeding 47 J at 0°C (35 ft-lb at 32°F).
3. A positive correlation existed between the nominal tensile stress acting on the ESW joint and the toughness at the zone when the brittle fracture would occur.

Based on the findings of the loading test results, it is essential to limit the applied tensile stress acting on the interior diaphragm to prevent brittle fracture of ESW joint. Figure 13 shows a schematic of the tensile forces acting on the ESW joint. The tensile force acting on the interior diaphragm, P_d, is determined from horizontal equilibrium with the tensile forces P_f and P_w acting on the beam flange and web, respectively. The driving force P_{req} to tear the slit tip in the HAZ of the ESW joint is dominated mainly by P_d, combined with the tensile forces P_c acting on the column plate. The required driving force P_{req} to initiate brittle fracture at the slit tip is a function of the toughness near the slit tip. Thus, limiting P_d (or the nominal tensile stress σ_d at the critical cross-section of the ESW joint) to a sufficiently small value is essential to prevent brittle fracture. An evaluation procedure to determine whether fracture will occur at the ESW joint is provided in the *Guidebook*, as shown in Figure 14. The fundamental idea is that the nominal tensile stress, σ_d, at the ESW joint should be limited to a threshold value, which is dependent on the CVN toughness of the ESW joint. The procedure to determine the CVN toughness is also provided in the *Guidebook*.

The nominal tensile stress limit for the interior diaphragm was established from the biaxial tensile test results and the subassemblage loading test results. Figure 15 shows the relationship between the ultimate strength of the ESW joints and the CVN toughness (at the zone where the brittle fracture initiated in the ESW joint). Each data point in the figure corresponds to a single test in which the brittle fracture occurred at the ESW joint. In this figure, the ultimate strengths of the joints P_u were normalized by the nominal yield strengths of the ESW joint, P_{dy}. The nominal yield strength P_{dy} is defined as the product of the yield stress of the interior diaphragm and the effective cross-sectional area of the ESW joint, considering the penetration of ESW and the spread of the tensile stress as shown in Figure 16(a); the penetration depth notably affects the strength and deformation capacity of the subassemblage with ESW joints (Umeda et al., 2022). For the results of beam-to-column subassemblage tests, P_u was computed from Figure 16(b) as follows:

$$P_u = \frac{M_{cf}}{H_b - 2_{bf}t} \tag{1}$$

and thus the corresponding nominal tensile stress is

$$\sigma_d = \frac{P_u}{t_w(B_b + 2t_s)} = \frac{M_{cf}}{(H_b - 2t_{bf})t_w(B_b + 2t_s)} \tag{2}$$

where M_{cf} is the design maximum bending moment at the beam-end, H_b is the height of the beam, B_b is the width of the beam flange, t_{bf} is the thickness of the beam flange, t_w is the width of the ESW joint at the interior surface of the column plate surface, and t_s is the thickness of the column plate.

In Figure 15, it can be seen that the fracture resistance increases as the CVN value increases, although the scatter of fracture resistance is considerable. From these test results, a required CVN toughness to prevent the fracture at the ESW joint can be derived. In the figure, the lower bound of the E_v–P_u/P_{dy} relationship is roughly represented by a bilinear curve consisting of two parts: an increasing part for smaller E_v and the plateau at $P_u/P_{dy} = 1$ for larger E_v. The boundary between the two parts is $E_v = 47$ J (35 ft-lb), which means that the ESW joint will be expected to fully exert its yield strength if E_v exceeds 47 J (35 ft-lb). In contrast, if E_v is smaller than 47 J (35 ft-lb), the ESW joint will not bear tensile strength corresponding to the yield tensile stress; thus, the maximum nominal tensile stress will decrease for smaller E_v. The bilinear relationship therefore gives a required CVN toughness to prevent the fracture corresponding to P_u/P_{dy}.

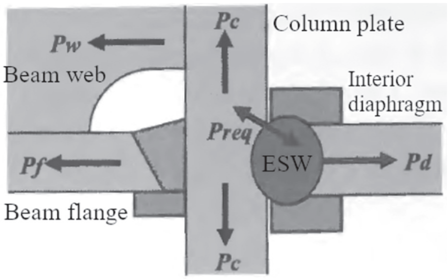

Fig. 13. Tensile forces acting at the ESW joint (adapted from JSSC, 2016a).

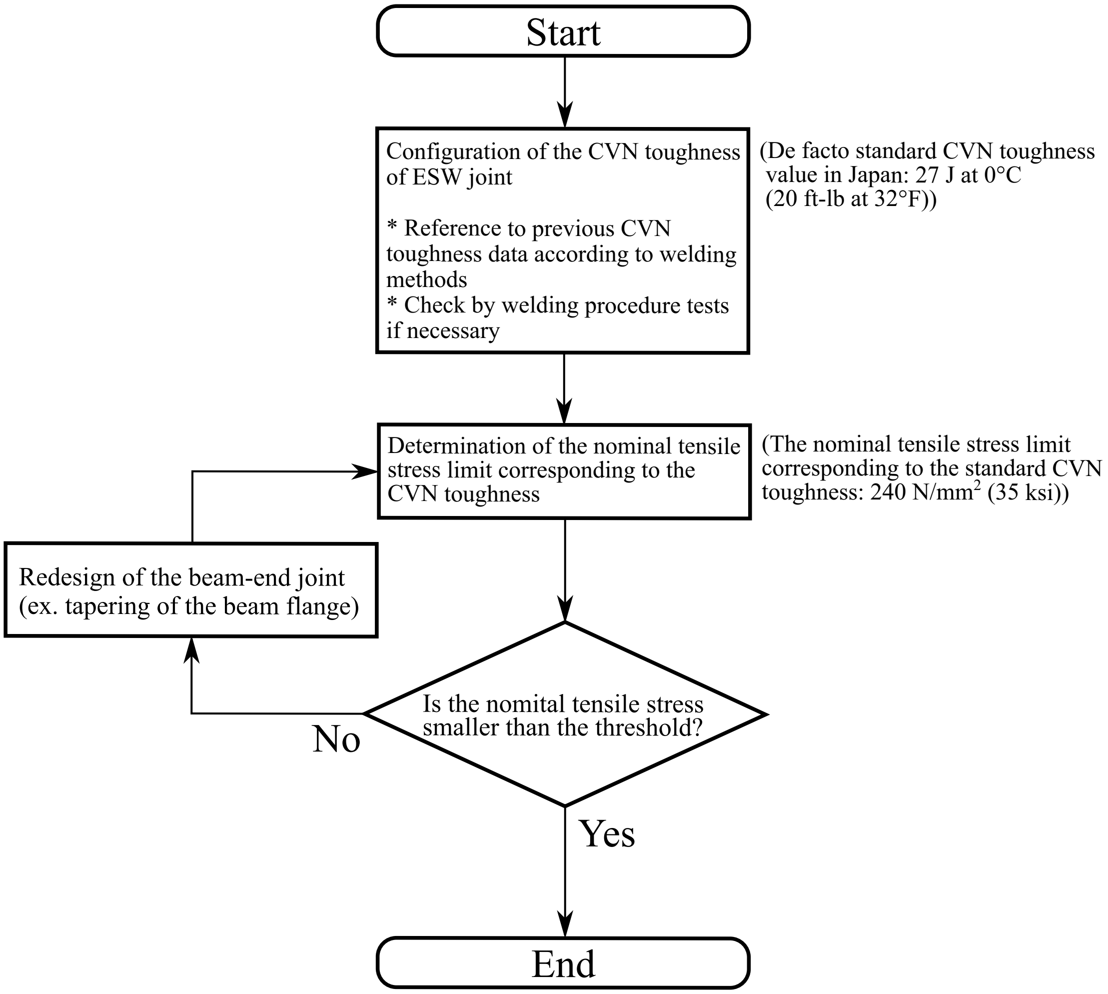

Fig. 14. Procedure of fracture prevention design of ESW joints at interior diaphragms (adapted from JSSC, 2016a).

In the *Guidebook*, the limiting values for the nominal tensile stress are listed in Table 2 as a simpler representation of the bilinear curve in Figure 15. As shown in the table, the toughness level of 15 J (11 ft-lb) is specified as the minimum requirement, whereas the next level of 27 J (20 ft-lb) is considered the de facto standard toughness level in Japan. The highest level of 47 J (35 ft-lb) is specified as the required toughness for the interior diaphragm to attain its yield stress without experiencing brittle fracture at the ESW joint. These criteria are also included in a recent manual for standard mechanical tests of welds in steel building construction in Japan (JSSC, 2016b).

Note that the test results in Figure 15 also include the information on the tensile stress of the column plate as a tensile stress ratio, which is defined by the ratio of the nominal tensile stress due to axial force and bending moment on the column member to the yield stress. A higher axial tensile stress in the column plate would influence the occurrence of brittle fracture of the ESW joint, but the criteria in Table 2 are independent from the tensile stress ratio. To explicitly consider the effect of the tensile stress, the detailed assessment procedure to be presented in the next section can be used.

Detailed Assessment Scheme of the Possibility of ESW Fracture

The *Guidebook* also introduced a detailed assessment method to evaluate the risk of brittle fracture at the ESW joint. Because the ESW joint fracture is characterized by the fracture starting from the slit tip between the steel backing and column plate, it is necessary to consider the effect of local stress concentration—that is, to evaluate whether the fracture can be prevented by the fracture mechanics approach. In this detailed method, the concept is to limit the local tensile stress acting on the slit tip to be sufficiently smaller, depending on the toughness of the ESW joint. Such local approach would be necessary if the tensile stress acting on the column plate is high and a detailed check of the risk of fracture of ESW joints is required. The application of the procedure requires a deal of effort; refer to the *Guidebook* and the references in the *Guidebook* for more information. This method is versatile as it can be applied to steel other than the 490 N/mm^2 (71 ksi) class steel.

In the detailed assessment, the risk of fracture of the ESW joint is assessed using original indices γ_{req} and γ_{lim} related to the maximum principal stress at the slit tip between the interior diaphragm and the column plate. As imagined from

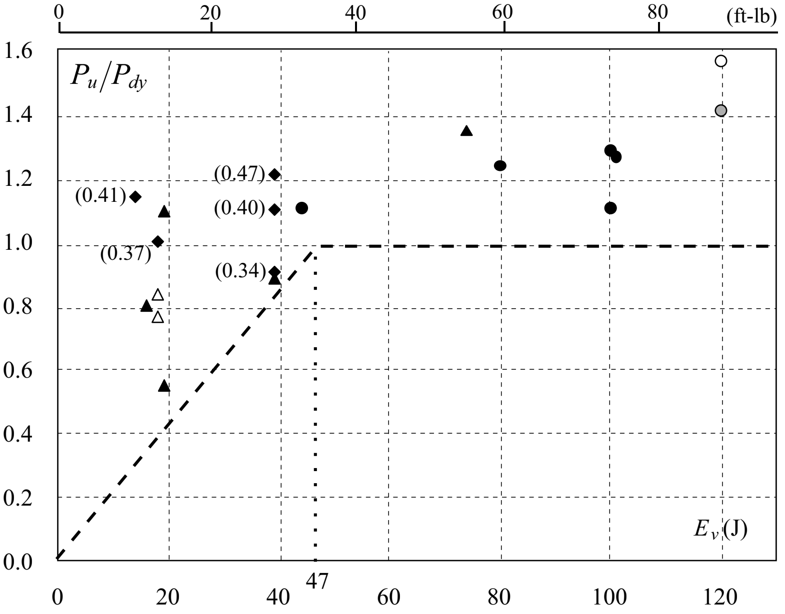

Location of crack initiation	Biaxial tensile test			Subassemblage test
	Tensile stress ratio			
	0	0.3	0.6	
Deposited metal	○	◍	●	-
HAZ	△	-	▲	(#)◆

(#) : The value in parentheses shows the tensile stress ratio corresponding to the nominal tensile stress due to bending moment at the experimental ultimate strength

Fig. 15. Maximum tensile resistance versus Charpy impact energy (adapted from JSSC, 2016a).

Table 2. Criteria for the Upper Limits of Tensile Stress Acting on the Interior Diaphragm (adapted from JSSC, 2016a)

Toughness level of the electroslag welds	15 J (11 ft-lb) or higher	27J (20 ft-lb) or higher	47 J (35 ft-lb) or higher
Criteria for the upper limits of acting stress	160 N/mm^2 (24 ksi) or less (0.5*F*)	240 N/mm^2 (35 ksi) or less (0.75*F*)	325 N/mm^2 (48 ksi) or less (1.0*F*)
F: Nominal yield stress for 490 N/mm^2 (71 ksi) class steel [= 325 N/mm^2 (48 ksi)]			

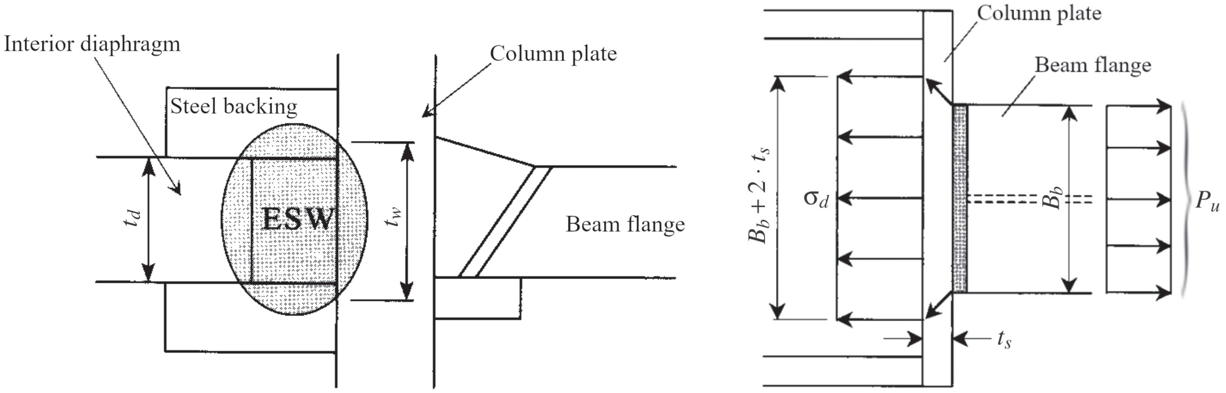

(a) Definition of effective cross-sectional area (adapted from JSSC, 2016a)

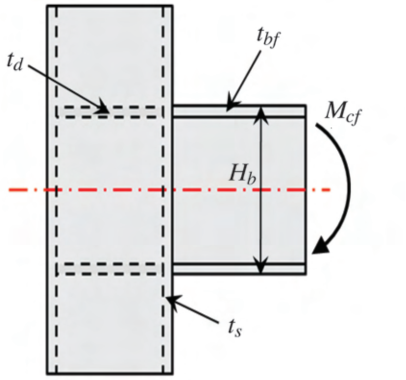

(b) Definition of beam-to-column subassembly dimensions

Fig. 16. Maximum nominal tensile stress in the interior diaphragm.

Figure 13, the existence of a high tensile stress in the column plate increases the magnitude of the principal stress at the slit tip, and thus the fracture resistance decreases. In addition, the higher tensile stress in the column plate would change the direction of the principal stress to make it aligned orthogonally to the direction of the slit. Thus, the driving force is more likely to initiate the opening of the crack at the slit tip.

Figure 17 shows the detailed assessment method. The required joint strength index γ_{req} is compared with the critical joint strength index γ_{lim}. If the condition $\gamma_{req} < \gamma_{lim}$ is satisfied, then the ESW joint is not expected to fracture. Otherwise, the joint detail or the design toughness of the ESW should be reconfigured; the assessment will be repeated until the condition is satisfied.

To determine the required joint strength index γ_{req}, the nominal tensile stress σ_d acting on the interior diaphragm was first calculated by Equation 2 presented in the previous section. The principal stress σ_{mreq} in the HAZ (at the slit tip in the ESW joint) corresponding to the calculated σ_d is then estimated through the σ_d–σ_m conversion curves, which were predetermined by finite element analyses, as shown in Figure 18. The σ_d–σ_m curves depend on the tensile stress ratio of the column plate, as shown in Figure 19. In the *Guidebook*, the σ_d/σ_u–σ_m/σ_u curves are given for the tensile stress ratio lower than or equal to 0.6. (In the Commentary in the *Guidebook*, the σ_d/σ_u–σ_m/σ_u curve for higher tensile stress ratio larger than 0.6 is also given, which was obtained by extrapolating the FEA results for lower stress ratios. However, the curve is not supported by experimental data.)

To determine limiting joint strength index γ_{lim}, the CVN value at a prescribed temperature T required in the design is first set. Kayamori et al. (2007) derived the correlation equation between the CVN value at HAZ of ESW joints and

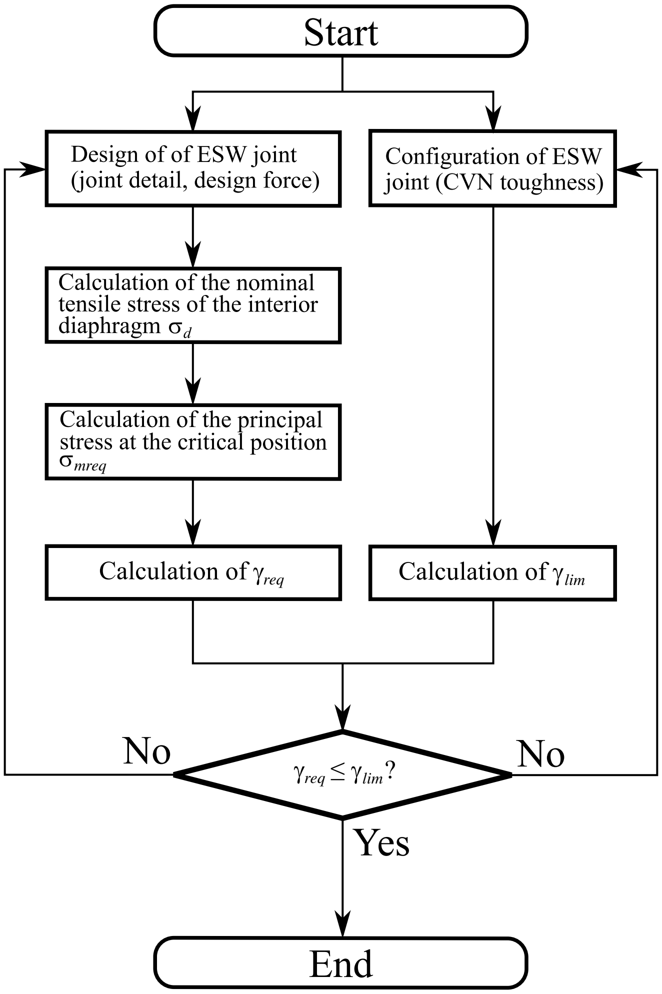

Fig. 17. Procedure for detailed assessment of fracture design of ESW joints (adapted from JSSC, 2016a).

the principal stress limit in the ESW joints by integrating loading test results, FEA results, and fracture mechanics-based investigation. The limiting joint strength index γ_{lim} corresponding to CVN is then calculated using the principal stress limit.

Weld Testing Method for ESW at the Interior Diaphragm

To examine the risk of brittle fracture of an ESW joint, it is necessary to evaluate the toughness of the ESW joint. Because the starting point of the fracture of an ESW joint is at the slit tip between the ESW joint and the steel backing and the point is close to the fusion zone (the boundary between the steel material and the weld metal), the *Guidebook* provides a clear procedure to sample CVN specimens in order to determine the toughness of the ESW joint; such unified procedure did not exist prior to the publication of the *Guidebook*.

For each ESW joint, V-notch specimens are sampled from three positions: the bottom of the V-notch is on the bond zone (Bond), 1 mm (0.039 in) toward the weld metal from the bond (Depo1), or 1 mm (0.039 in) toward the base metal from the bond (HAZ1) as shown in Figure 20. The reason the three positions are chosen is to evaluate the toughness

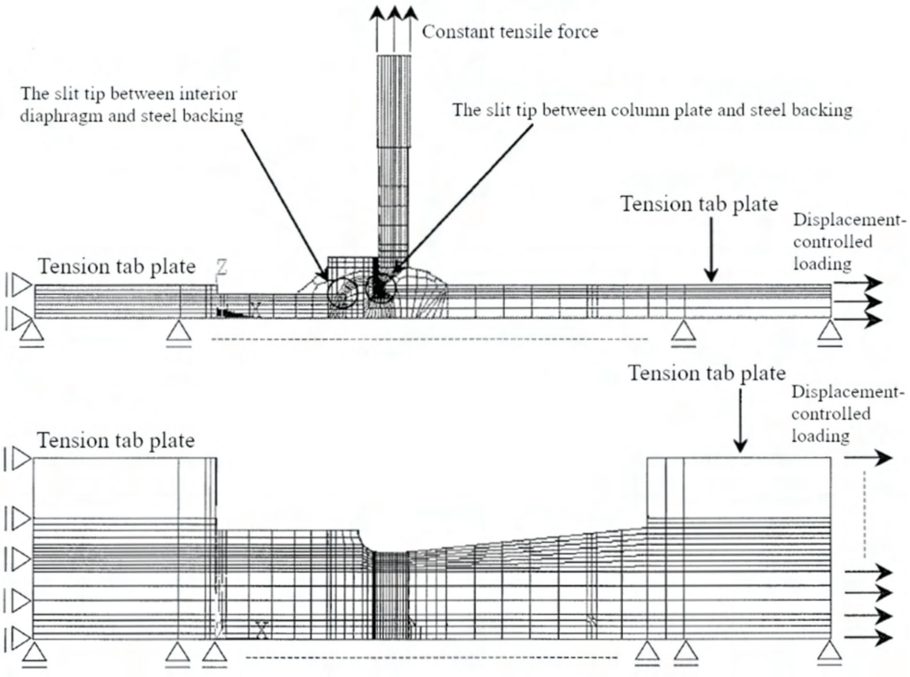

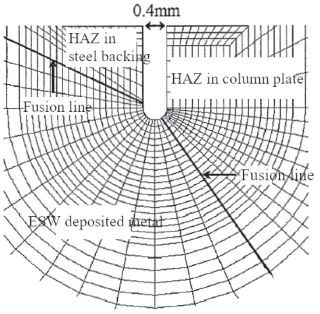

(Finite element mesh near the slit tip between column plate and steel backing)

(a) Finite element model

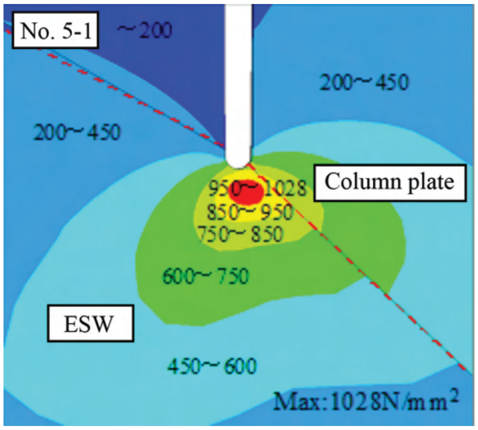

(b) Example of principal stress distribution near the slit tip between column plate and steel backing

Fig. 18. Principal stress distribution near the slit tip (adapted from Song et al., 2009).

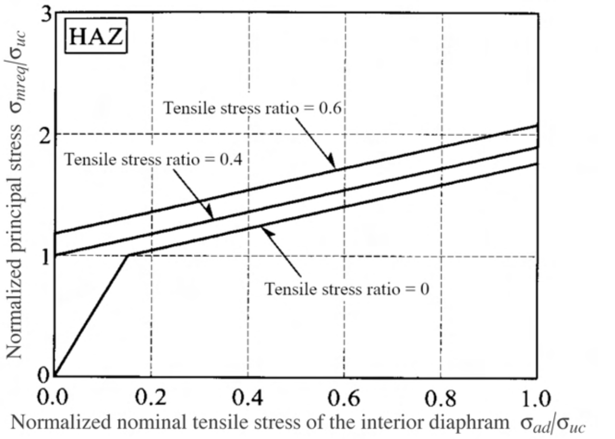

Fig. 19. Normalized principal stress versus normalized nominal tensile stress in the HAZ of ESW joint (adapted from JSSC, 2016a).

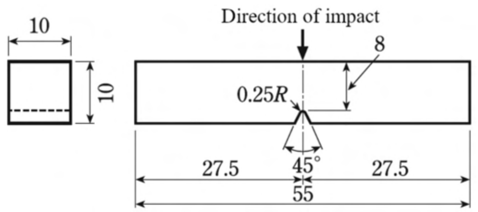

(a) CVN specimen (unit: mm) (adapted from JSSC, 2009)

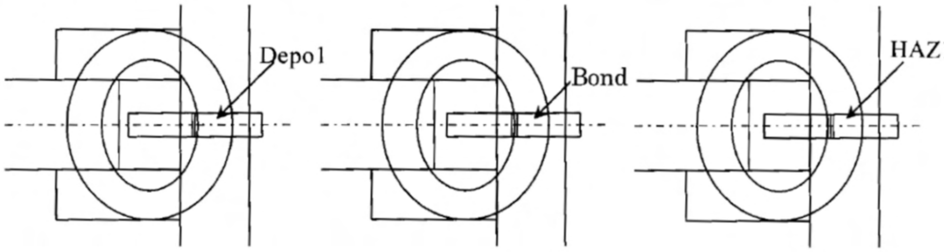

(b) Type A sampling (adapted from JSSC, 2016a and 2016b)
[An annular area represents the HAZ, as shown in Figs. 10 and 12(b)-(d)]

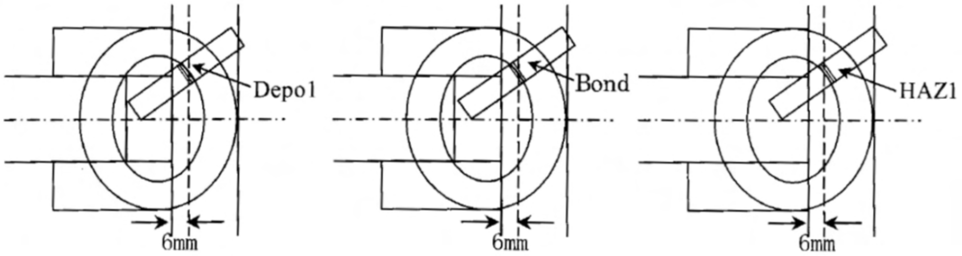

(c) Type B sampling (adapted from JSSC, 2016a and 2016b)

Fig. 20. Collection positions of Charpy V-notch test specimens.

of the material surrounding the slit tip. Figure 20(a) shows the specimen shape, which is the same defined as in ISO 148-1 (ISO, 2016). Three V-notch specimens at each notch position are required for a total of nine specimens. At each position, the average CVN value is calculated from three specimens, and the lowest average CVN value from Depo1, Bond, and HAZ1 represents the toughness of the ESW joint.

The Charpy V-notch specimens are collected such that the centerline of the interior diaphragm aligns with the centerline of the V-notch specimen, as shown in Figure 20(b). This is called Type A sampling in the *Guidebook*. This sampling method is relatively easy to position and to cut out the V-notch specimen. Therefore, this type of sampling has been widely adopted. However, it has been indicated that the measured Charpy energy decreases significantly, and the toughness of the ESW joint cannot be adequately evaluated if the ESW penetration into the column plate is significant. When this occurs, the bottom of the V-notch of the specimen is near the mid-thickness of the column plate. It is well-known that the toughness of steel is less in the through-thickness direction than in rolling or transverse direction, and the centerline segregation of steel plates may further reduce the toughness.

In addition to conventional Type A sampling, various V-notch specimen sampling methods were investigated to avoid inaccuracy in the toughness. To address the potential limitation of Type A sampling, Type B sampling method was introduced in the *Guidebook*, as shown in Figure 20(c). In Type B sampling, the longest edge of the V-notch specimen is not parallel to the centerlines of the interior diaphragm, unlike in Type A sampling. As shown in Figure 20(c), the specimen is oriented at the position where the V-notch is at or near the intersection between the line of the ESW joint and a line 6 mm (0.24 in) away from the back surface of the column plate. The choice of the sampling type depends on the extent to which the fusion line of the ESW joint is close to the mid-thickness of the column plate. In a recent manual for the mechanical test of weldment in steel building structures (JSSC, 2016b), however, Type B sampling is adopted as the standard sampling method for Charpy impact test specimens from the ESW at the interior diaphragm.

CURRENT AND FUTURE DEVELOPMENT

The *Guidebook* is intended for the 490 N/mm^2 (71 ksi) class of steel column plates, and the research challenge is to expand the application to high-performance steel. For example, a series of experimental studies on the ESW of SA440C steel, whose tensile stress is higher than 590 N/mm^2 (86 ksi), was conducted (Iyama et al., 2019), that validates the assessment methods in the *Guidebook* with a slight modification for higher-strength steels. Studies on the 780 N/mm^2 class steel are currently under way. In addition, the use of ESW on high-strength structural steel with a thermo-mechanically controlled process (TMCP) was studied (Fujisawa et al., 2019); softening of the HAZ in the ESW joint of TMCP steel is inevitable, and this study demonstrated that the ESW joints that had enough penetration—that is, t_w was large enough, as shown in Figure 16(a)—did not show brittle fracture if the HAZ was softened.

ACKNOWLEDGMENTS

This paper was prepared as the work of the International Publicity Committee on Welding Technology for Building Structures in the Japanese Society of Steel Construction under the financial support of the Japan Iron and Steel Federation. The authors are grateful to the two organizations and other members of the committee. Professor Chia-Ming Uang at the University of California, San Diego, and Professor Atsushi Sato at Nagoya Institute of Technology gave many valuable comments to the draft of this paper; the authors would like to express our deepest gratitude to them.

REFERENCES

Agic, T. and Hampton, J.A. (1968), "Electroslag Welding with Consumable Guide on the Bank of America World Headquarters Building," *Welding Journal*, December, pp. 939–946.

AIJ (1971), *Welding Work Standards V Consumable Electroslag Welding*, Architectural Institute of Japan. (in Japanese)

Akiyama, H., Yamada, S., Matsumoto, Y., Takeuchi, T., and Sugimoto H. (2002), "Full Scale Shaking Table Test on Ultimate Seismic Resistance of Advanced Type of Beam-to-Column Connections," *Journal of Structural and Construction Engineering (Transactions of AIJ)*, Vol. 67, No. 551, pp. 141–148. (in Japanese)

Chambers, J.J. and Manning, B.R. (2016), "Electroslag Welding: From Shop to Field," *STRUCTURE magazine*, February, pp. 20–23.

Fujisawa, S., Umeda, T., Shimokawa, H., Ishii, T., Harada, Y., Morita, K., Kobayashi, M., and Song, Y.H. (2019), "Highly Efficient Welding Process for Built-up Box-Section Column Tensile Tests of Electro-Slag Welded Joints of Thermo Mechanical Control Process (TMCP) Structural Steel," presented at 12th Pacific Structural Steel Conference, Tokyo.

Ishiguro, T., et al. (1975), *Welding in Steel Building Structures*, Rikoh Tosho. (in Japanese)

ISO (2016), Metallic Materials—Charpy Pendulum Impact Test—Part 1: Test Method, ISO 148-1:2016, International Standards Organization, Geneva, Switzerland.

Iyama, J., Matsumoto, Y., Ishii, T., Shimokawa, H., Nikaido, M., and Yamada, S. (2019), "Fracture Strength of Electroslag Welding Joint with High-Performance Steel," *Journal of Constructional Steel Research*, Vol. 153, pp. 495–508.

Japan Steel Structure Journal (1998), *Development of Steel Structure Technology in Japanese Architecture—A Brief History of 50 Years after World War II*, Chapter 18, Production Processing Technology. (in Japanese)

Japan Welding Engineering Society (2004), Q09-02-01: "Built-up Box Sections Are Often Used for Steel Columns of Building Structures. How are interior diaphragms welded in through-column type beam-to-column joints?" Japan Welding Engineering Society, http://www-it.jwes.or.jp/qa/details.jsp?pg_no=0090020010 (accessed July 28, 2022). (in Japanese)

JSSC (2009), *Introduction to Design of Steel Structures,* 4th Ed., Japanese Society of Steel Construction. (in Japanese)

JSSC (2016a), *Guidebook for Prevention of the Occurrence of Brittle Fractures of Inner Diaphragm Plate Electroslag Welds*, Japanese Society of Steel Construction. (in Japanese)

JSSC (2016b), *Manual for Standard Mechanical Tests of Weld Zone in Steel Building Structures*, Japanese Society of Steel Construction. (in Japanese)

Kayamori, Y., Suzuki, T., Shimokawa, H., Tabuchi, M., Nakagome, T., and Morita, K. (2007), "Study on Fracture Properties of Electroslag Welds: Part 12, Correlation between Charpy Absorption Energy and Maximum Principal Stress," *Summaries of Technical Papers of Annual Meeting Architectural Institute of Japan. C-1, Structures III*, pp. 789–790. (in Japanese)

Lee, P., Garai, R, Ozkula, G., Uang, C.M., and Sarkisian, M. (2014), "Issues on Using Welded Built-up Box Columns in Steel Special Moment Frames," presented at the Tenth U.S. National Conference on Earthquake Engineering, Anchorage, Alaska, July 21–25.

Matsumoto, M. (2000), "Steel Structures," *Journal of the Japan Welding Society*, Vol. 69, No. 8, pp. 628–632. (in Japanese)

Nippon Steel Welding & Engineering (2019), *Simplified Electroslag Welding Process with Non-Consumable Elevating Tip (SESNET method)*, Nippon Steel Welding & Engineering Co. Ltd., https://www.weld.nipponsteel.com/techinfo/weldqa/detail.php?id=27U3U9W (accessed July 28, 2022). (in Japanese)

Sakurai, R. and Takahara, S. (1966), "Electroslag Welding Applied to Steel Building Structures," *Manufacturing & Technology*, Vol. 18, No. 4, pp. 3–16. (in Japanese)

Shimanuki, H., Suzuki, T., and Azuma, K. (2003), "An Investigation on Brittle Fracture of Electro-Slag Welded Joint between Interior Diaphragm and Box Column, Part 1. Material Properties of Welded Joint," *Summaries of Technical Papers of Annual Meeting Architectural Institute of Japan. C-1, Structures III*, pp. 877–878. (in Japanese)

Shimokawa, H., Song, Y.H., Ishii, T., Suzuki, T., Harada, Y., and Morita, K. (2019), "Study on Fracture Behavior of Electroslag Welding Joint," presented at the 12th Pacific Structural Steel Conference, Tokyo, Japan.

Song, Y.H., Shimokawa, H., Ishii, T., Suzuki, T., Kayamori, Y., Harada, Y., and Morita, K. (2009), "Study on Fracture Behavior of Electroslag Welded Joints Using Cruciform Model Joints," *Kou kouzou rombunshuu*, Vol. 16, No. 64, pp. 49–63. (in Japanese)

Ueno, M. and Ariyasu, H. eds. (1968), *Consumable Nozzle Electroslag Welding*, Morikita Publishing. (in Japanese)

Umeda, T., Ishii, T., Fujisawa, S., and Shimokawa, H. (2022), "Effect of Penetration Depth of Electro-Slag Welding on Ductility of Beam-to-Column Connection," *Journal of Constructional Steel Research*, Vol. 189, Article No. 107081.

Wada, T., Namba, M., and Tanaka, T. (1990), "Welding Consumables for Building and Civil Engineering," *Journal of the Japan Welding Society*, Vol. 59, No. 7, pp. 514–521. (in Japanese)

Yamaguchi, M. (1997), "Welding Consumables and Procedures for Electroslag Welding," *Journal of the Japan Welding Society*, Vol. 66, No. 4, pp. 279–283. (in Japanese)

Steel Structures Research Update

Slotted-Hidden-Gap Connections and Intentional Eccentricity for Steel Brace Members

JUDY LIU

INTRODUCTION

Research on alternatives for steel brace members and their connections is highlighted. These studies are a collaboration between Dr. Colin Rogers, Professor and Acting Chair at McGill University, and Dr. Robert Tremblay, Professor at Polytechnique Montreal. Dr. Rogers's research interests include structural steel connections, seismic design of low-rise steel buildings, lateral-force-resisting systems for cold-formed steel structures, and seismic-deficient braced steel frames. Dr. Tremblay's research interests include seismic design, dynamic analysis and stability of structures, steel, and steel-concrete structures. Dr. Tremblay was recognized in 2022 with AISC's Lifetime Achievement Award for significant contributions to the development of steel design standards and the advancement of seismic design of steel structures, including braced frames. Service contributions for Dr. Rogers and Dr. Tremblay include their work on the Canadian Standards Association (CSA) S16 Design of Steel Structures committee. Some of the research team's investigations into novel approaches for steel brace and connection design are presented, along with a preview of future work.

BRACES WITH INTENTIONAL ECCENTRICITY

Research on braces with intentional eccentricity (BIEs) is motivated by improvements in seismic performance compared to concentrically loaded brace (CLB) members. A brief summary of the background, motivation, and research objectives is presented. Also provided are selected highlights of the experimental program and supplementary finite element study.

Disadvantages for concentrically braced frames (CBFs) stem from stiffness and overstrength. The frames see high spectral acceleration demands and therefore large design forces due to their initial lateral stiffness. The concentrically loaded brace (CLB) members are sized based on their compression resistance. The resulting overstrength creates challenges in capacity design, as other CBF members and components are designed to resist the expected, or probable, strength of the CLBs. Additional overstrength is due to seismic width-to-thickness limits, established to improve frame ductility and energy dissipation by delaying local buckling and eventual fracture at mid-length plastic hinge region. Meanwhile, CBFs experience low lateral stiffness as the braces yield in tension and buckle in compression. This behavior can concentrate in one story or a limited number of stories, leading to large lateral drifts and the potential for a soft-story mechanism.

The introduction of eccentricity in the brace can improve the seismic behavior. Skalomenos et al. (2017) are credited with the initial concept of offsetting the brace longitudinal axis from the line of force, as shown in Figure 1. The eccentricity produces bending in addition to axial force and results in a lower initial stiffness. Rather than yielding uniformly over the cross section, yielding begins at the extreme fiber. The subsequent progression of yielding through the cross section results in a greater post-yield stiffness. The flexural response also "induces a more even distribution of the strain demands over the brace length, instead of an earlier strain concentration at mid-length as in CLBs" (González Ureña et al., 2022). So, the onset of local buckling is delayed, increasing the fracture life of the brace. The eccentricity can be tuned to the desired initial and post-yield stiffness. The eccentricity can also be adjusted at specific stories to achieve a design with a "smoother distribution of drift demands over the building height" (González Ureña et al., 2022). For a detailed analysis of the force-deformation response of a BIE, refer to González Ureña et al. (2022).

The potential benefits of braces with intentional eccentricity are supported by system analyses conducted by the research team. González Ureña et al. (2021) investigated the seismic design and performance of frames with intentionally eccentric braces (FIEBs). The study included nonlinear time-history analyses of 4-, 8-, and 12-story prototype buildings designed with FIEBs for high-seismic demands. Maximum and residual story drifts were "significantly lower, owing to the substantial secondary stiffness of BIEs" (González Ureña et al., 2021). Also, the study demonstrated that BIEs can be used to avoid the concentrically braced frame tendency to concentrate drift demands within a story

---

Judy Liu, PhD, Research Editor of the AISC *Engineering Journal*, Professor, Oregon State University, School of Civil and Construction Engineering, Corvallis, Ore. Email: judy.liu@oregonstate.edu

ISSN 0013-8029

or limited number of stories. Refer to González Ureña et al. (2021) for additional conclusions and commentary on the FIEB design.

The most recent work by the research team fills an important gap in knowledge for BIEs. Skalomenos et al. (2017) tested five half-scale BIE specimens using circular HSS and two different eccentricity values. Though the potential of BIEs has been demonstrated, there have been "no published reports on physical performance of full-scale nor square HSS BIE specimens" (González Ureña et al., 2022). The team therefore tested full-scale square ASTM A1085/A1085M (ASTM, 2015) HSS BIE and CLB specimens under cyclic loading. One specific research objective was to evaluate the "response of BIEs complying with and exceeding the CSA S16-14 limits for global and local slenderness" (González Ureña et al., 2022). Supplementary finite element (FE) models of CLBs and BIE extended the work, providing a look ahead to design of frames with intentionally eccentric braces (FIEBs). Refer to González Ureña et al. (2022) for a detailed presentation and discussion of the FE models and results.

Highlights of the Experimental Program

Test specimen details were based on current specifications and a prototypical frame. The team referenced CSA S16-14 (CSA, 2019) global and local slenderness limits for rectangular HSS CLBs. Dimensions were based on a 19.7 ft × 13.1 ft frame. Specimen 1 was a 5-in.-square, 0.315-in.-thick (HSS 127×127×8) CLB, for comparison with the BIE specimens. Specimen 2 was a BIE the same HSS section as Specimen 1 but with an eccentricity of 5.12 in. Specimens 3 and 5 were 10-in.-square, 0.512-in.-thick (HSS 254×254×13) BIEs, tested to determine if eccentricity could improve brace behavior. For these two specimens, the global slenderness was below the CSA S16-14 lower limit of 70. González Ureña et al. (2022) noted that the lower limit is "intended to preclude overly stocky braces, as low global slenderness is correlated with a higher probability of undesirable premature fracture." The width-to-thickness ratios (local slenderness) satisfied CSA limits. Specimens 3 and 5 had eccentricities of 7.87 in. and 11.8 in, respectively. Specimen 4 was a thinner-wall version of Specimen 3. For this 10-in.-square, 0.394-in.-thick (HSS 254×254×10) BIE, the local slenderness was greater than allowed by CSA S16-14.

The test setup was designed to represent a prototypical FIEB. To create the eccentricity, an "eccentering" assembly of two side plates welded to corners of the HSS connected the brace to a knife plate, as shown in Figure 2. The knife plate was detailed to act like a pinned connection, allowing out-of-plane rotation with buckling of the brace. The knife plate was then slotted onto a gusset plate and connected with four bolted angles. The cyclic loading history applied increasing displacements based on equivalent interstory drift of the prototypical 19.7 ft × 13.1 ft frame. For example, 1% drift corresponded to a brace axial displacement of 1.31 in. Refer to González Ureña et al. (2022) for more details of the test specimens, instrumentation, test set-up, and loading.

The behavior of Specimen 1 was as expected for a CLB. There was a "clear transition between the elastic and post-yielding stages in tension, a nearly constant post-yielding maximum force, and a distinct peak force in compression before its strength deteriorated due to global buckling" (González Ureña et al., 2022). The post-yield stiffness in tension was only about 1% of initial stiffness. Local buckling near mid-length began during the first 3% drift cycle in compression. Fracture due to low-cycle fatigue occurred during the second 4% drift cycle.

Specimen 2, the BIE version of Specimen 1, exhibited markedly different behavior in tension and compression. Specimen 2 had "significant post-yielding stiffness in

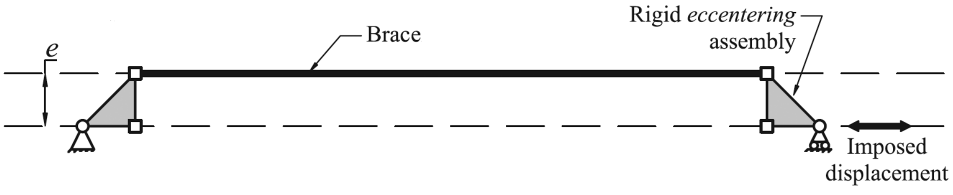

(a)

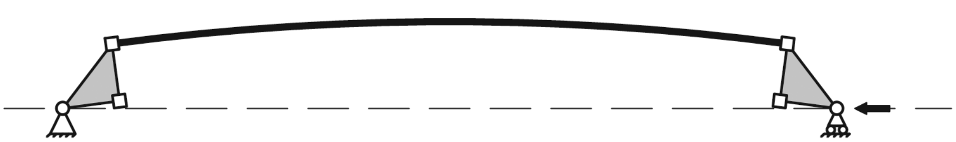

(b)

Fig. 1. (a) Components of a BIE and (b) deformed shape under compression.

tension, approximately 26% of the initial stiffness, and a smooth flexural response in compression, displaying neither global nor local buckling" (González Ureña et al., 2022). Specimen 2 achieved 58% of the theoretical tension yield capacity for the concentrically loaded Specimen 1. A decrease in the compression force after the peak was attributed to an increase in effective eccentricity due to bending. Specimen 2 started to fracture near the top eccentering assembly during first excursion to 2% drift in tension, with complete separation occurring during first 2.5% cycle. This failure mode would be studied further with the supplementary FE models.

Specimens 3, 4, and 5 all exhibited similar behavior, with local buckling and low-cycle fatigue fracture at brace mid-length. Specimen 5, with the same section but larger eccentricity than Specimen 3, had better fracture life (i.e., larger displacement) but lower initial stiffness and forces. Specimen 4 had the shortest fracture life of the three, due to its larger local slenderness. Initial stiffness and peak force values correlated to the cross-sectional areas for the three specimens, but post-yield stiffness was somewhat independent of the HSS properties.

The complementary FE models provided supplementary data as well as insight into the failure mode of Specimen 2. The fracture near the eccentering assembly revealed a shortcoming in the BIE configuration. A BIE under tension also experiences its largest flexural demands adjacent to the eccentering assemblies. From the FE model, Specimen 2, at time of failure, had reached its plastic bending moment capacity and about 71% of its maximum tensile strength. In another BIE FE model with the same failure mode, the BIE reached its plastic bending moment capacity and approximately 51% of its maximum tensile strength. In the BIE configuration used, the combined axial and flexural demands were being transmitted by welds along the corners of the HSS, where cold working and the heat of welding have affected the material ductility. González Ureña et al. (2022) considered that a configuration engaging the entire perimeter of the HSS would improve performance, but they also noted that Skalomenos et al. (2017) saw brittle failure with such a connection.

Given these results, the research team conducted an analysis of rotational demands at the ends of the HSS braces with the objective of developing design guidance. Noting limited data from this study and a lack of published work on rotational capacities of HSS under tension loading, they recommended that a conservative allowable rotation limit be used for HSS BIE design. The team suggested a provisional rotational limit of 10°. Refer to González Ureña et al. (2022) for more details of this analysis and recommendation.

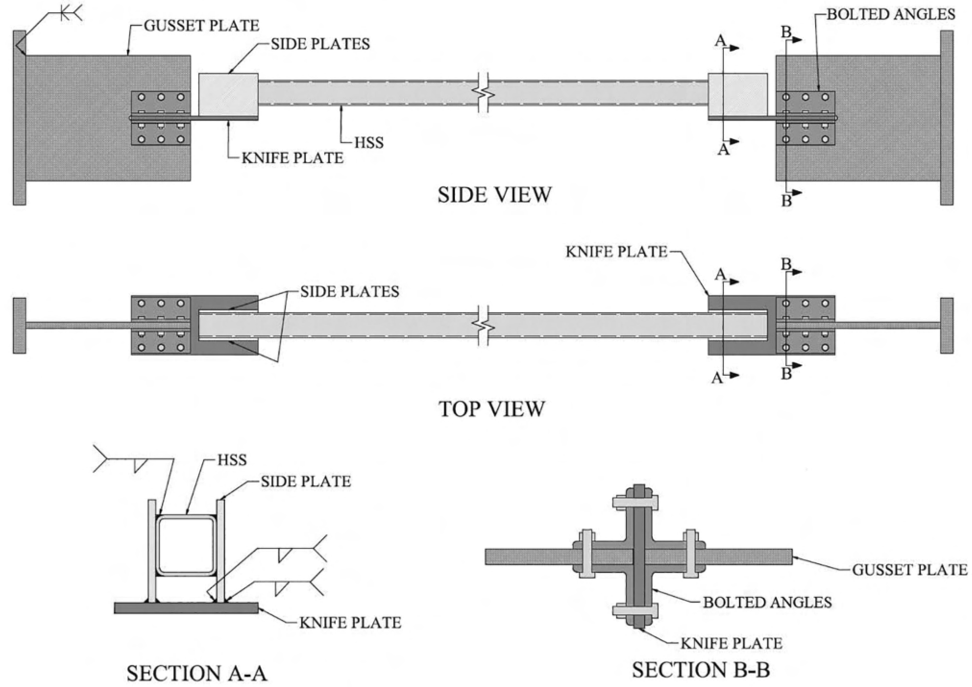

Fig. 2. BIE test setup.

Discussion

The highlighted work demonstrated the viability of BIEs and research needs. The BIE specimens “exhibited overall behavior and beneficial effects of the applied eccentricity, specifically substantial post-yielding stiffness and delayed onset of buckling at the brace mid-length” (González Ureña et al., 2022). The eccentricity can improve the fracture life of HSS braces that do not satisfy CSA S16-14 limits on global and local slenderness. Three BIE specimens had low-cycle fatigue-induced fracture at brace mid-length. One BIE fractured at the end, near the eccentering assembly, due to large rotation demands. More research is needed on allowable cyclic displacement capacities, especially at the ends of the BIEs. The research team recommends additional work focused on development of eccentering assemblies with lower rotational and strain demands on the HSS braces.

SLOTTED-HIDDEN-GAP CONNECTIONS

The slotted-hidden-gap (SHG) connection may eliminate the need to reinforce HSS braces at knife-plate connections, but existing design guidance is limited. The SHG prevents net section rupture of the HSS at the connection, promoting yielding throughout the brace length before rupture at midspan. Studies have confirmed the viability of the SHG connection, but the existing, empirical design approach was somewhat limited by available test data. Through an extensive, integrated program of numerical parametric studies and physical tests, the research team developed SHG connection design and detailing guidelines.

Characteristics of Slotted-Hidden-Gap Connections

The SHG connection differs from the conventional knife-plate connection in that both the HSS brace and gusset plate have slots. For the conventional connection, the gusset plate is inserted into slots on two sides of the HSS brace member and attached with fillet welds [Figure 3(a)]. This configuration locates the reduced net section of the HSS at the welds. The HSS also experiences shear lag and nonuniform tensile stresses at its reduced section. For the SHG connection, based on Mitsui et al. (1985), a slot is also cut into the gusset plate as shown in Figure 3(b). Mitsui et al. first introduced this “extended plate configuration” that, when assembled, allows the gusset plate and welds to extend past the ends of the HSS slots to the gross cross section (Figure 4). Stress concentrations are therefore moved away from the reduced net section. There is also a gap between the end of the HSS slot and the end of gusset plate slot.

A primary benefit to using SHG connections is that reinforcement of the net section is no longer needed. The HSS braces are the energy-dissipating fuses in the system, and capacity design principles require that the connection be stronger than the probable, or expected, strength of the brace. With an effective net section reduced by the slots and shear lag effects, section reinforcement (e.g., the addition of side plates) is typically necessary to satisfy capacity design requirements. The SHG connection, meanwhile, concentrates the inelastic demands away from the reduced section. In cyclic testing of braces or concentrically braced frames (CBFs) with SHG connections, Martinez-Saucedo et al. (2008), Packer et al. (2010), and Okazaki et al. (2013) did not observe any damage in the gusset plates, welds, or HSS net section. The main findings included confirmation that an increased weld length would reduce shear lag effects (Martinez-Saucedo et al., 2008) and that an SHG connection promotes extensive yielding in the brace with no fracture at the connection (e.g., Packer et al., 2010). These studies confirmed the viability of the SHG connection.

Research Objectives

The research team sought to improve seismic design and detailing methods for SHG connections. Existing guidance was “rather empirical and limited by the range of connection geometries and materials that had previously been tested” (Afifi et al., 2023). The work highlighted here builds from the research team’s studies (Moreau et al., 2014; Afifi et al., 2021) that already provided insight into some details and brace behavior. For example, Moreau et al. (2014) recommended a minimum overlap length of 5% of the weld length as sufficient to develop the tensile yield resistance of the HSS brace. The study also showed net section fracture of conventional connections compared to yielding on the gross area for the braces with SHG connections. The load-transfer mechanism and effects of different parameters were extensively studied (e.g., Afifi et al., 2021). The work demonstrated the importance of a weld overlap length in avoiding net section rupture, benefits of smaller weld sizes and longer weld lengths, and the ability of SHG braced frame building models to achieve large interstory drift ratios (Afifi et al., 2021).

The team continued to investigate critical parameters—for example, weld configurations—and their effects on the performance of SHG connections in seismic applications. This work was accomplished through numerical parametric studies coordinated with an experimental program. Design and detailing recommendations were major outcomes of the research.

Numerical Parametric Study

Critical parameters investigated included the HSS size and thickness, weld overlap length, weld size and length, and gusset plate width and thickness. The study was organized in four parts. In Part 1, four 6-in.- to 12-in.-square

HSS were studied. Thickness was initially constant across the HSS, and then different thicknesses were investigated. Part 2 focused on the gusset plate thickness, ranging from 0.748 in. to 1.25 in. Part 3 examined welds approximately 10 in. to 24 in. long and weld size varying from 1.25 in. to 0.748 in. Part 4 focused on the overlap length—that is, the length of the weld on the gross cross-sectional area of the HSS. The overlap length was varied for a constant total weld length.

In the finite element (FE) model, solid elements and typical detailing and common grades of steel were used. First-order reduced-integration, hexahedral, eight-noded solid elements with hourglass control were used for the HSS, welds, and gusset plate. The HSS slot width was typically 0.118 in. greater than the plate thickness. Slots had rounded ends as is common detailing practice. HSS tubes were grade CSA G40.20-21, 350 W Class C (CSA, 2018) with nominal $F_y = 51$ ksi and $F_u = 65$ ksi. Plates were ASTM A572/A572M Gr. 50 (ASTM, 2021) with nominal $F_y = 50$ ksi and

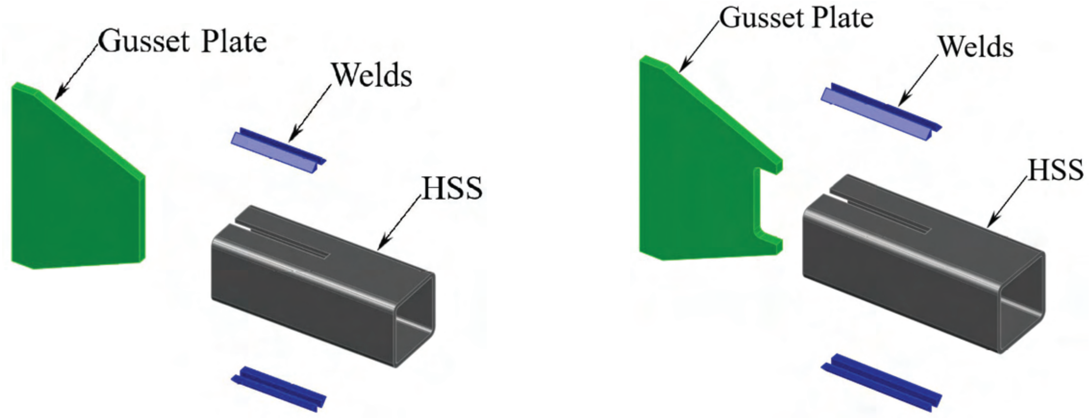

(a) Conventional *(b) Slotted-hidden-gap (SHG)*

Fig. 3. Exploded views of connection assemblies.

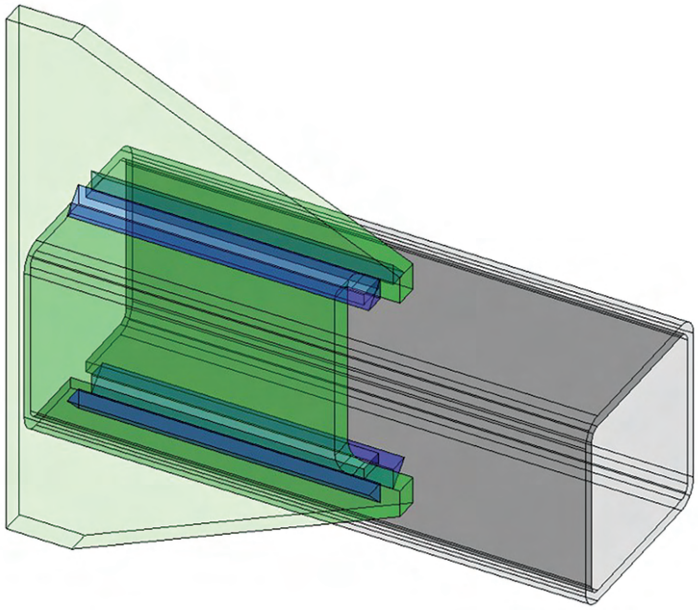

Fig. 4. X-ray view of slotted-hidden-gap (SHG) connection.

F_u = 65 ksi. For the welds, matching 71 ksi electrodes were used. For more FE model details, refer to Afifi et al. (2022).

The studies revealed how the different parameters affected the concentration of inelastic demands at the connections. The influence of HSS size and thickness is that larger sizes and thicknesses show more inelastic demands at the connection regions. As such, a larger weld overlap length may be needed to accommodate the increased connection stresses. Larger inelastic demands at the connection were also correlated to the thicker gusset plates. Meanwhile, smaller weld sizes and longer weld lengths resulted in a slight reduction in stresses at the connection. Finally, with a 0.787 in. weld overlap length, the desired SHG connection behavior was achieved. The study also revealed that the optimal weld overlap length is independent of the overall weld length. For more results and discussion, refer to Afifi et al. (2022).

Experimental Program

The experimental program and a companion FE study built upon the work by Moreau et al. (2014) and Afifi et al. (2021). Moreau et al. (2014) tested 4 conventional and 15 SHG connection specimens. Synthesis of the data and companion analyses by Afifi et al. (2021) revealed the influence of key parameters on the behavior of HSS braces with SHG connections as compared to conventional connections. The differences in the normalized load-deformation response and energy dissipation are clearly shown in Figure 5. The work also informed parameters requiring further investigation. The program described here expanded the range of applicability with brace and steel selection.

Test Specimens and Setup

This most recent work expanded the ranges for brace size and grade of steel. Specifically, 10-in.-square, 0.512-in.-thick (HSS 254×254×13) ASTM A1085/A1085M braces were used in this study. The HSS, the largest yet to be tested with the SHG connection, were chosen as they are typical of low- to medium-rise buildings in Canada (Afifi et al., 2022). With its relatively recent introduction to the market, A1085 steel is not commonly seen in published brace tests. Key parameters were tested with this extended range for HSS brace size and grade of steel.

The test program was designed to evaluate weld overlap length with consideration for the larger HSS and newer grade of steel. Specimens had SHG connections to paddle plates at both ends of HSS long enough to "allow for a uniform strain distribution at the central portion of the HSS brace" (Afifi et al., 2022) (Figure 6). Gusset plates were clamped by the grips of the loading device and were designed to remain elastic. Four bolted angles formed the gusset-paddle plate connection. For more details of the test set-up, refer to Afifi et al. (2022).

The two-part program investigated different weld configurations. The two specimens in Part 1 (weld configuration A) differed by the HSS slot length (15.2 in. vs. 15.9 in.) and the resulting weld overlap length (0.787 in. vs. 0 in.). Weld size and length were held constant at 1.14 in. and 15.4 in., respectively. In Part 2, longer, smaller welds (weld configuration B) were investigated. The weld size decreased from 1.14 in. to 0.748 in. Weld length increased from 15.4 in. to 24.4 in. The other parameters, such as weld overlap lengths, remained the same as in Part 1.

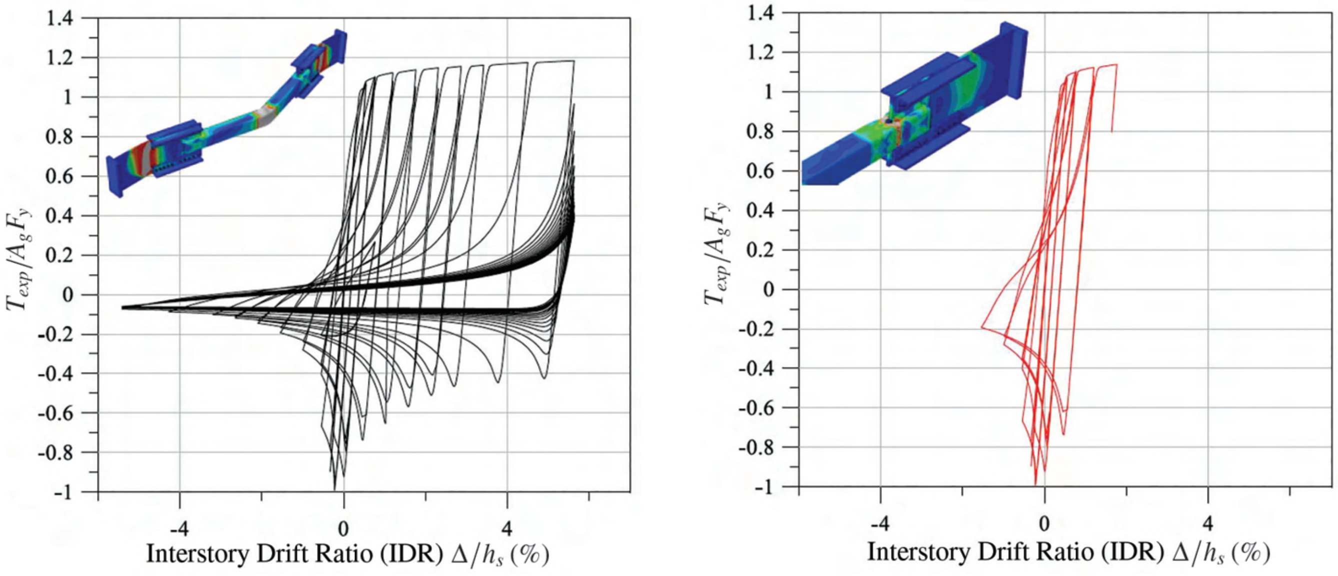

(a) *SHG connection*

(b) *Conventional connection*

Fig. 5. FE model comparisons of SHG and conventional connection normalized load-drift responses.

The specimens were loaded in tension and instrumented to capture the local strains as well as global force versus displacement. The specimens were monotonically and quasi-statically loaded so as to avoid strain rate effects. Instrumentation included the displacement transducer internal to the loading machine, string potentiometers for global and local displacements, strain gages, and a digital image correlation (DIC) system to capture local deformations. Additional details of the loading and instrumentation can be found in Afifi et al. (2022).

Results

The results from monotonic testing and companion FE models extended the range of applicability, supported prior conclusions, and provided additional insights into the behavior of HSS braces with SHG connections. As intended for these tests, inelastic behavior was limited to the braces. The paddle and gusset plates remained elastic. There was no damage to the welds or connecting angles.

For weld configuration A, results were markedly different between Specimen 1 (0.787 in. weld overlap length) and Specimen 2 (no weld overlap). Specimen 2 experienced extensive yielding at the connection before net section rupture at approximately 1.6 in. of displacement. The rupture was at the bottom connection. Welds at the bottom connection were shorter than specified and shorter than at the top connection. Specimen 1 experienced plastic elongation over the length of the HSS before a mid-length brace fracture at approximately 8.9 in. of displacement. Figure 7 shows this contrast in behavior for specimens from the Afifi et al. (2022) and Moreau et al. (2014) test programs. Note that the specimen shown in Figure 7(b) has a conventional connection.

Differences in behavior extended to the measured strains. In Specimen 1, the strains were initially higher at the top and bottom connections, reached peak strains, and then dropped off. Meanwhile, the strains at mid-length steadily increased for the duration of the test. In Specimen 2, strains were initially higher at the top connection, but the strains increased exponentially and were the highest at the bottom connection at the point of failure (i.e., fracture). Strains at Specimen 2 mid-length were less than half of the strain

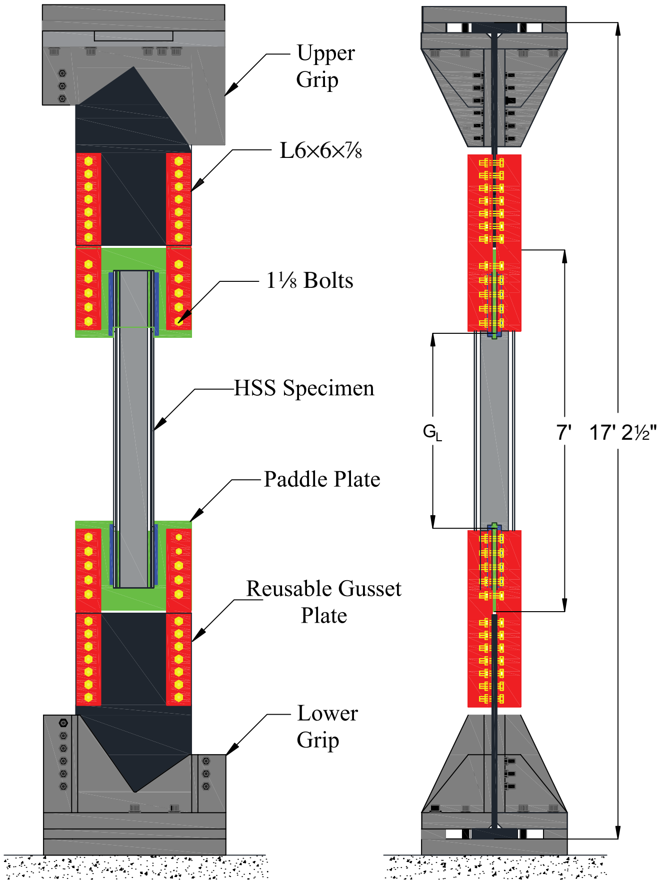

Fig. 6. Schematic of monotonic test setup.

at the top connection. Overall, Specimen 1 experienced a maximum strain of 55,000 με compared to only 35,000 με for Specimen 2.

The contrast in behavior was similar for Specimen 3 (0.787 in. weld overlap length) and Specimen 4 (no weld overlap), both of which used the smaller and longer welds for configuration B. Specimen 4 fractured on net section at approximately 1.6 in. of displacement. Specimen 3 yielded and fractured near mid-length of the brace, near 6.2 in. of displacement. Strain histories were also similar to those seen for weld configuration A. However, strains exceeded 80,000 με for Specimen 4 before fracture.

The test results confirmed expected effects of weld size and length. Specimens had different gage lengths for weld configurations A and B, so normalized load-displacement curves were compared. Specimen 1 failed at 19.2% brace strain compared to 22.3% for Specimen 3 with the smaller, longer welds. Specimen 3 also 1.5% higher tensile strength than Specimen 1; this was attributed to shear lag effects. A similar pattern was observed for Specimens 2 and 4, again with an increase in brace strains (2%) for the longer compared to the shorter weld.

The weld overlap length was the most critical parameter. Specimens with 0.787 in. weld overlap attained full capacity (yield) of the HSS member before fracturing at mid-length, away from the connection. No weld overlap resulted in localized yielding, necking, and fracture at the net section. As noted previously, for the same weld overlap length, the specimens with the longer welds experienced higher tensile loads and larger brace strains.

(a) SHG specimen

(b) Conventional specimen

Fig. 7. Extensive yielding along length of HSS and eventual fracture in SHG specimen from the Afifi et al. (2022) study, in contrast with fracture of conventional specimen at the connection from a Moreau et al. (2014) test.

The test results were supplemented with additional finite element (FE) investigations. Afifi et al. (2022) first conducted post-testing calibration of the FE models against the test results. Then, 25 FE models provided additional insight into the behavior of different SHG configurations for square HSS braces. The analysis results showed that thinner gusset plates are preferred. With the narrower slots in the HSS, loads are transferred more uniformly from the gusset plate to the HSS. The analyses also confirmed that smaller size, longer welds have lower inelastic demands at the connection and more extensive yielding over the brace length. Additional conclusions and recommendations can be found in Afifi et al. (2022).

Design and Detailing of SHG Connections

The research team sought to improve upon existing design and detailing recommendations for SHG connections. SHG connections prevent HSS net section rupture at the connections during the "high force tension cycles (anticipated strengths) of a seismic event" while eliminating the need to reinforce the net section to satisfy capacity design requirements (Afifi et al., 2023). The design recommendation development required additional parametric studies, as the investigations thus far "did not assess the effects of varying different elements simultaneously" (Afifi et al., 2023). In this parametric study, critical locations along the brace and connection were assessed, further evaluating important parameters for load transfer from the HSS to the plate.

The extensive parametric study was designed based on limits and most influential parameters from the research team's prior work. The studies to date had a limited number of square sizes, so the team explored 15 different HSS sizes. The HSS ranged from 16 in. square and 0.866 in. thick to 3 in. square and 0.189 in. thick (HSS 406×406×22 to HSS 76×76×4.8). Each HSS was analyzed with 2 weld configurations, 10 weld overlap lengths, 5 plate thicknesses, and 5 weld sizes. The gap length was kept at the 1.18 in. recommended by Martinez-Saucedo (2007). Afifi et al. (2023) noted that the gap met "fabrication tolerances found in common practice" and that keeping the value constant would minimize computations. The material properties (e.g., ASTM A1085 for the HSS) were also kept constant and consistent with Afifi et al. (2022). Capacity design requirements dictated the ranges for certain parameters. Weld size and length were chosen to be adequate for base-metal limit states and weld-metal fracture. Gusset plate thicknesses were also chosen such that yielding would not occur in the plate. Afifi et al. (2023) also noted that the "range for each parameter was chosen to provide a representative sample size while optimizing the needed computational time and cost." Further details of the parametric study can be found in Afifi et al. (2023).

The finite element modeling was as described in Afifi et al. (2021, 2022). Some highlights of the modeling included the stress-strain properties and gage length. True stress-strain curves were based on coupon data from the studies reported in Afifi et al. (2022). Stress-strain properties, accounting for the corners of the HSS and the longitudinal residual stress distribution, were based on Koval (2018). For comparison purposes, brace gage lengths were kept constant—that is, the distance between the HSS slot and brace mid-length was constant across the FE models.

The FE models were validated against prior work. FE model predictions were compared to experiments by Moreau et al. (2014) and Afifi et al. (2022) and prior numerical studies (e.g., Afifi et al., 2021, 2022). The FE model "accurately predicted" the overall connection response as well as location of fracture (e.g., at connection or brace mid-length) for braces with SHG connections with different overlap lengths.

Primary observations from the study related to load transfer and load overlap length. Free body cuts were used to examine load or force transfer through the brace and connection. Each critical location was assigned a "load participation factor," a percentage of load attributed to that connection element. One observation was that the weld load participation factor "increased uniformly with an extension of the weld overlap length" within a range of parameters (Afifi et al., 2023). Meanwhile, increases in weld overlap length showed some improvement in ductility, delaying displacement at failure when the fracture was at the connection. However, beyond the weld overlap length attributed to brace yielding and fracture in gross cross section, there was no benefit or increase in ductility with increase in weld overlap length. For additional results, refer to Afifi et al. (2023).

The main findings formed the basis for the proposed design methodology for the SHG brace connections. The expected, or probable, brace resistance is determined. The minimum weld length for the connection is chosen so as to avoid block shear rupture of the HSS at the connection. Then other components such as gusset plate thickness and weld size are selected based on the chosen weld length. The weld overlap length is chosen so that fracture will occur in at brace mid-length instead of at the connection. The research team's equation for minimum weld overlap length is based on the ratio of HSS effective net area to gross area and the slot thickness. Meanwhile, detailing requirements include a standard 1.18 in. gap as recommended by Martinez-Saucedo (2007), correlating to typical fabrication tolerances. The gusset plate slot width is the HSS outer dimension plus 0.118 in., also based on typical fabrication tolerances. Details of these and other requirements can be found in Afifi et al. (2023).

Validation included design and detailing of three braces and their SHG connections following the proposed design and detailing methods. Full FE models were created of the braces and their SHG connections. The models were subjected to a cyclic load history of increasing displacements, using a protocol similar to that for the long brace presented in Moreau et al. (2014) and Afifi et al. (2021). The three FE models exhibited the desired behavior, with buckling and fracturing at the mid-length plastic hinge. For details of the model and validation, refer to Afifi et al. (2023).

Discussion

Several numerical and experimental studies demonstrated the viability of the SHG connection, provided insight into important parameters, and supported the development of design and detailing guidelines. HSS width and thickness, plate thickness, weld size and length, weld overlap length, and gap length are primary factors in the performance of SHG connections. The proposed design method includes determination of the target weld overlap length, at which fracture occurs at brace mid-length rather than the net section at the connection. Numerical simulations of braces designed and detailed using the proposed method are able to sustain cyclic load reversals until buckling and fracturing at a mid-length plastic hinge.

FUTURE RESEARCH

The research team has advanced design of braced frame structures through research and design development for braces with intentional eccentricity (BIEs) and slotted-hidden-gap (SHG) connections. Full-scale experimental evaluation, supplementary finite element studies, and nonlinear dynamic system analyses have demonstrated the benefits of BIEs and highlighted areas requiring additional investigation. Design procedures, details, and performance of eccentering assemblies and connections are among the areas for future study. Afifi et al. (2022) investigated constructability of the SHG braces and connections, but this topic needs additional study as well. Another potential research topic is the influence of compression loading and gusset detailing of SHG connections for HSS braces.

ACKNOWLEDGMENTS

Thank you to Dr. Colin Rogers and Dr. Robert Tremblay for their contributions to this article. The work of Ph.D. graduates Mohamed Afifi and Andrés González Ureña, as well as Master's graduate Rolando Moreau, is also recognized, along with the technicians and engineers at the Hydro-Quebec Structural Engineering Laboratory at Polytechnique Montreal, as well as undergraduate and graduate research assistants from Polytechnique Montreal and McGill University. The research is sponsored by the Natural Sciences and Engineering Research Council of Canada (NSERC) and the Fonds de recherche du Québec-Nature et technologies (FRQ-NT). The researchers would also like to thank DPHV Structural Consultants, Constructions Proco, ADF Group Inc., and Atlas Tube for their technical and financial support. Any findings or recommendations are those of the researchers and do not necessarily reflect the views of the sponsors.

REFERENCES

Afifi, M., Moreau, R., Tremblay, R., and Rogers, C.A. (2021), "Evaluation of the Slotted-Hidden-Gap (SHG) Connection for Square HSS Brace Members," *Journal of Constructional Steel Research*, Vol. 179, No. 21, 106548. https://doi.org/10 .1016/j.jcsr.2021.106548

Afifi, M., Tremblay, R., and Rogers, C.A. (2022), "Numerical and Experimental Investigation of Slotted-Hidden-Gap (SHG) Connection for Square HSS Brace Members," *Journal of Constructional Steel Research*, Vol. 192, No. 4, 107234. https://doi.org/10.1016/j.jcsr.2022.107234

Afifi, M., Tremblay, R., and Rogers, C.A. (2023), "Design and Detailing Recommendations of Slotted-Hidden-Gap (SHG) Connection for Square HSS Brace Members," *Journal of Structural Engineering*, ASCE, Vol. 149, No. 2, 04022249.

ASTM (2015), *Standard Specification for Cold-Formed Welded Carbon Steel Hollow Structural Sections (HSS),* ASTM A1085/1085M, ASTM International, West Conshohocken, Pa.

ASTM (2021), *Standard Specification for High-Strength Low-Alloy Columbium-Vanadium Structural Steel*, ASTM A572/A572M-21, ASTM International, West Conshohocken, Pa.

CSA (2018), *General Requirements for Rolled or Welded Structural Quality Steel/Structural Quality Steel*, G40.20-13/G40.21-13 (R2018), Canadian Standards Association, Toronto, Canada.

CSA (2019), *Design of Steel Structures*, S16-14 (R2019), Canadian Standards Association, Toronto, Canada.

González Ureña, A., Tremblay, R., and Rogers, C.A. (2021), "Earthquake-Resistant Design of Steel Frames with Intentionally Eccentric Braces," *Journal of Constructional Steel Research*, Vol. 178, 106483. https://doi.org/10.1016/j.jcsr.2020.106483

González Ureña, A., Tremblay, R., and Rogers, C.A. (2022), "Experimental and Numerical Study of Square HSS BIEs under Cyclic Loading," *Engineering Structures*, Vol. 252, 113669. https://doi.org/10.1016/j.engstruct.2021.113669

Koval, I. (2018), "Accounting for Cold Working and Residual Stress Effects on the Axial Strength of HSS Bracing Members," M.Sc. Thesis, Département des génies civil, géologique et des mines, École Polytechnique de Montréal, Montréal, Canada.

Martinez-Saucedo, G. (2007), "Slotted End Connections to Hollow Sections," Ph.D. dissertation, Department of Civil Engineering, University of Toronto, Toronto, Canada.

Martinez-Saucedo, G., Packer, J.A., and Christopoulos, C. (2008), "Gusset Plate Connections to Circular Hollow Section Braces under Inelastic Cyclic Loading," *Journal of Structural Engineering*, ASCE, Vol. 134, No. 7, pp. 1252–1258.

Mitsui, Y., Kurobane, Y., and Endoh, K. (1985), "Experimental Study on Ultimate Strength and Deformation Capacity of Welded Tube-to-Through Gusset Plate Joints," *Journal of Structural Engineering*, ASCE, Vol. 31, No. B, pp. 145–156.

Moreau, R., Tremblay, R., and Rogers, C.A. (2014), "Evaluation of the 'Modified-Hidden-Gap' Connection for Square HSS Brace Members," Research Report, Department of Civil Engineering, McGill University, Quebec, Canada.

Okazaki, T., Lignos, D.G., Hikino, T., and Kajiwara, K. (2013), "Dynamic Response of a Chevron Concentrically Braced Frame," *Journal of Structural Engineering*, ASCE, Vol. 139, No. 4, pp. 515–525.

Packer, J.A., Chiew, S.P., Tremblay, R., and Martinez-Saucedo, G. (2010), "Effect of Material Properties on Hollow Section Performance," *Proceedings of the Institution of Civil Engineering: Structures and Buildings*, Vol. 163, No. 6, pp. 375–390.

Skalomenos, K.A., Inamasu, H., Shimada, H., and Nakashima M. (2017), "Development of a Steel Brace with Intentional Eccentricity and Experimental Validation," *Journal of Structural Engineering*, ASCE, Vol. 143, No. 8, 04017072. https://doi.org/10.1061/(ASCE)ST.1943-541X.0001809

Guide for Authors

Scope *Engineering Journal* is dedicated to the improvement and advancement of steel construction. Its pages are open to all who wish to report on new developments or techniques in steel design, research, the design and/or construction of new projects, steel fabrication methods, or new products of significance to the uses of steel in construction. Only original papers should be submitted.

General Papers intended for publication should be submitted by email Margaret Matthew, editor, at **matthew@aisc.org**.

The articles published in the *Engineering Journal* undergo peer review before publication for (1) originality of contribution; (2) technical value to the steel construction community; (3) proper credit to others working in the same area; (4) prior publication of the material; and (5) justification of the conclusion based on the report.

All papers within the scope outlined above will be reviewed by engineers selected from among AISC, industry, design firms, and universities. The standard review process includes outside review by an average of three reviewers, who are experts in their respective technical area, and volunteers in the program. Papers not accepted will not be returned to the author. Published papers become the property of the American Institute of Steel Construction and are protected by appropriate copyrights. No proofs will be sent to authors.

Manuscripts Manuscripts must be provided in Microsoft Word format. Include a PDF with your submittal so we may verify fonts, equations and figures. View our complete author guidelines at **aisc.org/ej**.

Smarter. Stronger. Steel.

American Institute of Steel Construction
130 E Randolph St, Ste 2000, Chicago, IL 60601
312.670.2400 | aisc.org/ej